MOLECULAR DYNAMICS STUDIES OF LIQUID AND CHAIN SYSTEMS

by

Vernon Simmons

B. S. in Physics, North Carolina A & T State University, 1995

M. S. in Physics, University of Pittsburgh, 1999

Submitted to the Graduate Faculty of
the Department of Physics and Astronomy in partial fulfillment
of the requirements for the degree of

Doctor of Philosophy

University of Pittsburgh

2004

UNIVERSITY OF PITTSBURGH

DEPARTMENT OF PHYSICS AND ASTRONOMY

This dissertation was presented

by

Vernon Simmons

It was defended on

April 26, 2004

and approved by

Robert Coalson, Professor

Steven Dytman, Professor

Yadin Y. Goldschmidt, Professor

Rainer Johnsen, Professor

Jeremy Levy, Associate Professor

Julia Thompson, Professor

Dissertation Director: Robert Coalson, Professor

MOLECULAR DYNAMICS STUDIES OF LIQUID AND CHAIN SYSTEMS

Vernon Simmons, PhD

University of Pittsburgh, 2004

Molecular Dynamics simulations have been used for the past 20 - 30 years to study interfacial properties of liquids though the foundations for these studies were laid as far back as 1791 when the astronomer Joseph Dalambre used the time reversible algorithm, commonly called the Verlet algorithm, for the integration of Newton's equations. Some of the properties obtained from Molecular Dynamics (MD) simulation are density profiles, system configurations, as well as stress or pressure tensor profiles. Generally, the surface tension has been calculated by integrating the stress tensor profile over the width of the interfacial region. In an effort to circumvent the stress tensor calculation and the technical difficulties associated with extensions to include many-body interactions, I studied the feasibility of implementing an equality recently developed by C. Jarzynski to determine the equilibrium surface free energy and, subsequently, the surface tension of an immiscible Lennard-Jones fluid from an ensemble average of a set of non-equilibrium simulations. In addition to exploring suitable systems on which to test what I will call the Jarzynski method, I established procedures for this type of simulation study.

ACKNOWLEDGEMENTS

Since arriving at Pitt and National Institute of Standards and Technology (NIST), I have received guidance, advice, support, and encouragement from a number of people. At Pitt, I benefited greatly from interactions with fellow graduate students Arie Barratt, John R. Cressman, Jr., Sandeep Tyagi, Andrew Peterson and Daniel Nestor, to name a few. I can easily break my time at Pitt into three parts and I would like to thank a few for their help during those periods. I thank Julia Thompson and Steven Dytman for helping me start at Pitt, Martin Vincent and James Mueller for helping me stay, and Robert Coalson for helping me finish. My gratitude at NIST will start with the Chemical Science and Technology Lab in general and extend specifically to William Koch and Willie May for providing such generous financial support and more importantly keeping an open door policy at all times. While at NIST, I was very fortunate to have had two mentors, Joseph Hubbard and Raymond D. Mountain, who have both given freely their time and energy to assist me in my studies. Though their styles differ, their passion for physics and chemistry and their wealth of knowledge helped to create an environment I enjoyed from the start. Lastly, I would like to thank my wife, Kym, for her never ending support during this part of my journey.

TABLE OF CONTENTS

I.0 INTRODUCTION . . . 1
- I.1 Surface Properties . . . 1
- I.2 Interfacial Characteristics . . . 2

II.0 MOLECULAR DYNAMICS SIMULATIONS . . . 5

III.0 A LOOK AT SURFACE TENSION USING MD SIMULATION . . . 15
- III.1 Introduction . . . 15
- III.2 The Pressure or Stress Tensor . . . 16
- III.3 Model and Simulation Properties . . . 18
- III.4 Simulation Results . . . 22
- III.5 Discussion of Simulation Results . . . 33

IV.0 MD TEST OF THE JARZYNSKI RELATION APPLIED TO INTERFACIAL TENSION . . . 41
- IV.1 Introduction . . . 41
- IV.2 The Free Energy-Work Connection . . . 42
- IV.3 Model and Simulation Properties . . . 47
- IV.4 Simulation Results . . . 54
- IV.5 Discussion . . . 62

V.0 MOLECULAR DYNAMICS OF ALKANETHIOL CHAINS . . . 66
- V.1 Introduction . . . 66
- V.2 Model and Simulation Properties . . . 67
- V.3 Simulation Results . . . 74

V.4 Discussion 87
VI.0 AN MD SIMULATION OF POLYETHYLENE OXIDE 89
VI.1 Introduction 89
VI.2 Model and Simulation Properties 90
VI.3 Simulation Results 96
VI.4 Simulation Results 107
VII.0 CONCLUSION 109
APPENDIX A. SIMULATION CODE FOR CHAPTER III 113
APPENDIX B. SIMULATION CODE FOR CHAPTER IV 123
APPENDIX C. BIBLIOGRAPHY 134

LIST OF TABLES

3.1 Maximal Long-Range Tail Corrections to the Interfacial Tension as a function of T^* and α. ρ_A^* and ρ_B^* are the density components of species A and B respectively. 40

4.1 Irving Kirkwood calculations of the free energy (F_{IK1i}) and the isotropic or scalar pressure (P_i) for the initial state or when interfacial area is A_0. The statistical error of these calculations is also shown. 54

4.2 Irving Kirkwood evaluations of the free energy (F_{IK1f}) and the isotropic or scalar pressure (P_f) at final state or when area is $2A_0$. The statistical error of these calculations are included. Note that F_{IK1} is independent of switching rate as it should be. 57

4.3 Free energy difference using the Jarzynski method. The nearly identical values of $\langle W \rangle$ and ΔF_J indicate that the switching process is very close to reversible for all switching rates. 59

4.4 Comparison of IK1 and Jarzynski free energy differences. ΔF_{IK} is independent of switching rate and is included in this chart for comparison. 60

4.5 Irving Kirkwood calculations for 2000 particle system. These quantities were calculated after system was equilibrated having interfacial area A_0 and $2A_0$. The statistical error is also shown. 63

5.1 Stretch parameters. CH_3 and CH_2 sites are equivalent for the stretch interaction. 69

5.2 Bend parameters. 69

5.3 The coefficients, C_l, in the torsional potential. Note that there is no site dependence for these coefficients. 70
5.4 The surface interaction parameters. 71
5.5 Lennard-Jones parameters. 73
6.2 Lennard-Jones Parameter and Charge Partitioning. 91
6.1 Stretch, Bend, and Torsion Parameters 93
6.3 Parameters for the Surface Interactions 94

LIST OF FIGURES

2.1 Connection between simulation, theory, and experiment. 6

2.2 Simple Lennard-Jones potential. 9

3.1 L-J potential functions for like and unlike species with α=0. The repulsive potential associated with the unlike interaction is reduced by a factor of 20. . 20

3.2 Initial particle distribution. The interface is initially parallel to the z-axis. . . 21

3.3 Final system configuration after equilibration is reached and prior to data collection. 23

3.4 Pressure, and ΔP vs. temperature where ΔP is the difference between the pressures at $\alpha = 0$ and $\alpha = 0.5$ respectively. ΔP is multiplied by a factor of 10 here for visualization. 24

3.5 Surface tension vs. Temperature for $\alpha = 0$ and $\alpha = 0.5$. 25

3.6 Surface tension vs. Temperature for $\alpha = 0.5$ for a simple L-J fluid in contact with its vapor. Note that, in contrast to the case of an immiscible binary fluid, γ^* decreases markedly with increasing T^*. 26

3.7 Interfacial density profiles for $\alpha = 0$ at $T^* = 1.176$ and 2.518. Note that the less volatile region expands as the temperature increases at an expense of the interfacial region. 27

3.8 Interfacial density profiles for $\alpha = 0.5$ at $T^* = 1.164$ and 2.530. Note the similar expansion of the less volatile region; hence, the variable α does not noticeably affect the overall behavior of the less volatile region. 28

3.9 Mole fractions for α=0 at $T^* = 1.176$ and 8.920 respectively. 30

3.10 Total density derivative for $\alpha = 0$ at $T^* = 1.176$ and 8.920 respectively. . . . 30

3.11 The kinetic and potential contributions to $\mathbf{P}_N^{IK1}$, the normal component of the interfacial pressure tensor profile, in the IK1 approximation for $\alpha = 0.5$ at $T^* = 1.165$.. 31

3.12 The kinetic and potential contributions to $\mathbf{P}_N^{IK1}$, the normal component of the interfacial pressure tensor profile, in the IK1 approximation for $\alpha = 0.5$ at $T^* = 8.821$. 32

4.1 L-J potential functions for like and unlike species with α=0. The repulsive potential associated with the unlike interaction is reduced by a factor of 20. . 49

4.2 Initial configuration of the $N = 1024$ system. This distribution has a sharp interface parallel to the z-direction. 50

4.3 Equilibrium configuration of $N = 1024$ system. The interfacial area is A_0 in this case. 51

4.4 Final configuration of $N = 1024$ system. The interfacial area is $2A_0$ in this case. 52

4.5 Work probability distribution. Switching rate in this case is in 100 step increments. 55

4.6 Density profile for the system when initial interfacial area A_0 and $2A_0$ for $T_{ref} = 3.0$. The two profiles are similar, but not identical. This implies that the equilibrium state of the system depends on the interfacial area. 61

4.7 Density profile for the initial interfacial area A_0 and $2A_0$ for $T_{ref} = 3.0$. This profile is for a system of 2000 particles. The densities in this case are close to identical which implies the area dependence on the equilibrium nature of the system is small. 64

5.1 Single chain molecule containing 19 sites in an all *trans* configuration. The molecule makes an angle of $\psi = 30°$ with the z-axis which is normal to the tethering surface. The large filled circle indicates the thiol group which is referred to as site number 1. The small shaded circles represent sites 2 through 18. The small filled circle indicates the terminal methyl united atom. 68

5.2 Density profiles for α=(a)$\frac{1}{10}$, (b)$\frac{1}{2}$, (c)$\frac{7}{8}$, and (d) 1. The profile for $\alpha = \frac{3}{4}$ is basically the same as for $\alpha = \frac{1}{2}$ and is not displayed. 75

5.3 Tilt angle distribution for $\alpha = \frac{1}{10}$(solid line), $\frac{1}{2}$(dashed line), $\frac{7}{8}$(long dashed line), and 1 (long short dashed line). Again, the distribution for $\alpha = \frac{3}{4}$ is very similar to the $\alpha = \frac{1}{2}$ case and is not displayed. 76

5.4 The average number of *gauche* defects for each chain site. The filled circles are the weak coupling case ($\alpha = \frac{1}{10}$), the filled squares for $\frac{1}{2}$, open diamonds for $\frac{3}{4}$, open triangles for $\frac{7}{8}$. The filled triangles are for the strong coupling case, α=1. 78

5.5 A snapshot of the chains with $\alpha = \frac{1}{10}$. This view shows that most of the chains are in nearly an upright position with local spatial order as well as indicated by the rows of chains. Periodic Boundary conditions mean the island of chains and the cavity are on the order of the box size. 79

5.6 A snapshot of the chains when $\alpha = \frac{1}{2}$ which shows that the disordered chains are located mostly along the interface between the island and the cavity. Here the chain tilt is more evident than the case in Figure 5.5. 80

5.7 A snapshot view of the chains with $\alpha = \frac{7}{8}$ which shows that the chains have nearly filled the cavity. 81

5.8 A snapshot view of the chains with $\alpha = 1$ which shows the ordered regions are smaller than the simulation cell 82

5.9 A snapshot view of the chains with $\alpha = 1$, just before the surface coupling was changed. 83

5.10 A chain snapshot when $\alpha = \frac{1}{2}$ after 350 ps. Here, a well defined cavity has formed, but the spacial ordering of the chains is not well developed. 84

5.11 A snapshot view of the chains for T = 329 K after 220 ps. The chains have now formed well defined rows. 85

5.12 A snapshot view of the chains for T = 360 K after 220 ps. The size of the cavity has decreased, the edge of the cavity is less sharp, and the spatial extent of the ordered rows is reduced from Figure (5.11). 86

6.1 Single surface-tethered $S(EO)_6CH_3$ molecule consisting of 20 sites in an all trans configuration, with the $S-CH_3$ vector oriented normal to the surface. The large filled circle represents the thiol head group, the small filled circles represent the 12 atom methylene units, the 6 oxygen atoms appear as large empty circles, and the united atom terminal methyl group is represented by a small filled circle. 92

6.2 Density profiles for four degrees of surface coverage:(a) full coverage at $0.214nm^2$ projected surface area per molecule, (b)$\frac{3}{4}$ full coverage, (c)$\frac{2}{3}$ full coverage, and (d)$\frac{1}{2}$ full coverage. The chain-surface interaction is weak and since the strong surface interaction causes similar behavior, it is not displayed. 97

6.3 The weak surface-interaction $S-CH_3$ tilt angle distributions. They are presented as the cosine of the angle that this vector makes with the surface normal vector and are shown for full surface coverage(solid line), $\frac{3}{4}$ full coverage (dashed line), $\frac{2}{3}$ full coverage (long dashed line), and $\frac{1}{2}$ full coverage (long-short dashed line). Results for the strong surface interaction are very similar and are not displayed. 98

6.4 Distributions of *intramolecular* O-O separation distances for weak chain-surface interaction are shown for four degrees of surface coverage: (a)full coverage, (b)$\frac{3}{4}$ full coverage, (c)$\frac{2}{3}$ full coverage , and (d)$\frac{1}{2}$ full coverage. Similar results for the strong surface interaction are not displayed. 99

6.5 The distribution of intramolecular O-O separation distances in the absence of any electrostatic interactions is shown for the full surface coverage case . . . 101

6.6 The projected snapshot view of all 225 chains as viewed from a vertical position located above the terminal methyl groups; this picture was taken at full surface coverage. The small dark blue spheres represent the terminal methyl groups, large yellow spheres are oxygen, small grey spheres are methylenes, and the small red spheres are sulfur. Even though the chains are predominately in an upright position and the lateral pattern is roughly hexagonal, there exists a considerable departure from the notion of perfect crystalline ordering which is due to thermal fluctuations. 102

6.7 Snapshot view of the chains at $\frac{3}{4}$ full surface coverage. There is a superficial resemblance to the full coverage picture; however, a closer inspection reveals that a substantial fraction of the chains are tilted away from an upright position. This effect is clearly seen in the associated orientation distribution. . . . 103

6.8 Snapshot view of the chains at $\frac{2}{3}$ full surface coverage. There is a close resemblance to both the full coverage and the $\frac{3}{4}$ full coverage cases; however, the associated orientation distribution now has a distinctly bimodal character. . . 104

6.9 Snapshot view of the chains at $\frac{1}{2}$ full surface coverage with a weak chain-surface interaction. There is a qualitative difference between this picture and those associated with higher coverage, insofar as well-defined cavities or regions completely devoid of chains are now apparent. The associated orientation distribution still resembles that for the $\frac{2}{3}$ full coverage case. Cavities are not observed at $\frac{3}{5}$ full surface coverage, even after equilibration times of 200 ps, which suggests that they may begin to appear over a rather narrow range of surface densities. 105

6.10 Snapshot view of the chains at 0.54 full coverage with a strong chain-surface interaction; note the appearance of a small though well-defined cavity. As in the weak surface interaction case, for the strong surface interaction case, cavities are not observed at $\frac{3}{5}$ full coverage, although large cavities are apparent at $\frac{1}{2}$ full coverage. 106

I.0 INTRODUCTION

I.1 SURFACE PROPERTIES

A fundamental property of liquid surfaces is that they tend to contract to the smallest area possible.(1) This tendency is due to the simplest properties of the molecules in liquids. In the interior of a liquid, each molecule is surrounded, and thus attracted, by other molecules. On average, over periods of time long compared to the molecular vibrations, the attraction on any molecule is uniform in all directions. At the surface, the story is much different. Molecules at the surface are subject to strong inward attractions *perpendicular* to the surface. This inward attraction causes the surface to diminish because the surface molecules move inward much faster than those from the bulk move outward to take their place.

When two non-mixing liquids come in contact with each other, an interface forms since this is a minimum free energy configuration. The presence of interfaces plays a fundamental role in a variety of fields for they are present in areas ranging from biology to metallurgy, and occur daily in natural and industrial processes such as adhesion. In many of these fields, a more detailed understanding of interfaces at the molecular level is becoming increasingly important.(2) If these systems are in a state of complete thermodynamic equilibrium, the interfaces arrange spontaneously in such a way that they correspond to free energy minima. Once a minimum free energy state is reached, the bulk properties remain unchanged; therefore, the surface state of the system is completely determined by the minimum of surface free energy.

The energy required to create a unit amount of interfacial area is defined as the surface tension or interfacial tension. Systems in nature continually try to reach a minimum energy configuration so if interfaces are present, the progress to and/or the final configuration of the equilibruim state is controlled by the surface tensions or the balance of the surface tensions of different interfaces of the system.(3)

The methods of measuring surface tension are classified into two categories: static and dynamic. The static methods measure the surface tension of practically stationary surfaces which have formed over an appreciable amount of time.(1) Static methods have been used for some time and are very well documented so I will focus primarily on the dynamic methods. Some important practical situations that require a better understanding of dynamic surface tension are(4) 1) Contact angle, which is determined by the balance between surface tension at a three-phase boundary, is important in large scale separation processes.

2) Wetting, adhesion, and detergency depend on the control of interfacial tension.

3) Emulsions and foams are stabilized/destabilized via surface-active agents.

I.2 INTERFACIAL CHARACTERISTICS

An important characteristic of an interface is that it breaks the symmetry of the bulk phases so properties vary differently parallel and perpendicular to it. This provides leverage in the study of forces, especially long-range forces, between molecules. A more thorough understanding of interfaces and interfacial properties can only come from a more extensive and self-consistent theoretical framework which assists the interpretation of experimental observations.(2) Another important point to keep in mind when examining the properties of interfaces is that the classical thermodynamic arguments that apply to the bulk may be quite different in the interfacial region. The formation of an interface breaks the homogeneity of a system and thermodynamic properties defined for homogeneous systems may have surprising characteristics. For instance, the heat capacity and compressibility, which are two quantities determined from thermodynamic fluctuations, can be negative in the interface; this is quite different than in the bulk since by definition, this cannot occur in a system of uniform density.(5) Two developments that have assisted in the study of interfacial properties are rapid extension of experimental techniques and introduction of computers.(2; 6; 7; 8)

As previously stated, the two methods of measuring surface tension are static and dynamic. Molecular dynamics (MD) simulations fall into the second category and have an important role in the investigation of condensed systems. This technique has provided the methodology for detailed microscopic modeling on the atomic scale, and is a powerful and widely used tool in chemistry, physics, and materials science. One significant feature of simulation studies is the ability to examine features that are not readily accessible to experimental methods.

In our simulations of simple, immiscible binary fluids, we focus on the thermophysical properties of these systems, such as internal pressure and surface tension, as well as an order parameter profile which describes the transition from one bulk fluid phase to the other. In the simulations of surface tethered chain molecules of both hydrophobic and hydrophilic types, we investigate the effects of chain chemistry, surface density, and chain-surface interaction on the types of structure that we observe.

In chapter II, I will give a more detailed background of the origins of MD simulations. I will also discuss some of its uses as well as relay some of the limitations that will arise. In the four subsequent chapters, I will present examples of how MD can be used to study specific molecular systems.

Chapter III provides a simulation study of the interfacial region of Lennard-Jones immiscible fluids. I will also discuss the mathematical construction of a microscopic or molecular level stress tensor from inter-atomic potentials and its use in calculating surface tension. Also in chapter III, I will introduce a void transfer mechanism to describe the interesting surface tension versus temperature behavior. In chapter IV, I discuss why it is desirable to bypass the stress tensor altogether in calculating interfacial tension. In this chapter, I will also introduce an idea originally proposed by C. Jarzynski(9) that allows one to acquire equilibrium free energy difference from a series of simulations of non-equilibrium processes. Though the system modeled is a simple Lennard-Jones mixture, the method and procedure outlined, if successful, should be applicable to more general and extensive system.

Chapter V consists of the results of a molecular dynamics study of a partial monolayer of self assembled octodecanethiol molecules. MD simulations are employed to examine the correlations between various statistical measures of surface induced chain ordering. I will focus particularly on thesignificance of the strength of the alkane chain surface interaction,as well as the role of temperature, on the type and degree ofdisorder observed. In chapter VI, I present a molecular study of surface-tethered $S(CH_2CH_2O)_6CH_3$. Here I examine the interplay between helix formation and thermal disorder. In this case, surface coverage as well as chain-surface interaction strength indicate that a set of approximately $\frac{7}{2}$ helical structures oriented predominantly normal to the surface are formed at near full coverage. The studies in chapter V and VI are necessary steps in the investigation of how self assembled octodecanethiol and polyethylene oxide films will behave when a fluid layer is imposed. Chapter VII concludes the dissertation: in it is reaffirmed the power of MD simulation in investigating systems on a microscopic scale. I have included an appendix which contains the Fortran 77 code used in Chapters III and IV. These should provide starting points for those who may want to continue or refine parts of this work.

II.0 MOLECULAR DYNAMICS SIMULATIONS

Though the N-body problem originated in the dynamics of the solar system, the general problem turns out to be analytically intractable for three or more body interactions. Once the atomic nature of matter was established, quantum mechanics dominated the study of the microscopic world. The situation became even more complicated because even the constituent particles seemed to behave in a manner not fully expected. Theory, in the form of statistical mechanics, for systems in thermal equilibrium has been very successful in describing this behavior from a conceptual point of view. Statistical mechanics provides a formal description of a system in equilibrium based on the partition function. Though this has been known for over a century, there are few quantitative results unless severe approximations are introduced. Simulation helps fill the gaps on the equilibrium side and in a sense provides a means of applying statistical mechanics to model the dynamical evolution of the system. Computers have long been used in scientific research, both in theory and experiment. Instead of attempting to obtain a description of the behavior of a physical system in closed form, the computer is able to examine the behavior of the original system directly.

The question of how simulation relates to physical theory usually arises in any discussion of the importance of MD or how it can be used in understanding problems occurring in nature. Though simulation is based on theoretical foundations, it tries to avoid much of the idealization and approximation normally associated with theory and replaces it with an extensive calculation effort. Simulation also draws from experiment since the output of any simulation should be treated with the same statistical methods as those used in analyzing experimental results. With computer simulation, the computer essentially becomes a laboratory in which a numerical experiment is conducted. Figure 2.1 shows a possible con-

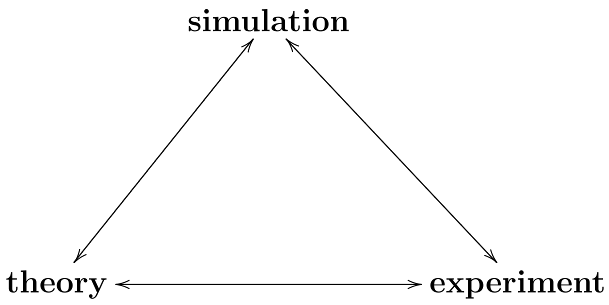

Figure 2.1: Connection between simulation, theory, and experiment.

nection between simulation, theory, and experiment. As emphasized by the arrows in this figure, these processes are in fact omnidirectional and are in no particular order of importance. Instead of simply fine tuning a Hamiltonian so that a few experimental observables are accurately produced, consider MD simulations as a means to extract information from a physical system that would be very difficult or impossible to obtain without it. While MD is dependent on the computer, it does not incorporate the two greatest developments in physics of the twentieth century - relativity and quantum mechanics. Special relativity proscribes information transfer at speeds greater than that of light; MD simulation typically assumes forces whose nature implies an infinite speed of propagation. Quantum mechanics has at its base the uncertainty principle; MD requires complete information about position and momentum at all times. In practice, the phenomena studied by MD simulation are those where relativistic effects are not observed and quantum effects can be incorporated or buried in the system potential if necessary. Strictly speaking, classical MD deals with a world that has little concern for anything that is "nonclassical". However, this fact has in no way diminished the power and effectiveness of the method. I should mention that though I will speak mostly about the classical use of MD, there are methods available that directly incorporate quantum mechanics into molecular dynamics simulations. These include, but are not limited to path integral methods(10; 11) which partially accounts for DeBroglie wave length effects and the Langevin-dynamics approach(12) which can be used to study dynamics systems composed of nanoparticles. The theoretical basis for MD embodies many of the important results produced by the great contributers of analytical mechanics, namely, Euler, Hamilton, Lagrange, and Newton. Some of their works contain fundamental observations about the apparent workings of nature while others lead to further theoretical developments. The simplest form of MD, that of simple particles, involves little more than Newton's second law. Rigid molecules require the use of Euler equations, and molecules with internal degrees of freedom may require the Lagrange method to incorporate geometric constraints into the dynamical equations. Though normal equilibrium MD corresponds to the microcanonical ensemble, constant $N, V, and\ E$, in certain cases properties at constant temperature (and sometimes pressure) are required. There are ways of modifying the equations of motion to produce such systems where the individual trajectories represent the solution of Newton's equations.(13)Molecular Dynamics Simulation are comprised of three main steps:

1) Select a set of potentials that behaves similarly to the system one wants to study. These may include explicit intramolecular forces similar to those used in chapters 5 and 6.

2) Derive the equations of motion and integrate these as a function of time.

3) Determine the relevant statistically averaged properties and interpret them.

Liquids represent the state of matter studied most by MD methods since both perfect crystalline solids and gases have well-developed theoretical foundations. For solids, theory begins by assuming that the atomic constituents undergo small oscillations about fixed lattice positions. For gases, independent atoms are assumed and interactions are introduced by weak perturbations. In the case of liquids, however, the interactions are as important as in the solid state, but there is no underlying ordered structure with which to begin. Though there has been dramatic progress, many challenges still remain when simulating liquids. Multiple phases introduce the issue of interfaces which often have a thickness comparable to the typical simulated region size. Inhomogeneities such as density or temperature gradients can be difficult to maintain in small systems, given the magnitude of fluctuations. There are also problems involving time scales which may be many orders of magnitude larger than those associated with the underlying molecular motion. This may introduce slow relaxation modes, diffusion hindered by structure, and the formation of spatial organization of some type.

Uses of MD can be broken down into the following categories: phase transitions, glassy materials, complex fluids, polymers, bio-molecules, and fluid dynamics. This is by no means a complete list of the types of systems MD could help understand, but it shows the flexibility of this type of simulation. Selecting a Hamiltonian should include determining whether the interactions are short- or long-ranged, and whether the system is thermally and mechanically isolated. If the system is isolated, normal dynamical laws are used or the equations of motion are modified to produce a particular statistical mechanical ensemble. One must also determine whether the constituent particles are structureless atoms or complex molecules. If the particles are complex, one must then determine if the molecules are rigid or flexible. The selected potential interactions could be between pairs of particles or have multi-particle contributions. There are other things to consider, but this should give an idea of the types of questions one must ask prior to simulating a system by MD.

The basic microscopic model for a substance capable of existing in any of the three most familiar states of matter - solid, liquid, and gas - is based on spherical particles that interact with one another. For liquid mixtures, the intermolecular potential as well as the interaction between the molecular properties of the components leads to a more complex topology of the thermodynamic phase space.(14) The simplest interactions between these atoms are between pairs and are responsible for providing the two principle features of an atomic force. The first is a resistance to compression so the interaction causes the atoms to repel one another at close range. The second is a binding term so the interaction must cause the atoms to attract each other over long range if separated by large distances. Potential functions having these characteristics adopt a variety of forms; the best known being the Lennard-Jones (L-J) potential (see Figure 2.2).(15) Two of the results we will present later use a simple L-J model; while the other systems contain distinct potentials needed to accommodate more system specific interactions. Though the L-J potential is quite simple, there are quite a few benefits to selecting it. First, it is smoothly varying and provides a continuous force model. Secondly, it is used extensively for the simulation of simple models and can be easily extended to investigate chain systems. The Lennard-Jones(12,6) fluid has been studied extensively both theoretically and using computer simulations. Though this model is generally known to be inadequate to represent an inert gas with high accuracy, it does provide a good model for testing liquid theories.(16) The L-J model selection also complies well with the principle

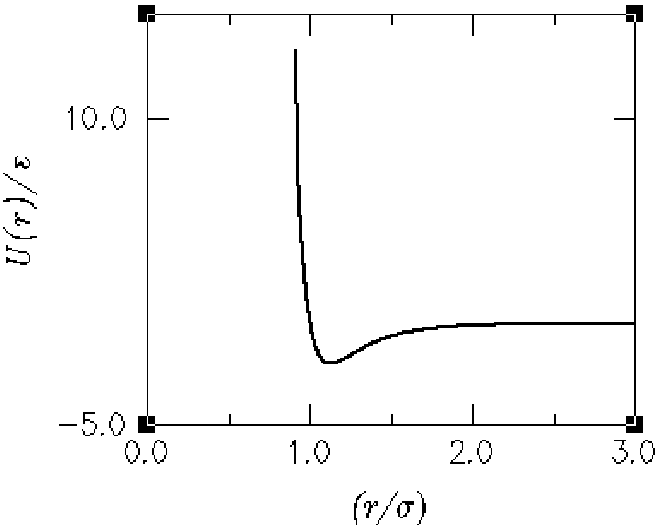

Figure 2.2: Simple Lennard-Jones potential.

of corresponding states which depends on the assumptions(17):

1) The translational motion of the molecules is classical.

2) The total potential energy is given by the sum of interaction energies of pairs of molecules.

3) The mutual pair potential energy of pairs of molecules has the form:

$$\epsilon(r) = \epsilon^{*}\phi\left(\frac{r}{r^{*}}\right) \tag{II.1}$$

where r is the distance between centers of molecules, ϵ^{*} and r^{*} are energy and length characteristics of the species involved, and ϕ is some universal or scale independent function (that *equals* -1 when $r = r^{*}$). From Eq. (II.1) one can see a L-J function provides a suitable potential choice.

Knowing the system's potential interactions allows determination of the corresponding forces, using the relationship $\mathbf{F} =$ -$\nabla U(r)$ and the equations of motion which follow from Newton's second law.

$$m\overrightarrow{a_i} = \overrightarrow{F_i} = \sum_{j=1}^{N_a} \overrightarrow{f_{ij}} \tag{II.2}$$

where the sum is over all N_a atoms excluding i itself, and m is the atomic mass. It is these equations that are numerically integrated in classical Molecular Dynamics programs. Using Newton's third law, namely $\overrightarrow{f_{ij}} = -\overrightarrow{f_{ji}}$ we see that each pair need be calculated only once. Since computer time may be expensive, one should consider where the majority of the computer time will be needed. For systems with pairwise interactions, the amount of simulation time is proportional to N_a^2 because one must compute $\frac{1}{2}N_a(N_a - 1)$ interactions. It is, therefore, a good idea to determine which atoms will contribute to the calculation of the observable quantities and not spend valuable time computing forces and potentials that provide little contribution. In the simulations discussed here, a nearest neighbor table has been used to reduce computation time.(18; 19) Though introducing a nearest-neighbor table will reduce the computation time, some consideration should also be given to the cut-off distance. It has been shown that this distance will affect the computed quantities, and this effect should be minimized.(6) The basic idea is to only consider those particles which are within a pre-determined distance from one another. The potential function, and hence the force, outside this region is zero. For a simulation, the simulated observables tend to be the same thermodynamic quantities observed in the laboratory, namely, total energy, temperature, pressure, and kinetic energy. The equations of motion can only be solved numerically. Because of the nature of the interatomicinteraction, atomic trajectories are unstable in the sense that an infinitesimal perturbation will grow at an exponential rate. With this in mind, there are sampling issues one has to contend with. Since integration of the equations of motion is a fundamental part of any MD simulation, the type of integrator chosen is also important. A comparatively low-order numerical integration method often suffices, and it's adequacy will emerge in the results and reproducibility of the simulation. A higher-order integrator should be used when softer interactions are involved such as those often used for modeling molecules with internal degrees of freedom. In addition to the higher-order integrator, a shorter time-step may help accommodate the fast internal motion. The numerical treatment of constraints introduces an additional concern; namely, that the constraints themselves must be preserved to much higher accuracy than is provided by the integration method. By numerically solving these equations of motion, one is able to gather important characteristics of the model or molecular system.The seminal work by Gibbs(20) made great strides in developing a statistical mechanical approach to study systems composed of molecules. A primary component of statistical mechanics is the ensemble, and obtaining observable quantities does depend on the ensemble ascribed to the system. Given the canonical ensemble where the temperature T, volume V, and particle number N are fixed, the equilibrium average of some quantity G is expressed in terms of phase-space integrals involving the potential energy $U(r_N)$:

$$\langle G\rangle = \frac{\int G(r_N)[\exp -\beta U(r_N)]dr_N}{\int[\exp -\beta U(r_N)]dr_N} \tag{II.3}$$

where r_N are the coordinates, $\beta = \frac{1}{k_B T}$, and k_B is the Boltzmann constant. This average corresponds to a series of measurements averaged over an ensemble of independent systems.The ergodic hypothesis relates the ensemble average to measurements carried out for a single equilibrium system over its time evolution. Both kinds of measurements should produce the same result. A Molecular Dynamics simulation produces averages of the form

$$\langle G\rangle = \frac{1}{M}\sum_{\mu=1}^{M} G_\mu(r_N) \tag{II.4}$$

over a series of M measurements made as the system evolves. Assuming the sampling is sufficiently thorough and captures the typical behavior, the two kinds of averaging will be identical. This notion of ergodicity and ergodic convergence for a Lennard-Jones type system has been studied thoroughly by Mountain and Thirumalai.(21) They found that for the homogeneous or one-component system, the structure of the energy and stress fluctuations suggested that essentially the system was in a minimum free-energy state. This is due to both the temperature range and time over which the following systems will be observed. When an interface forms, this amounts to each particle spending an equal amount of time in the interface as it does in the bulk.

Recall from basic statistical mechanics the concept of the equivalence of ensembles. An important consequence of this is that the basic thermodynamic properties of a model system may be calculated as averages in any convenient ensemble. Since MD simulation provides the instantaneous system configuration as well as the velocity distribution as output, some common expressions of thermodynamic quantities are:

$$KE = \sum_{i=1}^{N} \sum_{\alpha} \frac{p_{i\alpha}^2}{2m_i} \tag{II.5}$$

where KE is the kinetic energy, m_i is the molecular mass and α runs over the different spatial components of the momentum of atom i. The potential energy may be divided into terms depending on the coordinates of individual atoms, pairs, triplets, etc., but a calculation of any quantity involving the sum over triplets of molecules may be very time-consuming on a computer.

For liquids though, the pairwise approximation gives a good description because the three-body effects can be incorporated approximately by defining an effective pair potential term. The pair potentials appearing in MD are generally considered to be effective potentials and the potential energy can be written

$$U \approx \sum_{i} u_1(r_i) + \sum_{i} \sum_{j>i} u_2(r_{ij}) \tag{II.6}$$

where u_2 is the two-body potential and r_{ij} is the scalar distance between the centers of atoms i and j, $r_{ij} = |r_i - r_j|$. A consequence of an approximation of this type is the first term on the rhs of Eq. (II.6) sums over all particles while the second term is dependent only on the interaction between pairs of particles. The second term also neglects simultaneous multi-body interactions which, if included, would drastically increase the time required for the simulation.(6) In 1924, J.E. Lennard-Jones introduced a useful model for a soft-sphere pair potential which has since been studied extensively and found suitable to study liquid systems.(22) The total energy is simply the sum of Eqs.(II.5) and (II.6).

$$E =< H >=< KE > + < U > \tag{II.7}$$

Using the virial theorem, we can write the temperature and pressure relationships as:

$$2 < KE >=< \sum_{i=1}^{N} \frac{|p_i|^2}{m_i} >= 3Nk_BT \tag{II.8}$$

$$-\frac{1}{3V} < \sum_{i=1}^{N} r_i \cdot \nabla_{r_i} U > +\rho k_B T = P \tag{II.9}$$

Since the positions and velocities of the system are updated incrementally, the simulation also allows for calculation of the instantaneous temperature and pressure. Though the instantaneous quantities mentioned previously can be readily calculated from simulation, care must be used to distinguish these from true thermodynamic concepts such as pressure and temperature which can only be described as ensemble averages.

The nature of simulations in general and MD specifically contains inaccuracies which may be either systematic or influenced by the simulation process. These inaccuracies, or one could even call them errors, could be due to the finite system size or selected boundary conditions, potential cut-offs, and integration algorithm to name a few. There are more specific checks for code reliability so I will assume here that code induced errors are minimized. Usually periodic boundary conditions are chosen for MD simulation and this selection allows one to provide properties for a macroscopic sized system using a finite sized system. I should note here that the boundary conditions for the simulations in chapters V and VI are periodic in two of three dimensions. As will be shown in the immiscible binary fluid simulations of chapters III and IV, periodic boundary conditions causes the creation of two interfaces. The box length must be longer than the width and height to prevent interference between the liquid structural changes induced by the interfaces. A factor of two is stated often as suitable. To remove the finite size effects, we can extrapolate results to large system number and volume, holding the system density fixed. In order to decrease the amount of computation time needed, potential cut-offs are used. The errors due to these cut-offs are greatly reduced by choosing an optimum simulation time step size. I will include the system and simulation properties such as time-step size, particle number, potential, and box properties in each chapter for better continuity.

In the following chapters, I will try to differentiate "simulated results" from experimentally "measured quantities", but in most cases "measurements" are "theoretical calculations". Another point I should mention at this time concerns errors, and I will limit discussion to two types. First, there are errors associated with the computer system used by the simulation (systematic errors). Secondly, there are those associated with the molecular model used for the simulation (statistical errors).

To test for systematic errors, we should compare the simulation output evaluated using different platforms. For the systems selected, the accuracy is not affected by the type of computer used for the simulations.

The statistical errors associated with MD simulations in general are part of a larger concern, namely establishing the validity of the simulation. In the following chapters, I refer to the sample variances as the statistical errors. These are calculated using

$$\sigma_N^2 \equiv \frac{1}{N} \sum_{i=1}^{N} \left(x_i - \bar{x}\right)^2 \tag{II.10}$$

where x_i, $\bar{x}$ and N are the simulated measurements, the average of these measurements and the total number of simulation measurements, respectively. In some cases, the validation of a simulation can be determined by comparing simulated behavior with that calculated from an analytic theory of known accuracy. Additionally, the simulation results can be compared to experimental data of simple fluids.(1; 2; 3; 4; 7) This comparison constitutes strong circumstantial evidence. The following simulations were validated in this manner. In chapters III and IV, the density profiles were compared with prior simulation data and found to be consistent. In chapters V and VI, the simulation results were compared to established simulation data as well as features observed by infrared and ellipsometric spectroscopy.

III.0 A LOOK AT SURFACE TENSION USING MD SIMULATION

III.1 INTRODUCTION

In this chapter, we use MD simulation to provide a study of L-J immiscible fluids and surface tension.[1] The planar interface between two liquids having two degrees of affinity to mix is studied. The surface tension is calculated from the normal, $\mathbf{P}_N$, and transverse, $\mathbf{P}_T$, components of the pressure tensor $\mathbf{P}$ for a wide range of temperatures. An unusual increase in surface tension with increasing temperature at constant volume of the total system is attributed to a pressure induced void transfer mechanism that is justified by thermodynamic arguments. This effect is diminished on the addition of a modest attractive potential between the two species, and there is a turnover point at higher temperatures beyond which the surface tension decreases with increasing temperature. An order parameter is identified as the gradient of the mole fraction distribution through the interfacial region. An additional effect is the dramatic inversion of the kinetic and potential contributions to the $\mathbf{P}_N$ profile as the temperature is varied. It is found that a commonly used approximation for $\mathbf{P}$, the Irving-Kirkwood 1 or (IK1) method, results in a relatively modest unphysical variability in $\mathbf{P}_N$ that weakly violates the condition of local mechanical stability. However, this artifact does not prevent the (IK1) method from producing an interfacial tension which is nearly identical to that derived from the complete IK formulawith no additional approximations.

---

[1] This chapter is a variant of the paper published in *Journal of Chemical Physics* **Vol 120**, 2893 - 2900 (2004).

III.2 THE PRESSURE OR STRESS TENSOR

The pressure field **P** in an inhomogeneous fluid is anisotropic and has the form of a tensor that depends on spatial direction and position while remaining independent of the orientation of the surface element with which it is associated.(23) It is also known that **P** can be represented as the sum of an isotropic kinetic part, $\mathbf{P}_K$, and a virial or potential part, $\mathbf{P}_U$. The kinetic part, $\mathbf{P}_K$, has the form

$$\mathbf{P}_K = k_B T \sum_{species} \rho_i(r)\mathbf{I} \tag{III.1}$$

in which $\rho_i(r)$ is the local density of species i at position **r** and the summation is over all species. The kinetic contribution to **P** has the form of a local ideal gas equation of state associated with the momenta carried by the centers of mass of the particles. The direct interaction or potential part of **P** arises from the intramolecular and intermolecular forces and is associated with the distribution of potential energy in the space enveloping pairs or higher order clusters of interacting molecules. The pressure tensor is defined through an infinitesimal force d**F** acting through an infinitesimal surface element d**A(r)** located at the position **r**.

$$d\mathbf{F}(r) = -d\mathbf{A}(\mathbf{r}) \cdot \mathbf{P}(\mathbf{r}) \tag{III.2}$$

With the stipulation in the Irving Kirkwood theory(24) that the pair-wise additive potential part of the stress between any pair of molecules be concentrated along the straight line connecting the centers, an assumption which is intuitively appealing but which has been shown to be quite arbitrary, the normal, $\mathbf{P}_N$, and tangential,$\mathbf{P}_T$, components of **P** associated with a planar interface then assume the (IK) form(25)

$$P_N^{IK}(z) = \rho(z)k_B T - \frac{1}{2A}\Big\langle \sum_{i\neq j} \frac{|\, z_{ij} \,|}{r_{ij}} U'(r_{ij})\Theta\Big(\frac{z-z_i}{z_{ij}}\Big)\Theta\Big(\frac{z_j - z}{z_{ij}}\Big)\Big\rangle \tag{III.3}$$

$$P_T^{IK}(z) = \rho(z)k_B T - \frac{1}{2A}\Big\langle \sum_{i\neq j} \frac{x_{ij}^2 + y_{ij}^2}{r_{ij}} \frac{U'(r_{ij})}{|\, z_{ij} \,|}\Theta\Big(\frac{z-z_i}{z_{ij}}\Big)\Theta\Big(\frac{z_j - z}{z_{ij}}\Big)\Big\rangle \tag{III.4}$$

where $\rho(z)$ is the system density at z averaged over the x and y coordinates. A summation over species is implied for $\rho(z)$, the coordinate z is orthogonal to the interface, the angular brackets indicate a statistical average, and the sum over *(i,j)* pairs automatically includes multiple species. $\Theta(x)$ is the Heaviside step function which is unity for positive x (where x is the argument in parenthesis) and vanishes for x less than or equal to zero, A is the area of the interface and the sup prime designates differentiation with respect to the coordinates in parenthesis. The product of the step functions ensures that the contribution to the pressure tensor across an infinitesimally thin plane located at z from any pair of molecules requires that they be located on opposite sides of the mathematical plane located at z.

There also exists in the literature a commonly used expression for P that takes the so-called (IK1) form (24; 25; 26)

$$P^{IK1}(z) = \rho(z)k_BT\mathbf{I} - \frac{1}{2A}\Big\langle \sum_{i\neq j} \frac{\mathbf{r_{ij}r_{ij}}}{r_{ij}} U'(r_{ij})\delta(z_i - z)\Big\rangle \tag{III.5}$$

Note that the Dirac delta function rather than the Heaviside step function appears in the statistical average. This implies that the IK1 pressure tensor profile consists of averages taken over a succession of co-planar infinitesimal slabs. In the first term of equation (III.5), $\rho(z)$ again represents the system density, k_B the Boltzmann constant, T the temperature, and $\mathbf{I}$ is the identity matrix. The second term terms A, r, V, z are interfacial area, radial distance, potential, and the z-component of the position respectively. Instead of a series of half-spaces separated by mathematical planes, the system is divided into thin slabs of a very small thickness. Within the past few years, the relation between Eq. (III.5) and Eqs. (III.3) and (III.4) has been explored in considerable detail, both theoretically and by MD simulations on various fluids in the proximity of hard walls.(25; 26; 27; 28; 29; 30; 31). The conclusion is that Eq (III.5) represents a first-order Taylor series expansion of the more rigorous IK form, Eqs. (III.3) and (III.4), in the relative spatial positions of molecules; furthermore, it is known that this expansion tends to converge quite slowly.

The macroscopic stress or pressure tensor is generally expressed as a summation over the entire system

$$P_{\alpha\beta} = \frac{1}{V}\Big(\sum_i m_i v_{i\alpha} v_{i\beta} - \sum_i \sum_{j>i} r_{ij\alpha} \frac{\partial U_{ij}}{\partial r_{i\beta}}\Big) \tag{III.6}$$

where $P_{\alpha\beta}$ represents the β component of the force acting on a unit area in the αplane and (α, β) assumes values (x,y,z). In equation (III.6), m,v, and V are defined as mass, velocity, and volume respectively. U_{ij} and r_{ij} are the potential energy and distance between particles

i and j. The pressure tensor is defined as an infinitesimal force acting through a surface element located at an arbitrary position. Though various mathematical expressions for the pressure tensor have appeared in the literature, it has been recognized that the differences in form arise from different assumptions about the distribution of potential energy residing in the space between interacting particles. However, correct formulations of $\mathbf{P}$ must always yield identical results for the interfacial tension.(27; 28; 29; 30; 31; 32)

On the other hand, it has also been recognized that despite the severity of the approximation generated by (IK1), the reduced surface tension γ^*, which can be expressed as the integrated z-profile difference between $\mathbf{P}_N$ and $\mathbf{P}_T$, the normal and transverse components of the of the pressure tensor

$$2\gamma^* = \int_0^z \left[\mathbf{P}_N(z) - \mathbf{P}_T(z)\right] dz \tag{III.7}$$

is invariant with respect to the interchange of the (IK) and (IK1) expressions for P.(26; 29; 30; 31) The factor of two in Eq. (III.7) arises from the fact that, because of the periodic boundary conditions, each cell contains a pair of co-planar interfaces. Insofar as our simulation incorporates the periodic replication of a unit cell which contains a pair of co-planar interfaces, an oriented binary fluid lamellar system is produced.

III.3 MODEL AND SIMULATION PROPERTIES

We consider an asymmetric two-component mixture of both partially miscible and fully immiscible Lennard-Jones fluids. (6; 7) Simulations are performed in a parallelepiped of volume $L_x \times L_y \times L_z$ with $L_x = L_y$ and $L_z \geq 2L_x$. The volume contains two slabs of immiscible liquids, one of N_1 particles and the other of N_2 particles (where the subscripts *1* and *2* denote the system components). Here, we take $N_1 = N_2 = 1000$ so that $N = N_1 + N_2 = 2000$in this case. The system is subjected to periodic boundary conditions (pbc) in the x,y, and$z$ directions. Due to these conditions, two planar interfaces of area L_x^2 are created during equilibration. We consider the z direction perpendicular to the interfacial regions. The particles interact via the following modified L-J potentials

$$U_{11} = 4\epsilon\Big[\Big(\frac{\sigma}{r}\Big)^{12} - \Big(\frac{\sigma}{r}\Big)^{6}\Big] \tag{III.8}$$

$$U_{22} = 2U_{11} \tag{III.9}$$

$$U_{12} = 4\epsilon\Big[\Big(\frac{1.2\sigma}{r}\Big)^{12} - \alpha\Big(\frac{\sigma}{r}\Big)^{6}\Big] \tag{III.10}$$

where ϵ and σ are the well depth and interaction range parameter, respectively (see Figure 3.1). Species *2*, with a potential well depth set at twice that of species *1*, is the less volatile component, while the factor 1.2σ in U_{12} ensures sharp interfaces and tends to minimize finite system size effects. The like-species interactions were chosen to mimic the argon-krypton system, whereas the unlike-species interaction was adjusted to vary the degree of miscibility. In this work, the variable α, which takes the values 0 and 0.5, controls the thickness of the interface, or more precisely, the system miscibility via unlike particle attractive interaction. The primary reason for this behavior is that the like particle interactions are stronger and more favorable energetically. Therefore, a strongly repulsive interaction ($\alpha = 0$) causes the fluid to reflect immiscible characteristics, while an increase in α increases the tendency for the two fluids to mix. Initially, particles were evenly distributed with an infinitely sharp interface parallel to the *z*-direction as shown in Figure 3.2. A truncated potential with an interaction range of 4σ was employed in these simulations. An assessment of potential truncation artifacts is presented below. As will be discussed, a sharp interfacial profile tends to amplify such artifacts. The microcanonical (NVE) ensemble was used to equilibrate the system and make production runs. Since an MD simulation allows particles to move somewhat freely, we will see that a pressure increase will force particles from the bulk to the interfacial region. We could also view this particle movement as a void volume being transferred from the interface into the bulk region. With this idea in mind, we see that this ensemble selection will also allow us to treat the void volume, V_m ,as a third component. The initial velocities of all particles were set to zero. The box dimensions are $L_x = L_y = 8.38\sigma$ and $L_z = 40.0\sigma$. Once the simulation is turned on, we used a velocity scaling factor to drive the system to a desired temperature. Using the initial configuration discussed above, two interfaces form having a surface normal oriented *perpendicular* to the long direction. Figure 3.3 displays

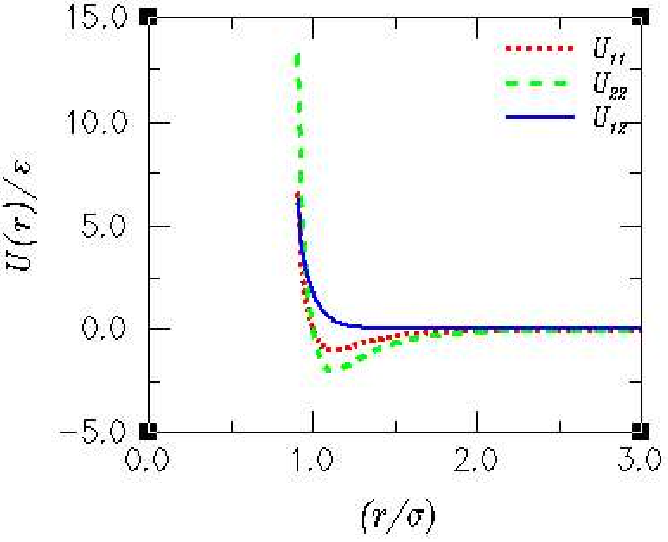

Figure 3.1: L-J potential functions for like and unlike species with α=0. The repulsive potential associated with the unlike interaction is reduced by a factor of 20.

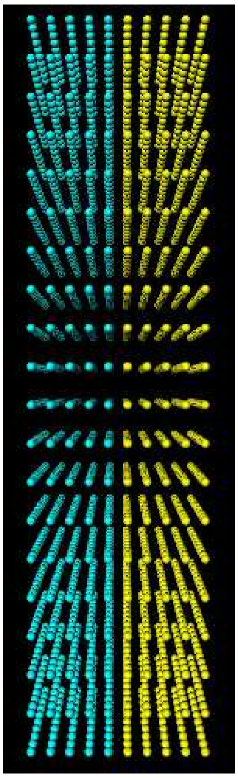

Figure 3.2: Initial particle distribution. The interface is initially parallel to the z-axis.

that the periodic boundary conditions causes the formation of two interfaces. The criteria for system equilibration were that the kinetic energy, and hence, temperature fluctuations were stationary and small. We define m as the particle mass in atomic mass units (amu), and for simplicity, the masses are set equal to unity. For all cases studied, the two fluids are quite immiscible. The system bulk densities (0.713) are lower than the triple point density for argon (0.85). Using reduced units, we are also able to represent the following reduced thermodynamic quantities: $T^* = \frac{k_B T}{\epsilon}$ for temperature,$\gamma^* = \frac{\gamma\sigma^2}{\epsilon}$ for surface tension, and $\rho^* = \rho\sigma^3$ for density, with $\rho = \frac{N}{V}$. The Beeman algorithm(6; 7) is used to integrate the equations of motion with an integration time step of $\triangle$ t $= .01$, which corresponds to twenty femtoseconds using the argon scale. Our equilibration runs were 6×10^5 time-steps (twelve nanoseconds) long while the collection runs were 1×10^4 time-steps (0.2 nanoseconds) long. During the simulation, the bulk phase densities increase slightly as the interfacial region has a decreased density.In order to ensure conservation of linear momentum and to prevent interfacial drift, the center of mass momentum in x, y, and$z$ directions is checked and reset to zero every 25 time-steps. Configuration files are updated every 1000 time steps while the stress and density profiles are updated at the end of each run.

III.4 SIMULATION RESULTS

Simulations of a liquid in contact with its vapor done by Daiz-Herrera and others(14; 35) indicated the presence of a brief plateau or possible nonmonotonic behavior in the (γ^*, T^*) and even in the (p^*, T^*) planes for the strongly non-mixing case, $\alpha = 0$, in the reduced temperature range (1.8-25.0)where p^* is the reduced hydrostatic pressure. As will be discussed later, pronounced nonmonotonicity in the (γ^*, T^*) plane has been reported for an MD simulation of a similar system in which the two unlike components have a modest ($\alpha = 0.5$) attractive interaction.(14) This motivated us to introduce two degrees of attraction between unlike species, corresponding to $\alpha = 0$ and 0.5, as shown in Figure 3.4, the (p^*, T^*) and $(\triangle p^*, T^*)$ for $\alpha = 0.5$,0 respectively. The pressure versus temperature plots for $\alpha = 0$ and 0.5 literally overlapped so we have used the difference, $\triangle p^*$, to prevent redundancy where

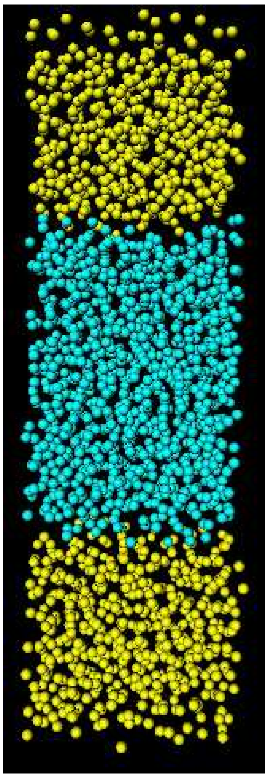

Figure 3.3: Final system configuration after equilibration is reached and prior to data collection.

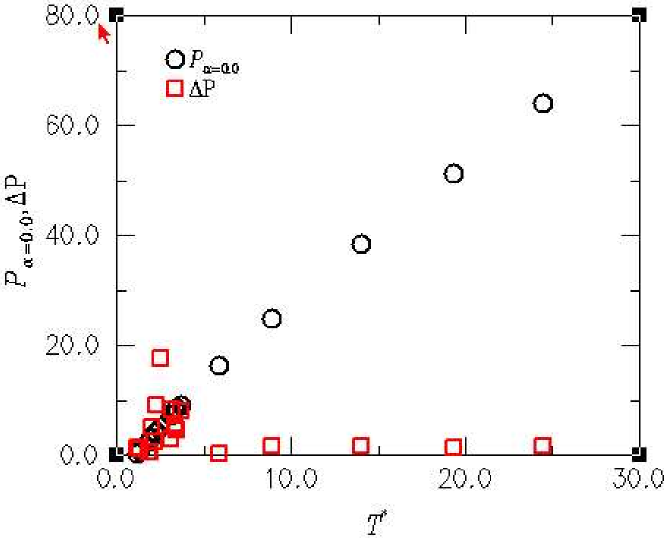

Figure 3.4: Pressure, and ΔP vs. temperature where ΔP is the difference between the pressures at $\alpha = 0$ and $\alpha = 0.5$ respectively. ΔP is multiplied by a factor of 10 here for visualization.

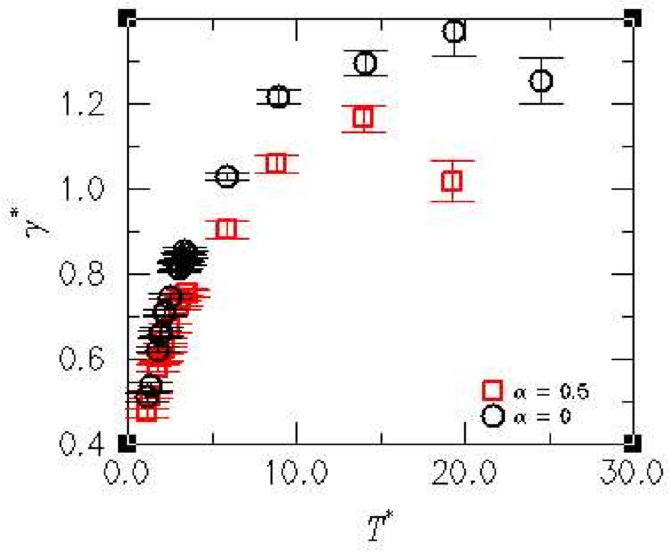

Figure 3.5: Surface tension vs. Temperature for $\alpha = 0$ and $\alpha = 0.5$.

$$\triangle p^* = p_0\Big(1+ \mid p^*_{\alpha=0} - p^*_{\alpha=0.5} \mid \Big) \tag{III.11}$$

As shown in Figure 3.4, both the p^* and $\triangle p^*$ behavior are very close to linear. This implies that the bulk thermodynamic properties of these binary fluid mixtures are remarkably insensitive to the degree of attraction between unlike species, at least for the reduced density ρ^*=0.713. On the other hand, as demonstrated in Figure 3.5, the interfacial tension, while increasing monotonically and approximately linearly with increasing T^* for small $(1.8-5.0)$ values of reduced temperature, exhibits a systematic decrease on the order of 15% as α varies from 0 to 0.5. Apparently the interfacial tension is much more sensitive to certain features of the intermolecular potential than is the bulk pressure. Moreover, the (γ^*, T^*) plot (Figure 3.5) exhibits a maximum. The decrease in γ^* with increasing T^* is in accord with physical intuition and experimental observations concerning the temperature dependence of the surface tension of a pure fluid. This effect is clearly illustrated in Figure 3.6, in which the simulated surface tension of the least volatile component in equilibrium with its own vapor is plotted versus temperature. Note that γ^* decreases markedly with increasing T^* in the same region for which the interfacial tension of the immiscible binary fluid is increasing with

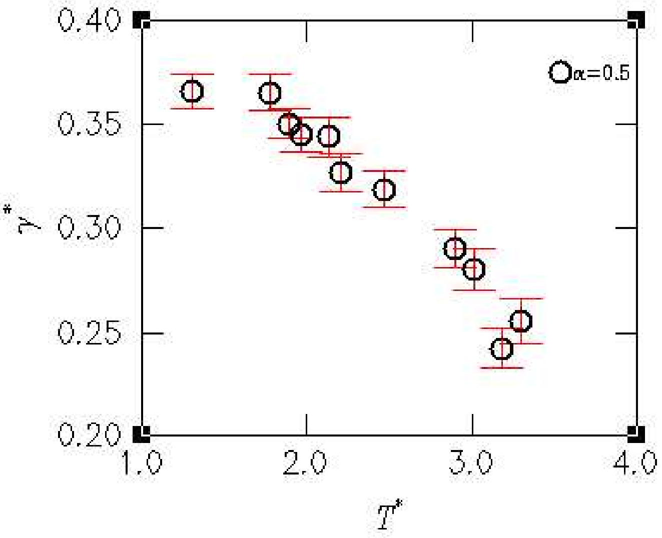

Figure 3.6: Surface tension vs. Temperature for $\alpha = 0.5$ for a simple L-J fluid in contact with its vapor. Note that, in contrast to the case of an immiscible binary fluid, γ^* decreases markedly with increasing T^*.

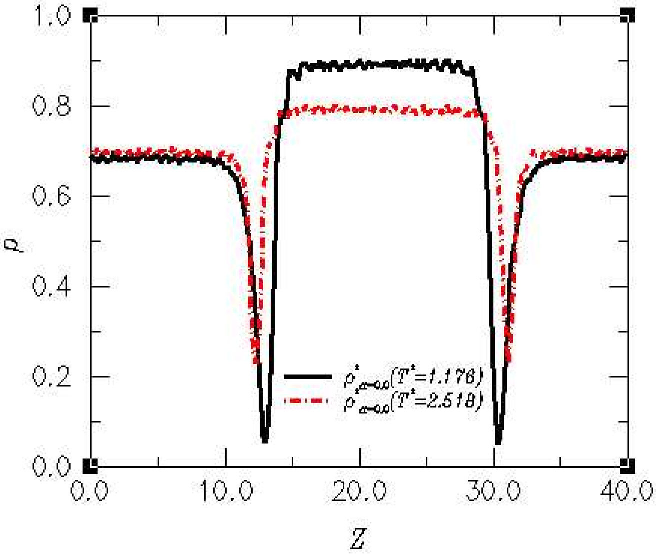

Figure 3.7: Interfacial density profiles for $\alpha = 0$ at $T^* = 1.176$ and 2.518. Note that the less volatile region expands as the temperature increases at an expense of the interfacial region.

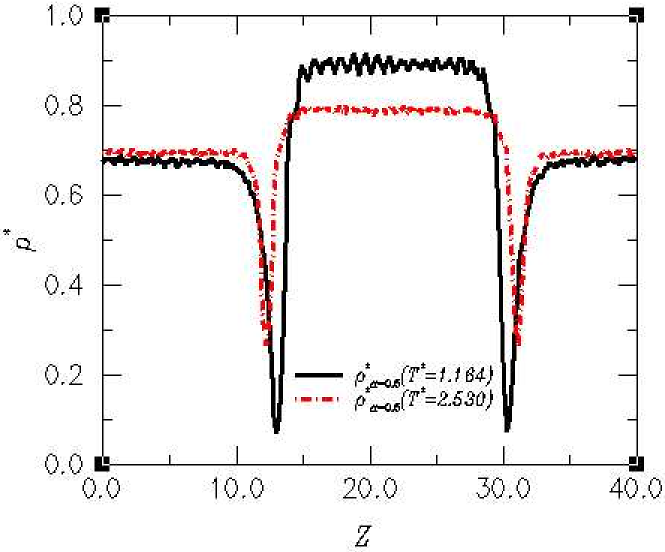

Figure 3.8: Interfacial density profiles for $\alpha = 0.5$ at $T^* = 1.164$ and 2.530. Note the similar expansion of the less volatile region; hence, the variable α does not noticeably affect the overall behavior of the less volatile region.

increasing T^*. This observation provides strong circumstantial evidence that the simulated behavior of the binary fluid is physically realistic and does not arise from an artifact in the simulation code or in its implementation.

In the case of an immiscible binary fluid, a surface tension maximum defines the conditions under which the temperature and pressure effects on γ^* are in balance. A further increase in T^* causes the interfacial density profile to broaden, thereby causing a decrease in γ^*.(36) In analogy with pressure, the density profiles across the interfacial region, as shown in Figures 3.7 and 3.8 , are not very sensitive to the value of α. However, they do exhibit systematic variations with temperature: the bulk density of the less volatile component , which has the higher density, decreases with increasing T^*, whereas the bulk density of the more volatile component is rather insensitive to T^*. Furthermore, both the width and maximum depth near the center of an interfacial profile clearly diminish with increasing but low temperature, and this shrinkage of the interfacial region coincides with an increase in surface tension. These effects are clearly exhibited in the distributions displayed in Figures 3.7 and 3.8. Note that as temperature increases to the left of the maximum in the surface tension, the profile minimum migrates away from the region occupied by the less volatile species. This behavior is as though the volume associated with the less volatile component were expanding at the expense of the interfacial volume, without, however, significantly affecting the density of the more volatile species. In selecting an order parameter that quantifies this, we should determine an operator: (1)which is a function of the dynamical variables in the system Hamiltonian and (2)whose ensemble average is zero in the homogeneous bulk phase and nonzero in the interfacial region. With these characteristics in mind, one can see from Figures 3.9 and 3.10 that derivatives of concentrations and mole fractions

$$\chi_1(z) = \frac{\rho_1(z)}{\rho(z)} \tag{III.12}$$

$$\chi_2(z) = 1 - \chi_1(z) \tag{III.13}$$

provide suitable order parameters.(36; 37; 38) From these figures, we see there is only a small effect due to changes in a, but these profiles broaden greatly as the temperature increases. As seen in the surface tension behavior as a function of temperature, mixing does occur above a particular region. This temperature enhanced species mixing should cause

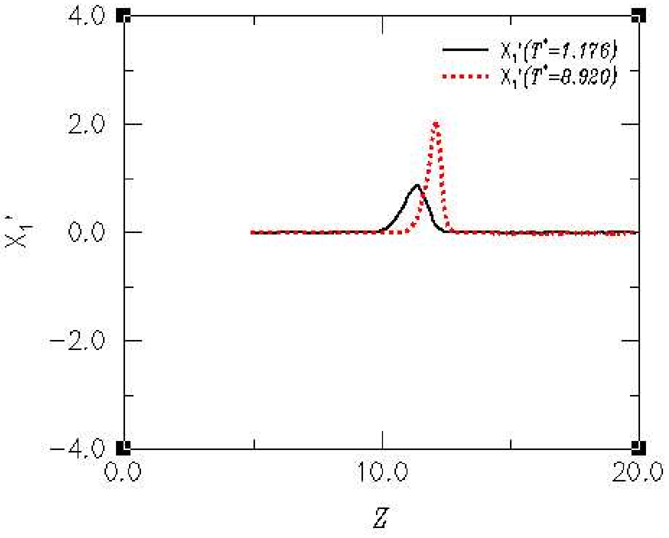

Figure 3.9: Mole fractions for α=0 at $T^* = 1.176$ and 8.920 respectively.

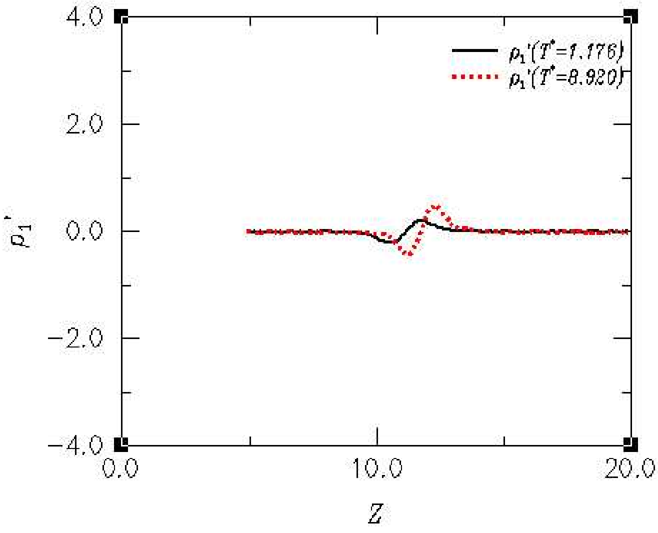

Figure 3.10: Total density derivative for $\alpha = 0$ at $T^* = 1.176$ and 8.920 respectively.

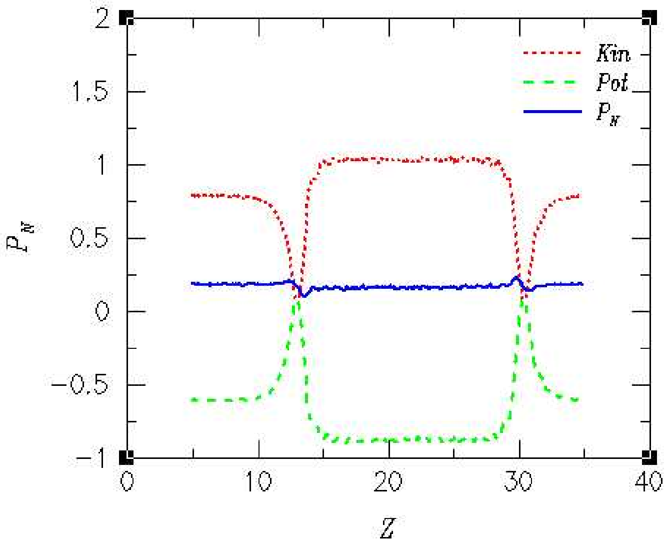

Figure 3.11: The kinetic and potential contributions to $\mathbf{P}_N^{IK1}$, the normal component of the interfacial pressure tensor profile, in the IK1 approximation for $\alpha = 0.5$ at $T^* = 1.165$..

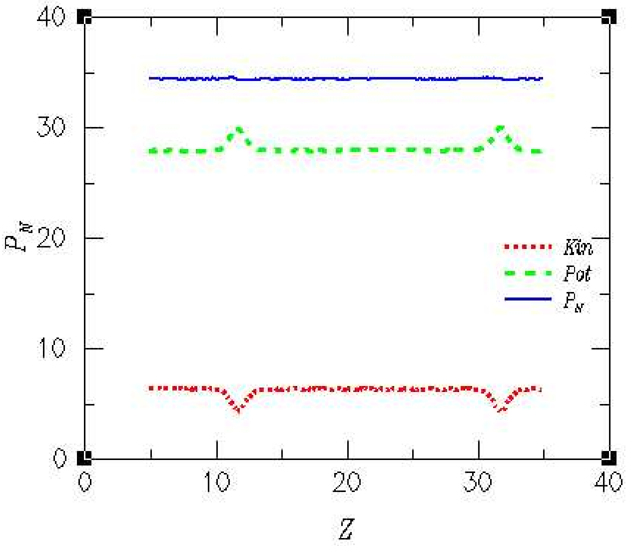

Figure 3.12: The kinetic and potential contributions to $\mathbf{P}_N^{IK1}$, the normal component of the interfacial pressure tensor profile, in the IK1 approximation for $\alpha = 0.5$ at $T^* = 8.821$.

a broadening of the order parameter profile as seen in comparing Figures 3.9 and 3.10, respectively. To simplify Figures 3.9 and 3.10, we have shown the qualitative behavior of one interface. Finally, in Figures 3.11 and 3.12 we present the kinetic and potential contributions to the $\mathbf{P}_N^{IK1}$ profile, the IK1 approximation to $\mathbf{P}_N^{IK}$, for two values of the reduced temperature. Note that the total normal component of the pressure tensor is not strictly constant through the interfacial region; this is an unphysical artifact associated with the IK1 approximation which has been recognized by others, and will be discussed briefly in the following section. More importantly, note the dramatic inversion of the kinetic and potential contributions to the normal component of the pressure tensor with respect to temperature. At the low temperature, $T^* \approx 1.16$ - 1.18, the kinetic contribution clearly dominates in the bulk phases of both components, whereas in the interfacial region the potential contribution is slightly larger. At the elevated temperature, however, the kinetic portion is much less than the positive potential contribution in both the bulk phases and in the interfacial region. Therefore, the total pressure is dominated by thermal motion at low temperatures and is controlled by repulsive molecular interactions at high temperatures.

III.5 DISCUSSION OF SIMULATION RESULTS

Our simulation results show that the (IK1) method is not consistent with the requirements of local mechanical stability as shown in Figure 3.11 (although it is easy to demonstrate that (IK1) is indeed consistent with global mechanical stability)(25) insofar as the component of the total pressure tensor profile which is normal to the interface, $\mathbf{P}_N(z)$, is not a constant. Indeed, it can be readily shown that for a planar interface, $\mathbf{P}_N(z)$ must be identical to the bulk hydrostatic pressure p for any distance z from the interface.(25) The argument is based on the observation that local mechanical equilibrium (the absence of net force) requires that the divergence of $\mathbf{P}$ vanish at each point in space, and also that the symmetry in P dictated by a planar interface requires that the z-derivative of $\mathbf{P}_{zz}$ be identically zero everywhere. On the other hand, the global stability property of zero net force acting on the entire system simply requires that the integral through the interfacial profile of this z-derivative vanish, which is obviously the case. The unphysical artifact associated with the (IK1) approximation for $\mathbf{P}$ has previously been observed in MD simulations of the interfacial regions of simple and polymeric fluids bounded by impenetrable, rigid walls(25; 29; 30; 31) and even in simulations on lipid bilayers in an aqueous environment.(39; 40; 41) In the cases involving walls, the variability of $\mathbf{P}_N(z)$ is much more pronounced than is seen for the binary fluid interface, which is consistent with physical intuition. It has also been recognized that the origin of this anomaly lies in the implicit assumption in (IK1) that the two particle density function $\rho_2^*(r_1; r_2)$ is translationally invariant with respect to the difference $(r_2 - r_1)$. While this symmetry is trivially exact for homogenous fluids and is approximately correct near critical points, it must break down for relatively sharp interfacial density profiles such as are generated in this simulation or inhomogeneous systems. In spite of this deficiency, it has been noted by others that the (IK1) approximation produces a surface tension identical to that generated by use of the full (IK) method.(25; 29; 30; 31)The unexpected increase in surface tension with increasing temperature deserves a few comments. While in the case of a single component system, one has(4)

$$\frac{d\gamma}{dT} = -S^\sigma \tag{III.14}$$

where S^σ, the interfacial or surface entropy, should be a positive quantity since $\frac{d\gamma}{dT} < 0$ for that case . As a check, we performed MD simulations of a pure $L-J$ fluid in equilibrium with its vapor and observed that γ does indeed decrease with increasing T. One way of describing the situation for a multi-component system is to recognize that thermodynamics provides a simple relation between how the entropy of the entire system changes with interfacial area and the temperature dependence of the surface tension.(4)

$$\left(\frac{\partial S}{\partial A}\right)_{T,V,n_i} = -\left(\frac{\partial \gamma}{\partial T}\right)_{V,A,n_i} \tag{III.15}$$

The LHS term of Eq(III.15) multiplied by T is the heat reversibly extracted from a thermal reservoir upon increasing the interfacial area by ∂A at constant T, V, and composition n_i. The point is that an increase in γ with increasing T implies that heat is actually transferred into the reservoir as the interfacial area increases, inasmuch as the systems entropy is reduced. Such an effect appears to be unphysical because it implies that for a microcanonical system increasing the interfacial area creates work. Another apparently unphysical implication is that the surface entropy associated with an increase in interfacial area is a negative quantity. A striking exception to this intuitive conclusion has been experimentally confirmed in the cases of certain liquid metals (Cu, Zn, Cd) in equilibrium with their vapor phase. It has been conjectured that the liquid surface of these metal is virtually crystalline.(42)At this point it should be recalled that as our simulations were performed in the (NVE) ensemble, an increase in the total energy E is accompanied by both a rise in the internal pressure p as well as temperature. Indeed, as Figure 3.4 shows, p and T are highly correlated; therefore, it appears that the key to understanding the temperature dependence of surface tension in our simulations lies in understanding the dependence of γ on p. Consider the Gibbs thermodynamicpotential dF that includes the effects of surface tension in thepresence of multiple components:(39; 4)

$$dF = -SdT + Vdp + \gamma dA + \sum_i \mu_i dn_i \tag{III.16}$$

Note that (A, p) cross differentiation applied to this expression yields

$$\frac{\partial}{\partial p}\left(\frac{\partial F}{\partial A}\right)_{T,p,n_i} = \frac{\partial}{\partial A}\left(\frac{\partial F}{\partial p}\right)_{T,A,n_i} \tag{III.17}$$

which states that the rate of change with p of the *(F, A)* coefficient is equal to the rate of change with A of the *(F, p)* coefficient. This is a necessary and sufficient condition for Eq (III.16) to be an exact differential form. From Eq (III.16) we are able to obtain the identities

$$\gamma = \left(\frac{\partial F}{\partial A}\right)_{T,p,n_i} \tag{III.18}$$

$$V = \left(\frac{\partial F}{\partial A}\right)_{T,A,n_i} \tag{III.19}$$

which we can then substitute Eq (III.18) back into Eq (III.17) to find; i.e.,

$$\left(\frac{\partial \gamma}{\partial p}\right)_{T,n_i} = \left(\frac{\partial V}{\partial A}\right)_{T,n_i} \tag{III.20}$$

The basic thermodynamic reasoning of Eq(III.20)tells us that for a fluid in contact with a gas or some other fluid which has absolutely no tendency to be adsorbed, but which exerts a pressure p on the system, the following relation holds:(43)

$$\left(\frac{\partial\gamma}{\partial p}\right)_{T,n_i} = \left(\frac{\partial V_m}{\partial A}\right)_{T,n_i} \tag{III.21}$$

where A denotes the surface area and V_m is the molar volume. By surface area, we are referring to the interfacial area, and the molar volume is the volume available for a molecule to occupy either in the bulk or the interfacial region of that particular fluid. In other words, the isothermal transfer of a molecule from bulk phase to the surface results in an increase in surface tension since V_m, an incremental change in the molar volume, must be a positive quantity because the volume available for the remaining particles in the bulk to occupy increases. This is so because the transfer process creates a void in the bulk that is then shared by the remaining molecules in the interior. Another way of casting this is to assert that an incremental pressure increase must induce the transfer of an increment of void volume V_m from surface to interior in order to create the incremental surface area dA at the interface, which results in a surface tension increment $d\gamma$. In this instance the notion of a void volume increment follows directly from the molar volume increment, and so there is no thermodynamic ambiguity. In particular, it is not necessary to formally introduce the concept of a surface volume into a thermodynamic description. Lewis and Randall(36), in the discussion on p.460 which deals with the interface of a binary fluid, refrain from a physical interpretation of Eq (III.21) which relates the pressure dependence of surface tension to the interfacial area dependence of the system volume. In addition to a void transfer process, this equation can also be interpreted either as a pressure-induced droplet expansion or as an emulsification (droplet break-up) effect that is accompanied by an overall volume expansion. Note that in our simulations the total volume is conserved, and so V_m assumes a role similar to that of a separate stable material species. The fact that the increase of γ with increasing T in our (NVE) simulations is accompanied by a decrease in both interfacial width and depth with a sharp dip in total density in the center of the interfacial profile, as shown in Figures 3.7 and 3.8, lends further support to an interpretation of this effect in terms of a void transfer mechanism. Direct confirmation of these ideas has proven to be rather frustrating according to the conclusions of Stecki and Toxvaerd.(38; 37; 44) Turkevich and Mann were able to provide experimental data on the isothermal dependence of surface tension on pressure and on the pressure dependence of interfacial density profiles for water-n-alkane systems which are in accord with our simulation results.(33; 34) It should also be mentioned that our system potential resembles that of Stecki and Toxvaerd(44; 43) who performed MD simulations of a simple, immiscible, symmetric binary fluid. They also constructed a theory which approximates the low temperature interfacial structure as a vacuum sheet or gap separating a pair of homogenous interacting slabs, each slab consisting of a pure fluid component. For pressures not too high, they find a strong tendency for the gap width to contract as pressure increases, which is in accord with our simulation findings. At low temperature, they also find a clear tendency for the surface tension to increase with increasing pressure. In contrast with our results they note the presence of density oscillations which extend from the interface well into the bulk: we attribute this discrepancy to the fact that the bulk density for our system, $\rho \approx 0.713$, is 12% lower than theirs, so in our case there is a reduced tendency for the fluid to order near the interface. They also report on a relatively novel phenomenon that may apply to fluid lamellar systems in general; namely, the existence of a soft or low frequency breathing mode associated with oscillations in the interfacial width or gap thickness. Another recent study by Diaz-Herrera et al.(14; 45) focuses on an MD (NVT-ensemble) simulation of binary and ternary mixtures of partially miscible Lennard-Jones fluids. Their main result, which is relevant to the present study, is that the interfacial tension of the binary fluid exhibits nonmonotonic behavior as a function of temperature. At sufficiently low temperatures, they observed an increase in the molar volume of a given species with increasing T that coincides with an increase in P as well as an increase in γ. They also report a pronounced turnover in $\gamma(T)$, where the surface tension is markedly reduced with increasing T beyond a rather sharply defined temperature. The surface tension maximum is the consequence of a balance between pressure induced interfacial contraction and temperature induced interfacial broadening. Our simulation results are consistent with these observations. In contrast to the Diaz-Herrera et al. study, there is considerable asymmetry between the like-like interactions in our system, the like-unlike interactions in the two simulations do not match closely, and the density of our system is somewhat lower than theirs. Nevertheless, from a rough comparison between the two it seems legitimate to infer that the sensitivity of the surface tension of even simple binary fluids to thermodynamic conditions may be non-trivial.At this point it should be noted that Lifschitz and Freed (L-F) (46; 47)have developed a variational-perturbational lattice theory of compressible polymer blend interfaces that predicts that for a fixed reduced temperature $\frac{T}{T_c}$, where T_c is the critical temperature, the interfacial tension may increase with increasing pressure. Their theory also predicts that, in this case, the width of the interface should decrease with increasing pressure. The physical mechanism in the (L-F) theory underlying these effects seems to be that vacancies or void regions (excess free volume regions) are considered as a separate species, and that increasing the external pressure on the blend causes this component to migrate from the interface into the interior, thereby giving rise to a surface deficiency. Since this is a negative quantity, it may be of sufficient magnitude to induce an increase in γ with increasing p. At any rate, the similarities between our MD results for a monatomic binary fluid and the predictions of the (L-F) lattice theory of compressible polymer blends suggest a simple explanation, common to both systems, in terms of a void transfer process.In addition to the surface entropy S^s one can define a surface energy E^s and even a surface specific heat C_V^σ.(4)

$$E^\sigma = \gamma - T\left(\frac{\partial\gamma}{\partial T}\right)_{A,V,n_i} \tag{III.22}$$

$$C_V^\sigma = \left(\frac{\partial E^\sigma}{\partial T}\right)_{V,A,n_i} \tag{III.23}$$

where E^σ can be regarded as the irreversible heat generated by an instantaneous decrease in interfacial area (spontaneous deemulsification) at constant temperature, volume, and composition. The physical meaning of the surface specific heat is somewhat obscure; it can be formally regarded as the response of the surface entropy or energy to thermal changes. According to Figure 3.5, in the context of our simulation, the specific heat, C_V, is a small positive quantity and has a maximum at the turnover of the surface tension γ^* vs. T^* plot.We anticipate that a very sharp interfacial profile implies significant corrections to the simulated surface tension because of the smooth truncation of the Lennard-Jones potential at a distance R_c.(48; 49; 50) An upper bound on this correction can be shown to have the form

$$\gamma_{tail} = \frac{3\pi}{2R_c^2}\left[\epsilon_{AA}\rho_A^{*2} + \epsilon_{BB}\rho_B^{*2} - \epsilon_{AB}\rho_A^*\rho_B^*\right] \tag{III.24}$$

where $\rho^* = \rho\sigma^3$ and ϵ_{ii} are the $L - J$ parameters. The assumptions underlying Eq (III.24) are that the various bulk radial distribution functions may be taken to be unity beyond the cut-off, that the bulk fluid densities are relatively insensitive to the cut-off, and that the interfacial density profiles for both species are infinitely sharp. Since R_c is set at 4σ in our simulations, it is easy to see that the surface tension can be enhanced by as much as a factor of two by these long-range interactions. In addition, the fact that the bulk densities are observed to decrease with increasing pressure implies that the pressure dependence of the interfacial tension is moderated by this correction. Table 3.1 contains maximal tail corrections to the surface tension for various values of T^* and α.

As a final note, we include a crude estimate of the importance of thermally excited capillary waves on the width w of the interfacial profile:(26; 51)

$$< w^2 >= \frac{k_B T}{2\pi\gamma_{tail}} \ln\left[\frac{L}{\sigma_0}\right] \tag{III.25}$$

where $< w^2 >^{1/2}$ is the equilibrium average width, $L^2 = A$, σ_0 is a short-range cut-off that defines a minimum wavelength, and γ_{tail} is the surface tension associated with step function interfacial density profiles. Fisher and Gelfand(51) have concluded that caution should be used with any quantitative predictions of a capillary wave model that is sensitive to how the short-wavelength fluctuations are handled, but that those predictions following from consideration of the long-wavelength modes alone are most probably widely applicable. Eq (III.25), which predicts a logarithmic divergence in the interfacial width as the surface area increases, is rather ad hoc in the sense that σ_0 is not uniquely specified and γ_{tail} depends on the value of R_c, so that by suitable choices of these parameters the entire interfacial width can be ascribed to capillary wave excitations. By setting both cut-off lengths at 4σ we find modest though non-negligible values for the capillary wave contribution to the interfacial width in the range (0.47-0.92)σ. If both cut-off lengths are set at σ the capillary wave effect becomes negligible.

Table 3.1: Maximal Long-Range Tail Corrections to the Interfacial Tension as a function of T^* and α. ρ^*_A and ρ^*_B are the density components of species A and B respectively.

α	T^*	ρ^*_A	ρ^*_B	γ_{tail}
0.0	1.176	0.671	0.900	0.6097
	2.0053	0.692	0.808	0.5256
	3.0574	0.704	0.80	0.5034
0.5	1.1646	0.675	0.888	0.5104
	2.0068	0.688	0.813	0.4463
	3.0333	0.704	0.775	0.4194

IV.0 MD TEST OF THE JARZYNSKI RELATION APPLIED TO INTERFACIAL TENSION

IV.1 INTRODUCTION

Molecular Dynamics simulation has been used for the past 20 - 30 years to study interfacial properties of liquids though the foundation for these studies were laid as far back as 1791 when the astronomer Joseph Dalambre used the time reversible algorithm, commonly called the Verlet algorithm, for the integration of Newton's equations.(52) Some of the properties obtained from Molecular Dynamics (MD) simulation are density profiles, system configurations, as well as stress or pressure tensor profiles. Usually, the surface tension is calculated by integrating the microscopic stress tensor profile over the interfacial region. J.G Irving and J.H. Kirkwood derived a relationship, based on two-body interactions, between the microscopic stress and the kinetic and potential energies of the system.(53) Subsequent simplifications of the Irving-Kirkwood method of determining the stress tensor have been made to decrease simulation times; however, the surface tension - microscopic stress tensor profile connection has remained. As stated in the Pressure and Stress Tensor section of the previous chapter, the IK1 formulation of the stress tensor consists of averages over co-planar infinitesimal slabs, or bins, instead of planes. The stress tensor provides a microscopic description of the pressure which helps determine the behavior of a system in the bulk as well as the interface. An interface breaks the homogeneity of a system and the IK1 expression becomes less accurate due to unphysical oscillations of the normal stress component.(25) It would be very beneficial to develop a method to determine free energy which circumvents the stress tensor calculation and the technical difficulties associated with extensions to include many-body interactions of more complex systems. In an effort to do this, I implemented an equality recently developed by C. Jarzynski. This equality uses an ensemble average of a set of non-equilibrium simulations to calculate equilibrium free energy differences of a system subjected to a time-dependent perturbation of tis Hamiltonian. To apply the Jarzynski relationship by simulation requires that the Hamiltonian of the system be changed as a function of time by some external parameter. This external parameter will be discussed and identified later in this chapter.

IV.2 THE FREE ENERGY-WORK CONNECTION

Calculating differences in equilibrium free energy has been of interest for some time, and biological applications of these energy calculations are of particular importance. An example of these applications are the desirability to estimate the free energy changes resulting from the irreversible stretching of M-RNA.(54) Equilibrium free energy differences are generally difficult quantities to obtain from computer simulations.(55) Recently, C. Jarzynski was able to show that there is an exact relation between the nonequilibrium average of work and the equilibrium free energy difference associated with a change in the Hamiltonian of the system.(9) Development of efficient methods to numerically estimate free energy differences still remains one of the outstanding problems of computational physics.(56; 57) Several attempts to directly apply Jarzynski's relation showed that the computational efficiency depends on the method used to change the Hamiltonian.(7; 54; 58; 59)

Work is a fundamental concept of thermodynamics, and efforts to understand how and why it affects bodies in nature have been undertaken for over a century. Consider the work, dW, done on a body in an infinitesimal *reversible* change when connected to a thermostat. The first law of thermodynamics states that if the system is allowed to interact with the thermostat, the resulting energy change can be written in the form

$$dW = dE - đQ \tag{IV.1}$$

Here, dE is the change in the internal energy of the body and $đQ$ is the change in the amount of heat contained in the body. The second law defines a state quantity, the entropy, related to $đQ$ by the quantity T, the temperature, by the relationship

$$dS = \frac{đQ}{T} \tag{IV.2}$$

If the system is not isolated, we can subsequently simplify Eq.(IV.1) since the temperature is constant to get

$$dW = dE - TdS = d(E - TS). \tag{IV.3}$$

Recall the relationship

$$F = E - TS \tag{IV.4}$$

where F is another thermodynamic function of the body known as the *Helmholtz free energy* (the energy available to perform work). From Eq.(IV.3, we see that the *work done* on a body in a *reversible* isothermal process is simply the change in its free energy. We know that the differential behavior is important in thermodynamics, so differentiating Eq.(IV.4) and substituting the combined form of the 1^{st} and 2^{nd} laws of thermodynamics:

$$dE = TdS - PdV \tag{IV.5}$$

where P is the pressure acting on the body and V is its volume, into Eq.(IV.4) we now get the differential form of the free energy

$$dF = -SdT - PdV \tag{IV.6}$$

From Eq.(IV.6) and Eq.(IV.4), we can easily express the energy in terms of the free energy.

$$E = F - T\left(\frac{\partial F}{\partial T}\right)_V = -\frac{\partial}{\partial \beta}\ln Z \tag{IV.7}$$

where Z is the system partition function. Knowing any of the quantities E, F, or TS as a function of the remaining two variables allows us to determine the remaining thermodynamic quantities by using the basic Maxwell relationships.(5)

The above discussion is mostly thermodynamic and macroscopic in nature, and in this chapter, I will show how MD simulations can help apply these concepts to a finite size system. The thermodynamic properties of a system may be determined from the system partition function. Since we assume our system obeys classical statistical mechanics, we need only the configurational contribution to the partition function. Zwanzig(60), arguably, spearheaded the use of simulations to calculate this configurational contribution, and I will outline his argument briefly here. Consider a system having N particles in a volume, V, and a total potential U_N. For a homogeneous and isotropic system, changing the shape of the container does not affect the energy of the system.(61) Once an interface has formed, the system is no longer isotropic or homogeneous so perturbations of the system Hamiltonian pertaining to the interface, i.e. changing the interfacial surface area, will have an effect on the properties that describe the system, especially the interface. For the analysis below, we are assuming Maxwell-Boltzmann statistics. The configurational free energy is given by

$$\exp(-\beta F_N) = Q_N = \int_V \cdots \int_V \exp(-\beta U_N) d\tau_1 \cdots d\tau_N \tag{IV.8}$$

where $\beta = \frac{1}{k_B T}$, U_N is a function of the configuration of the collection of molecules and $\int d\tau_i$ is an integral over the entire configuration space of the ith molecule. Assume that the system's potential energy can be separated into two parts:

$$U_N = U_N^0 + U_N^1 \tag{IV.9}$$

where U_N^0 is the potential energy of an unperturbed system and U_N^1 is the perturbation. The partition function and free energy of the unperturbed system from Eq (IV.8) is

$$\exp(-\beta F_N^0) = Q_N^0 = \int \cdots \int \exp(-\beta U_N^0) d\tau_1 \cdots d\tau_N \tag{IV.10}$$

For completeness, the probability of any particular configuration of the unperturbed system is

$$P_N^0 = \exp(-\beta(F_N^0 - U_N^0)) \tag{IV.11}$$

$$\int \cdots \int P_N^0 d\tau_1 \cdots d\tau_N = 1 \tag{IV.12}$$

Multiplying Eq. (IV.8) by Q_N^0 gives

$$\exp(-\beta(F_N - F_N^0)) \equiv \exp(-\beta F_N^1) = \big\langle \exp(-\beta U_N^1) \big\rangle_0 \tag{IV.13}$$

where F_N^1 is the free energy contribution from the perturbation, and the average is performed over the unperturbed ensemble so

$$\big\langle \exp(-\beta U_N^1) \big\rangle_0 = \int \cdots \int P_N^0 \exp(-\beta U_N^1) d\tau_1 \cdots d\tau_N \tag{IV.14}$$

Eq. (IV.13) is known as Zwanzig's *perturbation identity* and is the origin of many studies estimating free energy.(60) This equation is also the starting point of the scheme followed by C. Jarzynski(9) who used it to derive a relationship involving W, the nonequilibrium work, and the free energy

$$\Delta F = -\frac{1}{\beta} \ln \big\langle \exp(-\beta W) \big\rangle \tag{IV.15}$$

The brackets indicate an average with respect to the various phase space trajectories taken by the system going from an initial state to a final state, given that the system is initially at equilibrium. Equation (IV.15) says that we can extract equilibrium information, namely ΔF, from the ensemble of *nonequilibrium* or finite time measurements. Accurate numerical estimates of $\big\langle \exp(-\beta U_N^1) \big\rangle_0$ in Eq.(IV.14), is generally hard to realize because for any finite number of iterations, the average tends to be dominated by regions where $U_f \cong U_0$ (U_f and U_0 correspond to total energies of final and initial configurations).

If the work probability distribution is Gaussian (if the switching processes are very slow and the trajectories are close to reversible) then the free energy of switching becomes(60):

$$\Delta F = \overline{W} - \frac{\beta\sigma^2}{2} \tag{IV.16}$$

where

$$\sigma^2 \equiv \overline{W^2} - \overline{W}^2. \tag{IV.17}$$

Hermans(62) showed that the dissipated work

$$W_{diss} = (\overline{W} - \Delta F) \tag{IV.18}$$

is then related to the fluctuations in W by

$$W_{diss} = \frac{\beta\sigma^2}{2} \tag{IV.19}$$

If the fluctuations in W from one measurement to the next are much larger than k_BT, then $\left\langle \exp(-\beta W) \right\rangle$ will be dominated by certain regions where the values of W are far below $\overline{W}$. Since such values of the work represent statistically very rare events, it would require an unreasonably large number of measurements of W to accurately determine $\left\langle \exp(-\beta W) \right\rangle$.

One of the simplest and widely used methods of determining free energy differences between two states described by the classical Hamiltonians H_0 and H_1 is slow-growth thermodynamic integration.(58) The method of thermodynamic integration pioneered by Kirkwood is one way available to compute free energy, and it also allows the use of MD to directly apply the Jarzynski relationship.(63) In a computer simulation, a coupling parameter, call it λ, is varied such that the states λ=0 and 1 correspond to H_0 and H_1, respectively. This correspondence could be made by following a linear path in λ, i.e. $H_\lambda = H_0 + \lambda\delta H$. The derivative of the free energy with respect to λ is given by the canonical average in λ of the corresponding derivative of the Hamiltonian,

$$\Delta F = \int_0^1 \left\langle \frac{dH}{d\lambda} \right\rangle_\lambda d\lambda \tag{IV.20}$$

Equation (IV.20) forms the basis of thermodynamic integration. In computer simulations, $\left\langle \frac{dH}{d\lambda} \right\rangle_\lambda$ can be calculated for a few values of λ and combined by numerical integration formulas. Alternatively, λ, the coupling parameter, can be increased in discrete steps from 0 to 1 in the course of a simulation. As λ is changed, the accumulated work performed on the system is

$$W_{0\to 1} = \sum_{i=0}^{N-1} \left\langle H_{\lambda_{i+1}}(\mathbf{x}_i) - H_{\lambda_i}(\mathbf{x}_i) \right\rangle_{\lambda_i} \tag{IV.21}$$

This expression is for a path of discrete coupling-parameter values

$$\lambda_0 = 0, \lambda_1, \lambda_2 \cdots, \lambda_{N-1}, \lambda_N = 1 \tag{IV.22}$$

The variable $\mathbf{x}_i$ represent discrete trajectories in phase (or configuration) space with equations of motion according to the time-dependent Hamiltonian, H_{λ_i}. The increment

$$\left\langle H_{\lambda_{i+1}}(\mathbf{x}_i) - H_{\lambda_i}(\mathbf{x}_i)\right\rangle_{\lambda_i} \tag{IV.23}$$

is evaluated at the state $\mathbf{x}_i$. In the limit of an infinitely slow change of the coupling parameter, the work is reversible and identical to the free energy change. Algorithms for varying λ have been discussed in detail previously(9; 58; 59), and the general procedure begins with the generation of an ensemble of equilibrium configurations ($\lambda = 0$). There are basically three steps to follow once these have been generated. First, select a configuration from the equilibrium ensemble. Next, increment the potential energy function by changing λ_i to λ_{i+1} . Finally, relax the system at the λ_{i+1} value. This is repeated until the final coupling parameter ($\lambda = 1$) is reached.

Equations (IV.20) and (IV.21) are both general equations so one has freedom in selecting the coupling parameter. For the following simulations, the interfacial area plays the role of the external Hamiltonian ($\lambda\delta H$). My goal is to explore the free energy difference as a function of interfacial area change of this system. We will relate this to the surface free energy determined from the Irving-Kirkwood (IK1) stress tensor approach. Since we calculated the surface tension earlier with confidence (see Chapter 3), the same type of system will be used to attempt to validate the free energy-work relationship.

IV.3 MODEL AND SIMULATION PROPERTIES

The simulated system consists of fully immiscible Lennard-Jones fluids and are performed on a parallelpiped of volume $L_x \times L_y \times L_z$ with $L_x = L_y$ and $L_z \geq 2L_x$. The volume contains two slabs of immiscible liquids, one of N_1 particles and the other of N_2 particles (where the subscripts *1* and *2* denote the system components or species). As stated above, the computational efficiency is affected by the rate at which the system's coupling parameter is switched. A large system (one having a large number of particles or many degrees of freedom) requires more sampling of the tails of the probability distribution because the statistical sample used to evaluate IV.15 will be dominated by infrequent or rare events. In order to ensure this sampling problem did not occur, I elected to use a smaller system than the one used in Chapter 3. Another consideration is if the system or the interfacial area is too small, the energy change associated with the area change is smaller than the energy fluctuations; there will again be a sampling problem because the system will have to be observed for an extremely long time. An intermediate system should therefore provide a good test of the Jarzynski relationship for immiscible binary fluids. Here, we take $N_1 = N_2 = 512$ so that $N = N_1 + N_2 = 1024$ in this case; however, I will show that this selection introduced another size effect, namely interfacial interaction, for this type of system. The system is subjected to periodic boundary conditions (pbc) in the x, y, and z directions. Due to these conditions, two planar interfaces of area L_x^2 are created during equilibration. We consider the z direction to be perpendicular to the interfacial regions in the following figures. The particles interact via the modified L-J potentials

$$U_{11} = 4\epsilon\left[\left(\frac{\sigma}{r}\right)^{12} - \left(\frac{\sigma}{r}\right)^{6}\right] \tag{IV.24}$$

$$U_{22} = 2V_{11} \tag{IV.25}$$

$$U_{12} = 4\epsilon\left[\left(\frac{1.2\sigma}{r}\right)^{12}\right] \tag{IV.26}$$

where ϵ and σ are the well depth and interaction range parameter, respectively (see Figure 4.1). The potential was truncated at 4σ as in Chapter 3. An assessment of the truncation artifacts was provided in the previous chapter so I will not discuss them here, though recall that a sharp interface will amplify these artifacts. The unlike-species interaction was chosen to ensure the system did not mix ($\alpha = 0$). The particles were initially distributed with a sharp interface parallel to the z-direction (see Fig. 4.2). During the equilibration phase of the simulation, the microcanonical (NVE) ensemble was used. Using the microcanonical ensemble simply decreases the system's equilibration time. We define m as the particle mass, and for simplicity, the masses are set equal to unity. Though the microcanonical ensemble is the simplest ensemble to simulate, there are problems replicating the setup experimentally. The canonical ensemble is more suitable for experimental validation. Once equilibration was achieved (see Figures 4.3 and 4.4), the canonical (NVT) ensemble was used for data collection. A Nosé-Hoover chain method developed by Martyna et. al.(13) has been used to

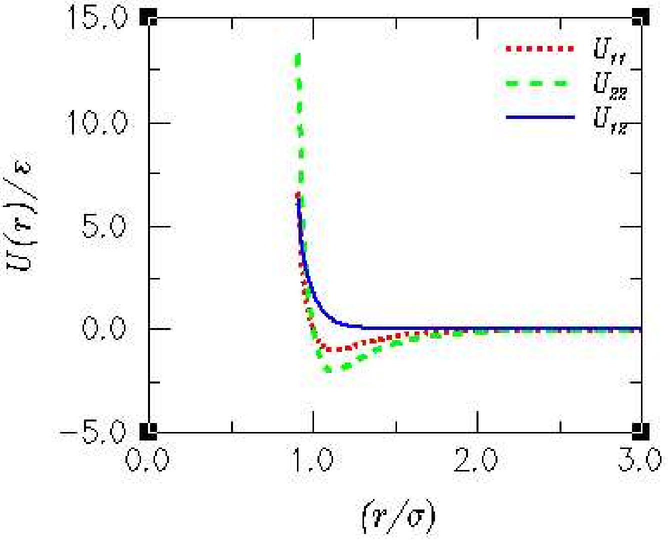

Figure 4.1: L-J potential functions for like and unlike species with α=0. The repulsive potential associated with the unlike interaction is reduced by a factor of 20.

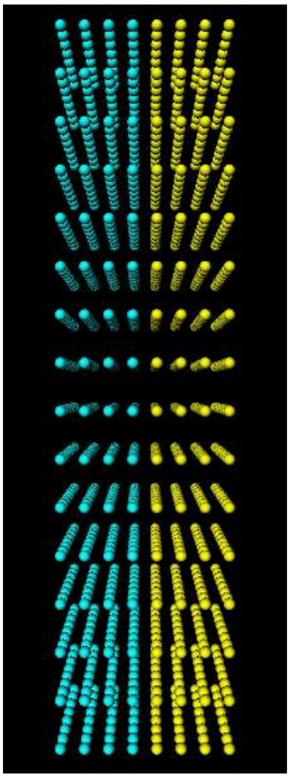

Figure 4.2: Initial configuration of the $N = 1024$ system. This distribution has a sharp interface parallel to the z-direction.

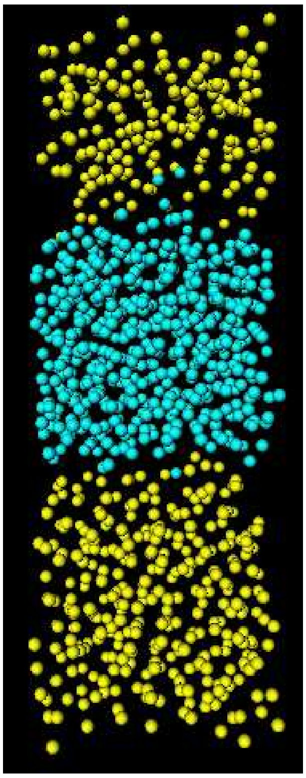

Figure 4.3: Equilibrium configuration of $N = 1024$ system. The interfacial area is A_0 in this case.

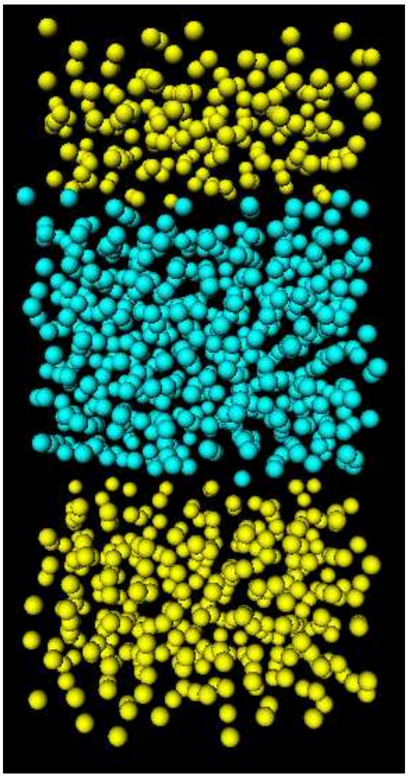

Figure 4.4: Final configuration of $N = 1024$ system. The interfacial area is $2A_0$ in this case.

control the temperature of the system. This thermostat uses a Verlet-like algorithm and has been shown to sample the canonical ensemble. This method has also been found to prevent large periodic oscillations in more complex simulations and maintains ergodicity.(64) The box dimensions initially were $L_x = L_y = 6.704\sigma$ and $L_z = 32.0\sigma$ so the system bulk densities (0.713) are lower than the triple point density for argon (0.85). Using reduced units, we are also able to introduce the following reduced thermodynamic quantities: $T^* = \frac{k_B T}{\epsilon}$ for temperature,$\gamma^* = \frac{\gamma\sigma^2}{\epsilon}$ for surface tension, and $\rho^* = \rho\sigma^3$ for density, with $\rho = \frac{N}{V}$. A Verlet like algorithm is used to integrate the equations of motion with an integration time step of $\triangle$t = .005, which corresponds to ten femtoseconds using the argon scale. The neighbor table was used as a time saving device in these simulations.(18)

The process by which the interfacial area was changed is a sequence of homogeneous dilations which consists of the following steps. Once the system had been equilibrated, a set of initial configurations were selected. The equilibrium requirements are that the total energy is stable, with small fluctuations compared to the average energy, and that the density profiles are stationary in time. I allowed the system to evolve for a short time (about a picosecond) so as to ensure stability before initiating the switching process. The simulation was then stopped and the interfacial area was increased by 10%. In order to facilitate the relaxation process and prevent particle overlap, the particle positions were shifted so as to conserve the overall volume. This amounts to a slight displacement of atoms in the x and y directions and a small volume-conserving compensating displacement in the z direction. Since no work is done on a homogeneous liquid by changing its shape, a particle reconfiguration of this type, i.e. a volume conserving virtual displacement, should have a modest effect on the total energy of the system.(65) The system was then allowed to relax until the next switch was made. The time span over which the system was allowed to relax between switches defines the switching rate. After the last switch was made, the system was allowed to run for a few picoseconds in order to ensure that a stationary state was achieved. More explicitly, the switching process consisted of a sequence of 9 homogeneous dilatations, each followed by relaxations consisting of t$'$ = 10, 100, or 500 time steps. Following the 10th dilatation, the system was allowed to evolve for 2000 time steps in order to insure that a stationary state was established. For each t$'$, we did 200 repetitions (200 transitions) from an arbitrary

Table 4.1: Irving Kirkwood calculations of the free energy (F_{IK1i}) and the isotropic or scalar pressure (P_i) for the initial state or when interfacial area is A_0. The statistical error of these calculations is also shown.

T_{ref}	F_{IK1i}	P_i
1.5	.84±.11	1.77±.18
3.0	1.19±.20	7.40±.23
7.0	1.7±.30	20.2±.40

equilibrium configuration.

IV.4 SIMULATION RESULTS

The initial configurations or states were in thermodynamic equilibrium and the Irving-Kirkwood method was used to calculate the surface tension. We can relate this quantity to the free energy used to create an interfacial area A_0, and I will refer to this value simply as the free energy from here. These values are included in Table 4.1. The behavior of these quantities relative to the system temperature is consistent with the study in the previous chapter.

The free energy was evaluated again at the end of each sequence of switching transitions and the results are shown in Table 4.2. This table also shows that the free energy does not depend on the switching rate. Note that the free energy and scalar pressure do show a

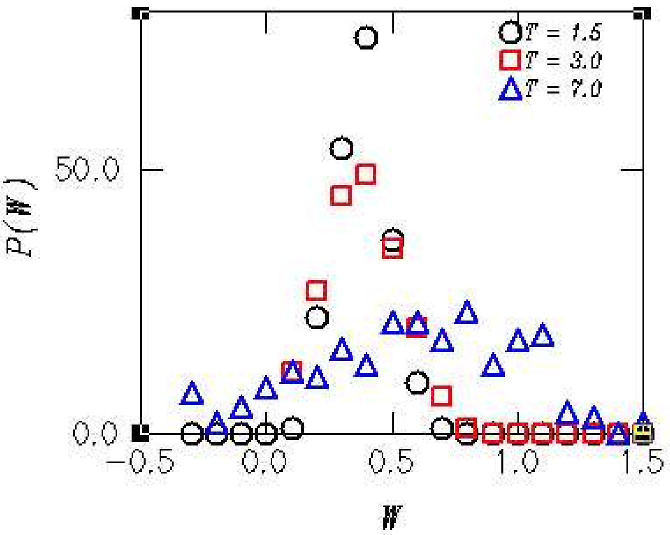

Figure 4.5: Work probability distribution. Switching rate in this case is in 100 step increments.

temperature dependence; however, upon further inspection the free energy values are quite different for initial and final interfacial areas (Compare Table 4.1 and Table 4.2). Note that this binary fluid system has two degrees of freedon, V and T, and since these are held fixed throughout the switching process, one might assume that the scalar pressure should be invariant with respect to switching; provided that both initial and final states are true equilibrium states. However, the existence of a pair of interfaces in each unit cell implies that the thermodynamic reasoning appropriate for homogeneous, isotropic systems may not be applicable in this case. For instance, the distance between the interfaces decreases as the surface area increases, and any interactions between these will impart a surface area dependence to the interfacial density profiles as well as the free energy calculations associated with them provided the final state of the system is in equilibrium.

Consider for a moment that the system has not reached equilibrium due to the length of time that the system was allowed to settle after the final interfacial switch. If this is the case, by allowing the system to evolve for a few more picoseconds (few thousand time steps), the system should come to thermodynamic equilibrium and the Irving-Kirkwood procedure would result in free energies that are independent of surface area. Even after running the system on the time scale of equilibration, I found the IK1 free energy, F_{IK1}, calculation gave results consistent with those of Table 4.2 so the final state of the system appears to be in equilibrium. With the increase in the temperature, and therefore the internal pressure, there should be a tendency for particles to migrate to the interface as the system relaxes(see Figures 3.7 and 3.8). We monitored this in the previous chapter and reported this behavior. This was not what I observed here and I will discuss the implications of these features in the next section.

In order to examine the computational efficiency of the Jarzynski relationship, the free energy difference should be independent of switching rate. The probability densities shown in Figure 4.5 were constructed by the following binning process. After a number of realizations, 200 in this case, we calculated the difference in the total energy between the initial and final configurations, which corresponds to the total (reversible plus irreversible) work done on or by the system. We then divided the work axis into bins of equal width and simply counted the number of times an energy difference (W) in a certain bin was realized. The work

Table 4.2: Irving Kirkwood evaluations of the free energy (F_{IK1f}) and the isotropic or scalar pressure (P_f) at final state or when area is $2A_0$. The statistical error of these calculations are included. Note that F_{IK1} is independent of switching rate as it should be.

Switching rate	T_{ref}	F_{IK1f}	P_f
10	1.5	1.18±.02	2.78±.05
	3.0	1.46±.02	8.78±.07
	7.0	2.07±.07	21.9±.20
100	1.5	1.17±.02	2.86±.06
	3.0	1.50±.02	8.87±.09
	7.0	1.98±.06	22.1±.30
500	1.5	1.18±.02	2.85±.07
	3.0	1.46±.07	8.77±.06
	7.0	1.97±.09	22.2±.20

probability distribution shows that the switching process is Gaussian at low temperature and far from Gaussian at the highest temperature. The free energy differences shown in Table 4.2 are in good agreement and nearly independent of the switching rate which is in accord with the Jarzynski relationship.

Table 4.3 displays the relationship between irreversible work, equilibrium free enerby difference, temperature, and switching rate. Note that $\langle W \rangle$ and ΔF_J are nearly identical for a given switching rate for all three temperatures. This implies that even the fastest homogeneous deformation is very close to being reversible, even though the work distribution function does not possess a Gaussian form at the higher temperatures. The observation that ΔF_J never exceeds $\langle W \rangle$ implies that our statistical protocol is robust.

The Irving Kirkwood stress tensor method results in an apparent free energy difference and is calculated using Equation (IV.27).

$$\Delta F_{IK1} \equiv F_{IK1(f)} - F_{IK1(i)} \tag{IV.27}$$

where the subscripts f and i refer to the final and initial states, respectively. This equation tacitly assumes that the stress profiles integrated through the interfacial region are the sole causes for the free energy changes in the entire system. In particular, Equation(IV.27) does not incorporate any free energy changes associated with the bulk or homogeneous regions of the system. The free energy differences obtained from the Jarzynski relationship range from .36 to .58 and those obtained from the IK method range from .22 to .34 as shown in Table 4.4. Since we have assumed that the final state of the system had reached equilibrium, this discrepancy indicates that the interfaces are interacting with one another. The idea of “interacting interfaces” means that the interfaces’ proximity with its image causes molecular propagations in the bulk region that are not accounted for in the free energy calculation using the IK method.

Table 4.3: Free energy difference using the Jarzynski method. The nearly identical values of $\langle W \rangle$ and ΔF_J indicate that the switching process is very close to reversible for all switching rates.

Switching rate	T_{ref}	$\langle W \rangle$	$\langle exp(-\beta W) \rangle$	ΔF_J
10	1.5	.38	.77	.38
	3.0	.39	.86	.39
	7.0	.59	.92	.58
100	1.5	.37	.77	.37
	3.0	.37	.88	.36
	7.0	.53	.92	.52
500	1.5	.36	.78	.36
	3.0	.40	.87	.39
	7.0	.58	.92	.57

Table 4.4: Comparison of IK1 and Jarzynski free energy differences. ΔF_{IK} is independent of switching rate and is included in this chart for comparison.

Switching rate	T_{ref}	ΔF_J	ΔF_{IK}
10	1.5	.38	.34
	3.0	.42	.27
	7.0	.58	.31
100	1.5	.37	.33
	3.0	.36	.30
	7.0	.52	.22
500	1.5	.36	.33
	3.0	.39	.26
	7.0	.57	.22

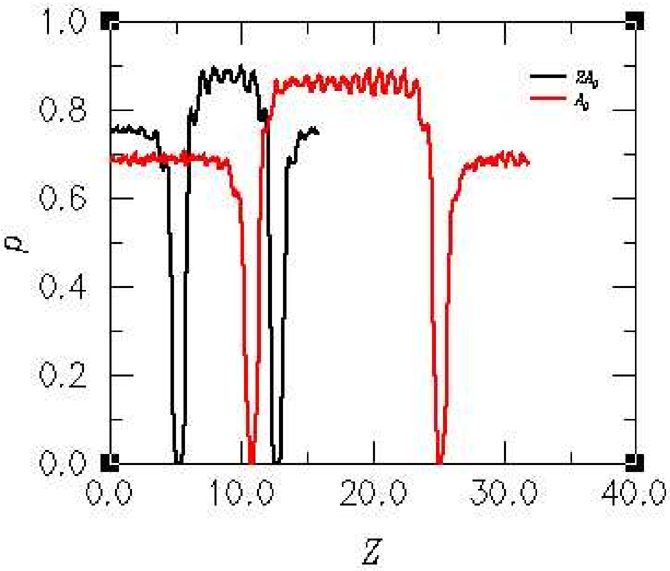

Figure 4.6: Density profile for the system when initial interfacial area A_0 and $2A_0$ for $T_{ref} = 3.0$. The two profiles are similar, but not identical. This implies that the equilibrium state of the system depends on the interfacial area.

IV.5 DISCUSSION

For the three temperatures selected, what is perhaps most striking about these simulations is that except for the lowest temperature, the free energy differences obtained by the Jarzynski method, ΔF_J, are quite a bit larger than the apparent free energy differences computed via the Irving-Kirkwood stress tensor method, ΔF_{IK1}. In order to pin down the reason(s) for this discrepancy, we sought to clarify two concerns: ensure the system was equilibrated and test for interfacial area effects on the free energy calculations. To check the first part, we equilibrated our system in both initial and final states using identical protocols. We observed that the density profiles, interfacial tensions, and other properties are nearly identical to those obtained by the various step-wise switching procedures. Moreover, we reversed a few of the switching processes to check for hysteresis effects, and found none. This strongly suggests that the systems where $N = 1024$ are indeed equilibrated after the switching process is completed. This implies that molecular propagations caused by a lack of interfacial separation might account for the difference between the IK1 and Jarzynski computations. This would be the case if, for example, the separation between interfaces were to affect the bulk density of one or both components. In order to test this hypothesis, we doubled the number of particles in our system, equilibrated at interfacial area A, computed the IK1 surface tension, and then performed the same operation at area $2A_0$. The larger system has a larger interface-interface spacing compared to a system half that size, which implies a smaller surface area dependence of the density profile as well as interfacial tension. As indicated in Figure 4.7 and Table (4.5), this is indeed what we observe: the area dependence of the interfacial tension is in fact four times smaller for the large system as compared to the small system. Also from Figure 4.6, we note that the bulk density of one of the components has clearly been increased as a result of increasing the interfacial area. This step was only done to test the aforementioned hypothesis, and recall that statistical limitations prevented the use of the 2000 particle system to compare the Jarzynski and IK1 methods.

We conclude first that both the Jarzynski and IK1 approaches can be useful tools in simulating immiscible liquid systems. The Jarzynski relation is quite effective at extracting free energy differences associated with interfacial area changes in systems comprised of closely

Table 4.5: Irving Kirkwood calculations for 2000 particle system. These quantities were calculated after system was equilibrated having interfacial area A_0 and $2A_0$. The statistical error is also shown.

Int. Area	T_{ref}	F_{IK1}	P
A_0	3.0	.83±.05	7.15±.10
$2A_0$	3.0	.90±.03	8.25±.10

spaced, interacting interfaces such as a lipid bilayer. Due to the computational cost, the Jarzynski relation is not a practical method to obtain the interfacial tension of isolated interfaces, at least for immiscible binary fluids where the IK1 method is still the best option. Secondly, we find that the homogeneous dilation, fast-switch protocol produces free energy differences that are nearly identical to those obtained by slower switching. This implies that computation costs can be greatly reduced by using a fast-switching Jarzynski method to study a strongly interacting lamellar type system. In addition, by examining the interfacial area dependent shifts of the density profiles, see Figure 4.6 and Figure 4.7, we conclude that the discrepancy between ΔF_{IK1} and ΔF_J can be attributed to the interactions between the interfaces which results in the compression of the more volatile of the two bulk phases. This effect is taken into account by ΔF_J, whereas it is implicitly excluded in the computation of ΔF_{IK1}. In other words, the change in free energy calculated by the IK1 method accounts only for the interfacial region, whereas the Jarzynski method free energy difference incorporates the bulk in addition to the interfacial properties. Presently it is not possible to separate these contributions in the Jarzynski relationship, so due to the interfacial interaction and the corresponding discrepancy between ΔF_{IK1} and ΔF_J, the free energies calculated by the

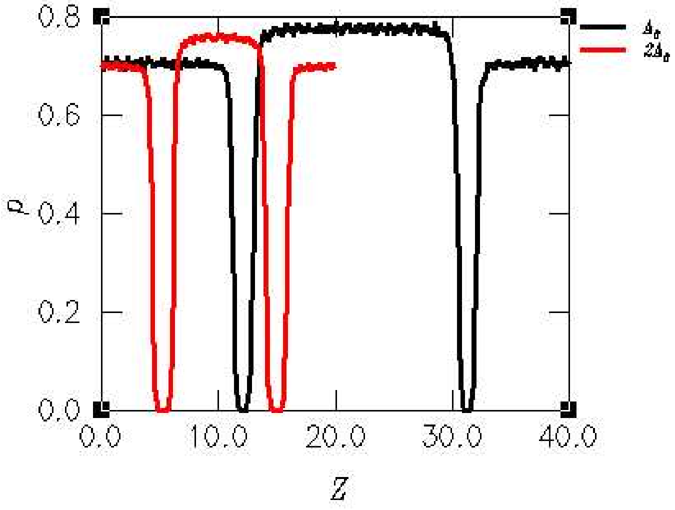

Figure 4.7: Density profile for the initial interfacial area A_0 and $2A_0$ for $T_{ref} = 3.0$. This profile is for a system of 2000 particles. The densities in this case are close to identical which implies the area dependence on the equilibrium nature of the system is small.

two methods can not be compared directly for this type of system.

V.0 MOLECULAR DYNAMICS OF ALKANETHIOL CHAINS

V.1 INTRODUCTION

We present the results of a molecular dynamics [1] study of a partialmonolayer of self assembled octadecanethiol molecules. Thecorrelations between various statistical measures of surface inducedchain ordering are examined. These include the density profile,chain morphology, tilt angle distributions, and *gauche*defect distributions. Particular attention is focussed on thesignificance of the strength of the alkane chain surface interaction,as well as the role of temperature, on the type and degree ofdisorder which we observe. The following simulations are in accord with experimental evidence which indicates that the quality, in thesense of reproducibility in the laboratory, of dense filmsincreases as the coupling of the chain molecules with the surfacedecreases. We believe that our findings have general implicationsfor the establishment of experimental protocols for selfassembled surface films of organic molecules with varying degrees ofprescribed disorder.Our simulations support that experimental observation and show that there is a range in the strength of the interaction between the methyl and methylenegroups and the surface where the character of the structure of the partially filled films changes from islands of nearly upright chainscoexisting with empty regions of the surface (the weak coupling case) toless structured regions of partially ordered chains coexisting withhighly disordered chains that completely cover the surface (thestrong coupling

---

[1] This chapter is a variant of the paper published in *Journal of Physical Chemistry B* **Vol 105**, 9503 - 9508 (2001). A preliminary study was published as a NIST Internal Report (*NIST IR 6481*).

case). The simulations also show that as the systemtemperature is increased above ambient, the structure in the intermediate couplingcase (defined below) becomes less ordered. This alsois consistent with experimental results.(66; 67; 68)

In this simulation, we consider three types of order. The first is the collectivearrangement of the molecules as indicated by the the density profile of the chains relative to the tethering surface. The second featurethat measures order is the distribution of tilt angles of the chains.The final measure of order is the fraction of *gauche* defects foundalong the chains. We shall see that the defect fraction, a quantitythat is measurable in an average sense(69; 70), correlates closely withthe density profile and tilt angle distribution. These quantitativemeasures of order are complemented by images of the chains. Theimages provide a qualitative, but informative picture of how the chainsare arrayed.

V.2 MODEL AND SIMULATION PROPERTIES

A united atom representation of a 19-site chain molecule (octadecanethiol) is used inthese simulations. Other long chain molecules such asoctadecyltriclorosilane could be considered with appropriatechanges in the head group interactions. Figure 5.1 provides anillustration of the geometrical arrangement of a chain. The intermolecular and intramolecular interactionpotentials are those of model I of Hautman and Klein(71) with the addition of harmonic stretch interactions between adjacentintramolecular sites. The details of the model are included here.The coefficients for the potential parameters are listed in Tables V.1-V.4. This model has beenshown to result in dense-packed films (number density of 4.65 moleculesper nm^2) that are consistent with the structure observed experimentally.(71) The coefficients in these potentials of course depend on the sitesinvolved. The extra indices needed to indicate the site dependencehave been supressed to simplify the notation.The intramolecular interaction consists ofstretch, bend, torsion, and Lennard-Jones terms. Explicitly,

$$U_{intramolecular} = U_2 + U_3 + U_4 + U_{L-J} \tag{V.1}$$

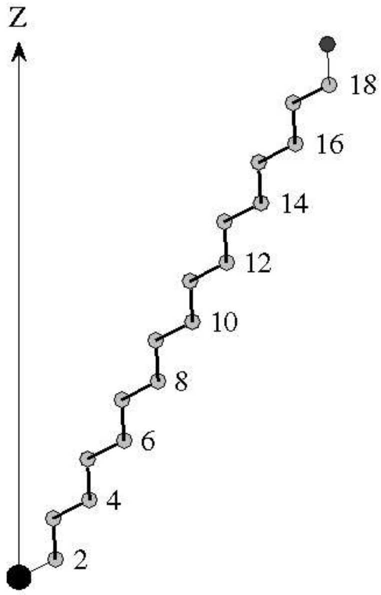

Figure 5.1: Single chain molecule containing 19 sites in an all *trans* configuration. The molecule makes an angle of $\psi = 30^\circ$ with the z-axis which is normal to the tethering surface. The large filled circle indicates the thiol group which is referred to as site number 1. The small shaded circles represent sites 2 through 18. The small filled circle indicates the terminal methyl united atom.

Table 5.1: Stretch parameters. CH_3 and CH_2 sites are equivalent for the stretch interaction.

Parameter	S-C	C-C
$k_s, 10^7 K/nm^2$	4.529	4.529
$d_0, \mathring{A}$	1.82	1.54

Table 5.2: Bend parameters.

Parameter	C-C-C	S-C-C
$k_\theta, 10^3 K/rad^2$	62.5	62.5
θ_0, deg	109.5	114.4

Table 5.3: The coefficients, C_l, in the torsional potential. Note that there is no site dependence for these coefficients.

l	a_l, K
0	1116
1	1462
2	-1578
3	-368
4	3156
5	-3788

Table 5.4: The surface interaction parameters.

Site	$C_{12}, 10^7 K\mathring{A}^{12}$	$C_3, K\mathring{A}^3$	$z_0, \mathring{A}$
CH_3	3.41	20800	0.860
CH_2	2.80	17100	0.860
S	4.089	180600	0.269

The bond stretch term is

$$U_2 = \frac{k_S}{2} \sum_{i=1}^{N-1} (\mid \mathbf{r}_{i+1} - \mathbf{r}_i \mid - d_0)^2 \tag{V.2}$$

where d_0 is the equilibrium bond length. The sum runs over the N-1 bonds and $\mathbf{r}_i$ is the positionof the i^{th} site in the chain. The stretch parameters k_S andd_0 are listed in Table 5.1.The bend term is

$$U_3 = \frac{k_\theta}{2} \sum_{i=1}^{N-2} (\cos\theta_{i+1} - \cos\theta_0)^2 \tag{V.3}$$

where θ_{i+1} is the angle with its vertex at site $i+1$ formed by bonds connectingsites $i, i+1$ and sites $i+1, i+2$, andθ_0 is the equilibrium angle at site $i+1$. The bend parametersare listed in Table 5.2. The torsion term involves adjacent quadruples of sites with the form(72)

$$U_4 = \sum_{i=1}^{N-3} \sum_{l=0}^{5} a_l \cos^l(\phi) \tag{V.4}$$

whereϕ is the dihedral angle between the two planes formed by thefour adjacent sites. The vertices of the dihedral angles are indicatedas bold lines in Fig. 5.1. There is no site dependencefor these coefficients with values (in units of K) shown in Table 5.3. The final intramolecular interaction termis a Lennard-Jones interaction between sites separated by three ormore sites.

$$U_{L-J} = \sum_{sites} 4\epsilon \Big[\Big(\frac{\sigma}{r}\Big)^{12} - \Big(\frac{\sigma}{r}\Big)^{6} \Big] \tag{V.5}$$

The intermolecular interaction is the same Lennard-Jones interactionused in U_{L-J} and acts between sites on different molecules.The Lennard-Jones potential parameters are listed in Table 5.5. There is also a surface interaction of the form.

$$U_{surface} = \frac{C_{12}}{(z - z_0)^{12}} - \frac{\alpha C_3}{(z - z_0)^3} \tag{V.6}$$

The interaction of the chain sites with the surface depends only onthe distance of the site above the surface. The factor α multiplying the coefficient C_3 is used to vary the attraction of the surface for the methyl and methylene groups. For the thiol group,α is always unity. The parameters for the surface potentialare listed in Table 5.4.The values of C_3 in Table 5.4 for the CH_3 and CH_2 sites are forthe strong coupling case mentioned in the introduction, that is for$\alpha = 1$. The weak coupling case has α values for the methyl and methylene sitesof $\frac{1}{10}$. We also consider scaling factorsof $\frac{1}{2}$ (intermediate coupling) and of $\frac{3}{4}$ and $\frac{7}{8}$ to examine the change from weak and intermediate coupling to strongcoupling to the surface. Our simulations involve 225 chains tethered to a smooth surface by thesurface potential. The chains are located in an L × L square planar region subject to periodic boundary conditions in the planar directions. The z-axis is normal to the smooth surface that islocated in the $z = 0$ plane. The size of the square, L, is 9.48 nmso that the average density is 2.50 molecules/nm^2, about $\frac{1}{2}$the close packed density. The simulations were started by placing the chains in a vertical orientation($\psi = 0$) at random positions with no overlaps. The thiol siteswere placed at the stable position of 0.24 nm above the $z = 0$ surface.Then the system was allowed to evolve, subject to a Nosé-Hooverthermostat(13) that maintains the temperature of thesystem at 297 K (ambient conditions). The equations of motion were integrated using theBeeman algorithm with a time step of 1 fs.(73; 74) The system was allowed to evolve until "stabilized".Here stability means that the various order parameters described below were unchanged over sequential, 100 ps duration runs. We do not imply that thermal equilibrium was obtained in each case discussed. In fact, different initial configurations lead to significant differences in themeasures of order when $\alpha = 1$.In addition to the simulations at 297 K, a second set of simulationswere performed to investigate the temperature variation of the amountof order in the system for intermediate coupling, $\alpha = \frac{1}{2}$.The details of this set of simulations are described in a separate section that follows.

Table 5.5: Lennard-Jones parameters.

Sites	$\sigma, \mathring{A}$	ϵ,K
S$_I$-S$_I$	4.25	200
$CH_3 - CH_3$	3.905	88.1
$CH_2 - CH_2$	3.905	59.1
$CH_3 - CH_2$	3.905	72.3
CH_3-S	3.723	105.4
CH_2-S	3.723	86.5

V.3 SIMULATION RESULTS

As stated before, three measures of order are considered in this long chain study. The first is the density profile. During the simulation, the number of sites located at a distancebetween z and z+dz above the surface is monitored. The resolution in$z$, dz, is 0.00316 nm. The second measure of order is the distibution oftilt angles of the chains. As indicated in Fig. V.1, the tilt angle,ψ, is taken to be the angle between the normal to the surface and thevector connecting the head group to the methyl group. The cosines ofthe tilt angles are binned with a resolution of 0.01. Finally, themean number of *gauche* defects, f_G, for each of the bonds is determined. A *gauche* defect is said to be present at a bond between twosites in a chain if the torsion angle about the bond is greater inmagnitude than 66°, the position of the maximum in the torsion potential.(72)The variation of the density profile, *n(z)*, of the chains with the change inthe strength of the surface attraction is indicated in Fig.5.2. Thedistance of the sites above the surface is z. Figs. V.2a through V.2d are for values of the coupling parameter α of $\frac{1}{10}$, $\frac{1}{2}$, $\frac{7}{8}$, and 1 respectively.

There are several features of these profiles to be noted. When thesurface coupling is weak, $\alpha = \frac{1}{10}$, the profile is quite structured. There are 19 distinct peaks in Fig. V.2a suggesting thatthe chains are in nearly identical configurations. This structure becomesless pronounced as the coupling increases. The peaks for largervalues of z, the distance above the surface, become blurred into lesspronounced features. Also, the maximum extension of the chainsdecreases. For $\alpha =\frac{1}{2}$ (and also for $\frac{3}{4}$ which is not shown as the profile is essentially that for $\frac{1}{2}$), the main effect is theblurring. The profile remains above n(z) = $\frac{1}{2}$ for z<2 nm.As α increases from $\frac{3}{4}$ to $\frac{7}{8}$, the profilestructure decreases significantly and *n(z)*> $\frac{1}{2}$ occurs only forz<1.6 nm. The further increase of α to 1, the strong couplingcase, produces an almost linear decrease in density for z>1.2 nm.The maximum height of a chain remains at about 2.2 nm as the otherstructural features become fainter.

Next we examine the distribution of tilt angles, ψ. The distributions of $\cos\psi$ are shown in Fig. 5.3 for α'sof $\frac{1}{10}$(solid line), $\frac{1}{2}$(short dashed line), $\frac{7}{8}$ (long dashed line) and 1 (long-short dashed line). The distributions for $\frac{1}{2}$ and $\frac{3}{4}$ are not very different,so the distribution for α = $\frac{3}{4}$ is not shown.The chains in the weak coupling case are tilted about 20°to the normal

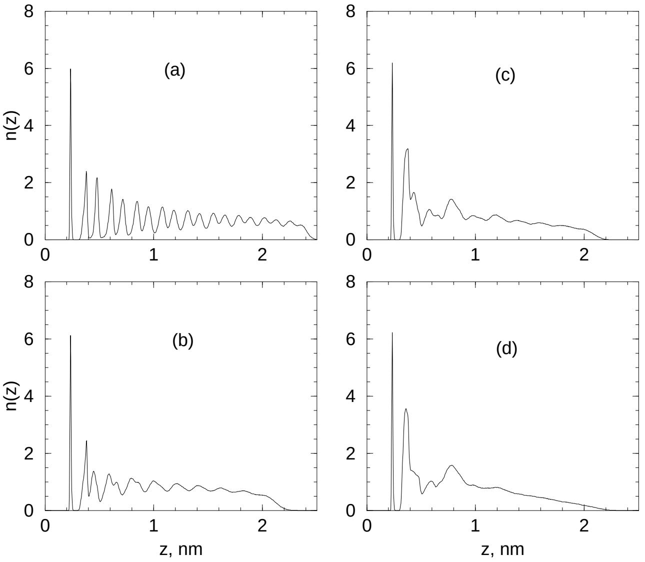

Figure 5.2: Density profiles for α=(a)$\frac{1}{10}$, (b)$\frac{1}{2}$, (c)$\frac{7}{8}$, and (d) 1. The profile for $\alpha = \frac{3}{4}$ is basically the same as for $\alpha = \frac{1}{2}$ and is not displayed.

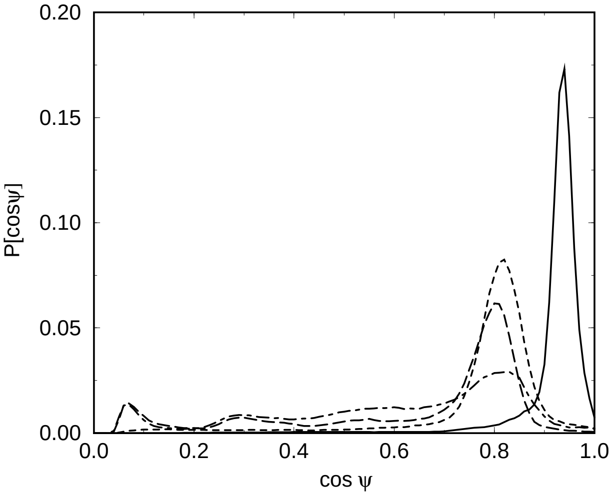

Figure 5.3: Tilt angle distribution for $\alpha = \frac{1}{10}$(solid line), $\frac{1}{2}$(dashed line), $\frac{7}{8}$(long dashed line), and 1 (long short dashed line). Again, the distribution for $\alpha = \frac{3}{4}$ is very similar to the $\alpha = \frac{1}{2}$ case and is not displayed.

with a narrow distribution of angles. As the couplingincreases to $\alpha = \frac{1}{2}$, the average tilt increases to about 35° with a broader distribution about the maximum in $P[\cos\psi]$. Further increases in the coupling to the surface lead to a significant fraction of the chains with tilt angles greater than 50°.As is the case for the density profiles, the major change in thetilt angle distributions occurs when $\alpha > \frac{3}{4}$.

The average fractions of *gauche* defects, f_G, for each site on the chains are shown in Fig. 5.4. The term *site* refers to the bondbetween two united atoms. For example, the defects on site 2.5 areassociated with the bond between united atoms 2 and 3 as shown in Fig. 5.1.

The weak coupling case has few defects although the fraction increasesfor the last two bonds. As the coupling increases in strength,the fraction of defects increases, particularly close to thesurface and close to the free end of the chain. As in the othertwo order measures, the difference between $\alpha = \frac{1}{2}$ and$\alpha = \frac{3}{4}$ is small. When α increases from $\frac{3}{4}$ to $\frac{7}{8}$, the major increase in defects is in the bottom half of the chain. The further increase of α to 1results in an overall increase in defects over the entire lengthof the chain.The format of the snapshots displayed in Figs. V.9 through V.12 is describedin the simulation results section. Snapshots are not a substitute for thequantitative order measures. We monitored the order measuresdescribed in the results section during the sequence of runs described below.The snapshots and our description of the state of the system areconsistent with the order measures. The snapshots are used only toillustrate the trends in the order of the system.The surface coupling was reduced by setting $\alpha = \frac{1}{2}$ and the system then evolved from the configuration shown in Fig. V.9for 180 ps. At 100 ps the system was disordered, but at 180 ps,the system had developed a cavity as a portion of the surface was uncovered.This cavity evolved into a well defined object surrounded by nearlyupright chains over the next 170 ps. The configuration at the endof this part of the simulation is shown in Fig. V.10. It is evidentfrom Fig. V.10 that the formation of the cavity precedes the development of spatial orderin the form of ordered rows of molecules. The development ofordered rows required and additional 200 ps. This evolution processgave us confidence that it was not necessary to achieve a fullystabilized system in order to infer the trends in the order of thesystem as the temperature was increased. As noted previously, a cavity is associated with ordered rows

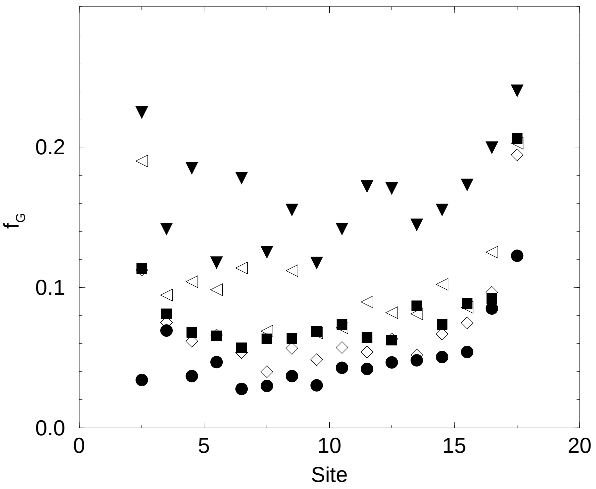

Figure 5.4: The average number of *gauche* defects for each chain site. The filled circles are the weak coupling case ($\alpha = \frac{1}{10}$), the filled squares for $\frac{1}{2}$, open diamonds for $\frac{3}{4}$, open triangles for $\frac{7}{8}$. The filled triangles are for the strong coupling case, α=1.

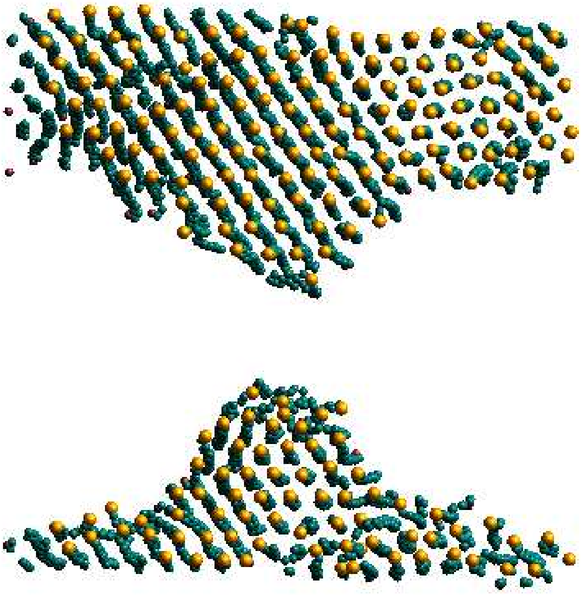

Figure 5.5: A snapshot of the chains with $\alpha = \frac{1}{10}$. This view shows that most of the chains are in nearly an upright position with local spatial order as well as indicated by the rows of chains. Periodic Boundary conditions mean the island of chains and the cavity are on the order of the box size.

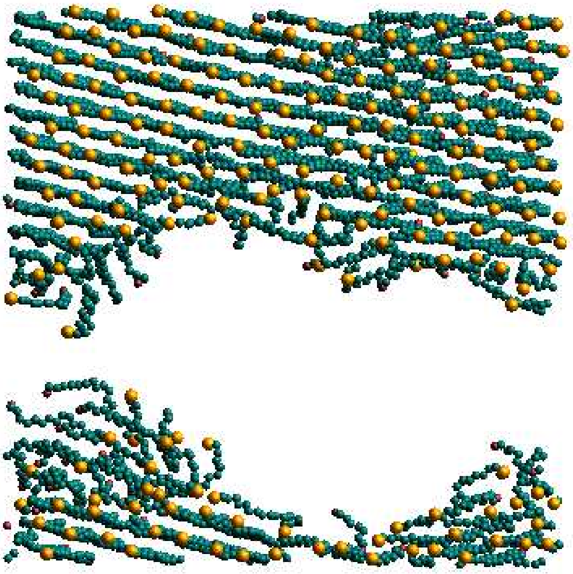

Figure 5.6: A snapshot of the chains when $\alpha = \frac{1}{2}$ which shows that the disordered chains are located mostly along the interface between the island and the cavity. Here the chain tilt is more evident than the case in Figure 5.5.

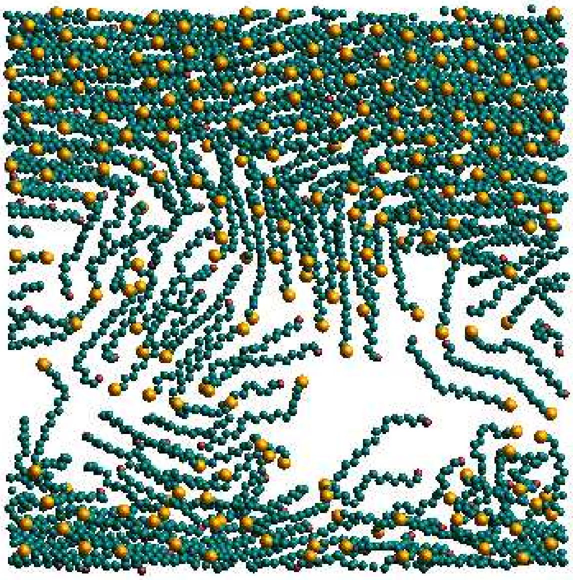

Figure 5.7: A snapshot view of the chains with $\alpha = \frac{7}{8}$ which shows that the chains have nearly filled the cavity.

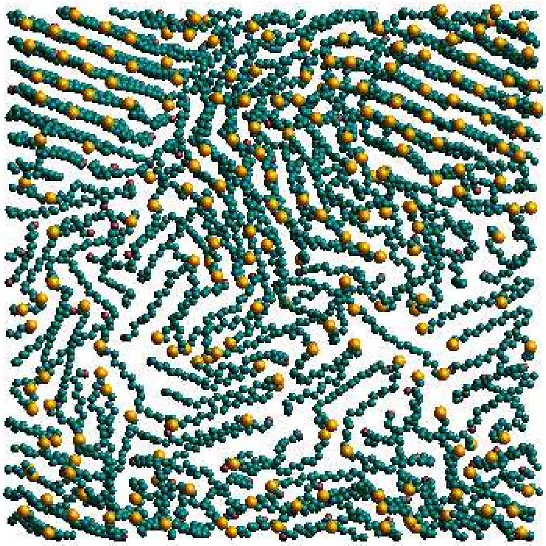

Figure 5.8: A snapshot view of the chains with $\alpha = 1$ which shows the ordered regions are smaller than the simulation cell

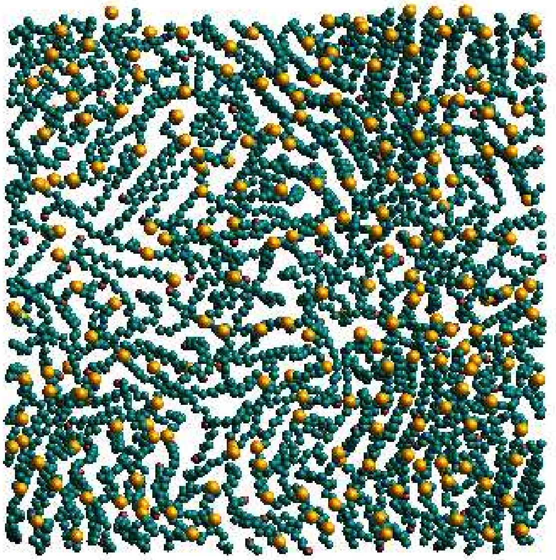

Figure 5.9: A snapshot view of the chains with $\alpha = 1$, just before the surface coupling was changed.

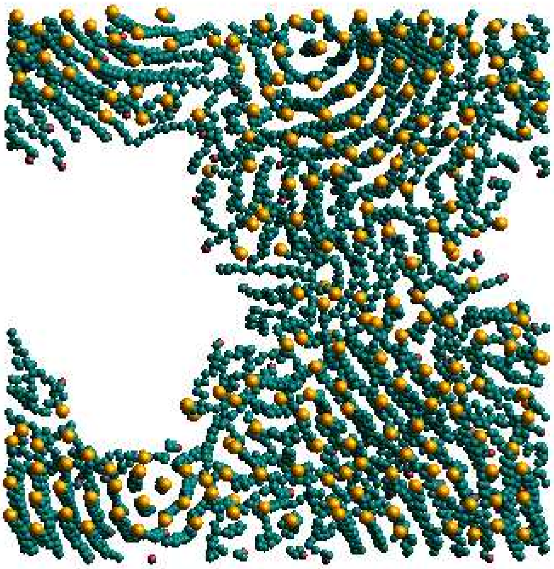

Figure 5.10: A chain snapshot when $\alpha = \frac{1}{2}$ after 350 ps. Here, a well defined cavity has formed, but the spacial ordering of the chains is not well developed.

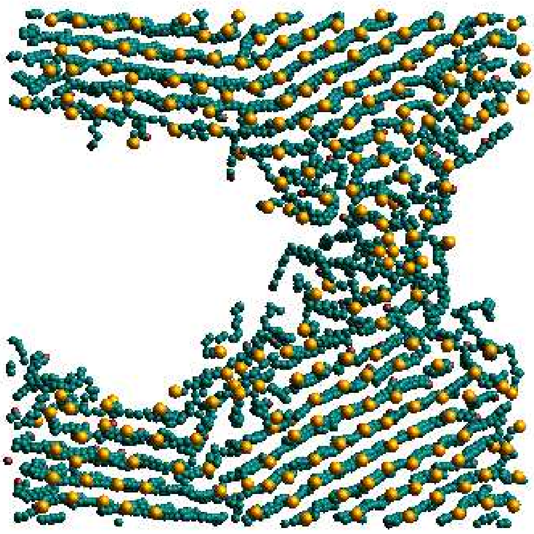

Figure 5.11: A snapshot view of the chains for T = 329 K after 220 ps. The chains have now formed well defined rows.

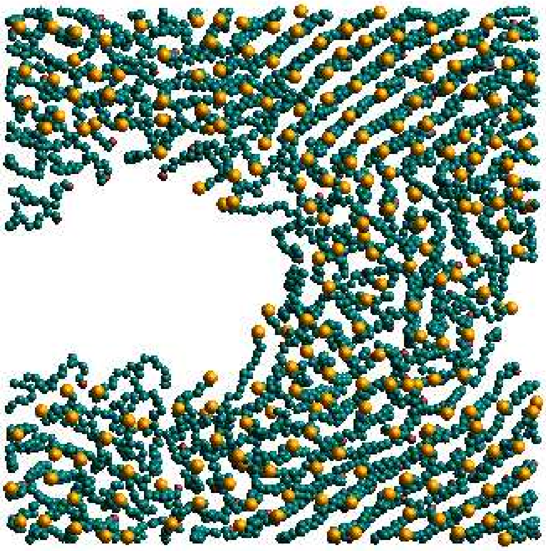

Figure 5.12: A snapshot view of the chains for T = 360 K after 220 ps. The size of the cavity has decreased, the edge of the cavity is less sharp, and the spatial extent of the ordered rows is reduced from Figure (5.11).

of chains in thestabilized system. The presence or absence of a cavity is anindicator of how the system will evolve.The temperature of the system shown in Fig. V.10was then increased to 329 K and run for300 ps. The cavity remained well defined and the spatial orderingof the chains increased with the formation of well defined rowsof chains. This is shown in Fig. V.11. For this slightly higherdensity system (2.87 molecules/nm^2), the cavity appears to beembedded in the chains rather than coexisting with an island.Next, the temperature was increased to 360 K and run for 220 ps. The cavity decreasedslightly in size as the “edge” of the cavity became more irregular. Then thetemperature was increased to 391 K and run for 320 ps. Thesize of the cavity decreased during this interval, as is shown inFig. V.12. Also, the spatial extent of well defined rows has decreased.Finally the temperature was increased to 422 K. During the next 100 ps, the cavitybecame smaller and considerable disorder was evident. After another85 ps, the cavity disappeared as the surface was completely covered by the chains, quite similar in appearance to Fig. V.9.While there are some moderately long simulations in this set, no attempt was made to demonstratestability of the states as was done in the previous set of simulations.

V.4 DISCUSSION

The types of order that develop in tethered chain molecules when thecoverage is on the order of $\frac{1}{2}$ of the close packed coveragehave been examined in terms of the strength of the attraction between the tethering surface and the methyl and methylene groups of the chains.In the weak coupling case, $\alpha = \frac{1}{10}$, the chains formordered islands of nearly upright chains coexisting with regions ofthe surface that contain no chains (a cavity). The distribution oftilt angles is narrowly peaked about 20° and the densityprofile is highly structured. The snapshot of this case suggests thatthe island consists of ordered rows of nearly upright chainsarranged in an approximately hexagonal arrangement. Consistent withthis view is relatively low fraction of *gauche* defects overmost of the chain sites. The fraction increases to about $\frac{1}{10}$near the methyl end group.On the other hand, for the strong coupling case, $\alpha = 1$, thechains form small islands or ordered regions coexisting with disorderedchains that completely cover the tethering surface. The distributionof tilt angles is broad and there are a significant fraction of *gauche* defects over all sites in the chains. The density profile is correspondingly less structured and decreases in magnitude as the height above the surface exceeds 1.2 nm.The case of intermediate coupling, $\frac{1}{2} \leq \alpha \leq \frac{3}{4}$, moderatesthe order of the weak coupling case by increasing the mean tilt angleto about 35°. The island of chains remains in coexistence withthe cavity.In the narrow range of coupling, $\frac{3}{4} < \alpha \leq \frac{7}{8}$, the arrangementof the chains changes. The rows of ordered chains are not as extensive and the cavity begins to fill in with chains that arestrongly tilted.It is not possible to say if this change in ordering is a phase transitionon the basis of the results obtained here. The temperature variationstudy does indicate that for intermediate coupling, the orderedcoexistence of upright chains and a cavity is the stable arrangement,for temperatures from ambient to 360 K. At higher temperatures, thesystem reverts to a disordered arrangement with no cavity and noclear ordering of rows of chains.

Our simulation of sub-monolayer alkanethiol films are consistentwith experimental findings. In particular, we find thatthe degree of order in the films correlates with the strength of the surface interaction and that increasing temperature promotes chain disorder. In addition,we find that several detailed statistical measures of surface filmorder that are not directly experimentally observable correlatenicely with more readily accessible averaged properties. These include density profiles, domain morphology, tilt angle distributions,and *gauche* defect distributions.

These results help one understand the experimental finding that weaksurface coupling promotes reproducibility of laboratory films.(75) With weak coupling, the tendency of thechains to form ordered islands leaves room for the addition ofchains with minimal rearrangement of already presentmolecules. With strong coupling, it becomes necessary to move oneor more already attached molecules so that the thiol group of anadded molecule can reach the equilibrium point 0.24 nm above thesurface. Clearly, the growth of well ordered films will be easierwhen the surface coupling is weak. Insofar as our simulations employ generic interaction potentials, we believe that our findings have general implications for theestablishment of experimental protocols for self assembled surface films of organic molecules with varying degrees of prescribed disorder.

VI.0 AN MD SIMULATION OF POLYETHYLENE OXIDE

VI.1 INTRODUCTION

In this chapter, a Molecular Dynamics study of surface-tethered $S(CH_2CH_2O)_6CH_3$ is presented. In this study, we analyze helix formation and thermal disorder and present the results of a simulation of surface-tethered 1-thiahexa(ethylene oxide)chains terminated by methyl groups, i.e., $S(EO)_6CH_3$, where $EO = -CH_2CH_2O-$. We find that spontaneous helix formation and details of helix morphology depend on charge partitioning ascribed to oxygen and the metheylene groups. The effects of varying surface coverage as well as chain-surface interaction strength indicate that a set of approximately $\frac{7}{2}$ helical structures oriented predominantly normal to the surface at near full coverage. This occurred even though thermal disorder clearly precludes a description based on the concept of a perfect crystalline monolayer. Thermal fluctuations in chain morphology in the vicinity of the terminal methyl groups lead to the exposure of oxygen to the external environment. We also find that the persistence of compact helix-containing domains at partial surface coverage results in the formation of well-defined cavities or void regions that expose the bare surface, even in the presence of srong chain-surface attractive interactions.We qualitatively explore and quantify structural features of self-assembled monolayers of surface tethered polyethylene oxide (PEO) chains. The detailed morphology of composite, surface-grafted, PEO-containing monolayers is currently believed to play an important role in conferring resistance of the surface to non-specific protein adsorption.(76; 77; 78; 79; 80; 81; 82; 83; 84; 85; 86; 87) While these systems have been the subject of a number of intensive experimental and theoretical investigations, there remain unresolved issues that may be at least partially addressed by the judicious use of MD. For example, the dependence of chain ordering on atomic and surface interaction potentials can be studied in the presence of statistical and thermal fluctuations. Microscopic structural features, not readily accessible to experimental probes, can then be examined under a variety of physical conditions. In particular, we investigate the helical structures formed from a monolayer of $S(EO)_6CH_3$.There exists infrared spectroscopic evidence that this monolayer consists of $\frac{7}{2}$ helices oriented normal to the (gold) tethering surface(82; 87), and so we attempt to construct a "minimal model" interaction potential, based on a model for *amorphous* polyethylene oxide, which results in a good approximation to this particular morphology. Our simulation indicates that we are reasonably successful if the nearest neighbor O-O separation distance is chosen as the principal criterion of a $\frac{7}{2}$-like helical order. The model employed in the simulation is described in the following section. The next section also contains a description of the simulations and introduces various measures used to characterize structure of the monolayers.

VI.2 MODEL AND SIMULATION PROPERTIES

A united atom representation of a 20-site $S(EO)_6CH_3$ molecule is employed in the following simulation (see Figure 6.1). From a dynamical point of view this united atom simplification is justified because the first vibrational level for C-H stretch lies far in energy above that associated with the temperature(290K) of these simulations. From a structural point of view, the asphericity of the methylene and methyl groups at short range and the modest degree of C-H charge separation are not expected to play major roles in overall chain morphology. The intra- and intermolecular parameters in this study are identical, unless otherwise noted, to those used by Lin et.al.(88) in their MD simulation of amorphous, polydisperse polyethylene oxide, except that S in our model is generally treated as distinct from O. The total potential energy of the system,U, consists of the sum of a bonded term, a non-bonded term, and a surface interaction:

$$U = U_b + U_{nb} + U_{sur} \tag{VI.1}$$

$$U_b = \sum \frac{1}{2}K_r(\triangle r_i)^2 + \frac{1}{2}K_\theta(\triangle\theta_i)^2 + \frac{1}{2}U_2\Big(1-\cos 2\phi_i\Big) + \frac{1}{2}U_3\Big(1+\cos 3\phi_i\Big) \qquad \text{(VI.2)}$$

Here $r = (r - r_D)$, where D stands for the SC, CC, and CO equilibrium bond separations, and $(\triangle\theta) = (\theta - \theta_E)$, where E is the SCC, CCO, and COC equilibrium bend angles. ϕ is a torsion angle; ie., the dihedral angle between the two planes formed by four adjacent sites associated with the quadruples SCCO, CCOC, and OCCO. The parameters for stretch, bend, and torsion are given in Table 6.1. For bonded interactions CH_2 is assumed to be identical to CH_3.

Table 6.2: Lennard-Jones Parameter[a] and Charge Partitioning[b].

Sites	ϵ,Kcal/mol	$\sigma, \mathring{A}$
S-S	0.3971	4.582
$CH_2 - CH_2$	0.1201	3.425
$CH_3 - CH_3$	0.1501	4.038
O-O	0.0950	2.851
q(0)=-0.326$\|e\|$		
q(CH_2)=0.163$\|e\|$		

[a] Unlike site interaction parameters for ϵ are determined from the geometric mean of like site parameters($\epsilon_{ij} = (\epsilon_i\epsilon_j)^{\frac{1}{2}}$).Unlike site interaction parameters for σ are determined from the arithmetic mean mean of like site parameters ($\sigma_{ij} = \frac{1}{2}(\sigma_i + \sigma_j)$).

[b] q has units of the elementary charge.

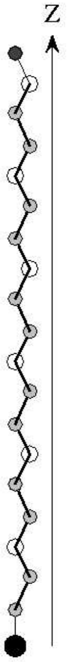

Figure 6.1: Single surface-tethered $S(EO)_6CH_3$ molecule consisting of 20 sites in an all trans configuration, with the $S - CH_3$ vector oriented normal to the surface. The large filled circle represents the thiol head group, the small filled circles represent the 12 atom methylene units, the 6 oxygen atoms appear as large empty circles, and the united atom terminal methyl group is represented by a small filled circle.

Table 6.1: Stretch, Bend, and Torsion Parameters

Stretch	S-C	C-C	O-C
K_r, Kcal/mol/$\mathring{A}^2$	590	590	672
$r_o, \mathring{A}$	1.538	1.538	1.423

Bend	S-C-C	C-C-O	C-O-C
K_θ,Kcal/mol/rad^2	125	125	112
θ_o	114.0	109.0	111.9

Torsion	S-C-C-O	C-C-O-C	O-C-C-O
U_2,Kcal/mol	-0.503	0	-0.503
U_3,Kcal/mol	2.878	2.878	2.878

Table 6.3: Parameters for the Surface Interactions

Sites	A,Kcal/mol*$\AA^{12}$	B[a],Kcal/mol*$\AA^3$	$z_o, \AA$
S	67 660	358.6	0.269
CH_2	55 600	3.396	0.860
CH_3	62 350	4.130	0.860
O	63 150	4.167	0.860

[a] The weak surface interaction case is obtained by dividing B by 10 for $CH_2, CH_3, andO$.

The first non-bonded contribution to the potential energy is a Lennard-Jones interaction which acts between sites on the same molecule which are separated by three or more sites, as well as between a given site and those sites associated with all other molecules in the system. In this case CH_2 is distinct from CH_3. The second term is a direct electrostatic interaction between all pairs of partially charged sites in the system. This charge partitioning is assumed to occur only between the oxygen and methylene units (18 charged sites per molecule). We employ the same charge assignment as proposed for amorphous polyethylene oxide, which was determined from experimental data on the dipole moment and equilibrium configuration of the dimethyl ether molecule. The Lennard-Jones parameters and partial charge assignments are given in Table 6.2. The non-bonded contribution to U, U_{nb}, takes the form

$$U_{nb} = U_{LJ} + U_q \tag{VI.3}$$

$$U_{LJ} = \sum_{sites} \left[\left(\frac{\sigma}{r}\right)^{12} - \left(\frac{\sigma}{r}\right)^{6} \right] \tag{VI.4}$$

$$U_q = \sum_{sites} \frac{q_i q_j}{\mid r_i - r_j \mid} \tag{VI.5}$$

All non-bonded interactions are assumed to terminate at a distance of 1.2 nm; long range dispersion interactions and electrostatic effects are not included in our model.Finally, the surface interaction term takes the form(71)

$$U_{sur} = \frac{A}{(z - z_0)^{12}} - \frac{B}{(z - z_0)^3} \tag{VI.6}$$

The strong repulsion at short distances ensures an impenetrable surface, whereas the attractive portion serves to firmly tether S while influencing the overall structure of the chains. The surface interaction parameters are given in Table 6.3. Note that the B parameter for S is larger by a factor of ≈ 100 compared to B for the other groups. In summary, our interaction potential is based on a model for amorphous polyethylene oxide, supplemented by a chain-surface interaction and strong S-surface tethering.Our simulations cell contains 225 $S(EO)_6CH_3$ molecules tethered via a strong short range S-surface interaction. The overall chain-surface potential is translation-invariant with respect to directions parallel to the surface, so that lateral motion is inhibited only by the presence of nearby molecules. The chains are located in an L × L square planar region subject to periodic boundary conditions in the lateral direction. The z-axis is chosen normal to the surface which is located in the $z = 0$ plane. The cell dimension, L, is adjusted so that the surface area available per chain varies by steps from that corresponding to a close-packed density of 0.214 nm^2 to twice this value.The simulations were initiated by placing the chains in a vertical orientation with respect to the tethering surface in a perfect square-planar array. The starting configuration of each chain was taken as the all-trans form as depicted in Figure 6.1. The thiol sites were set at 0.24 nm above the $z = 0$ plane, and the system was then allowed to evolve, subject to a Nosé- Hoover thermostat(13) that maintained the temperature at 290K (NVT-ensemble). The equations of motion were integrated using the Beeman algorithm(73; 74) with a time step of 1 fs to guarantee adequate resolution of the C-C and C-O stretching motions. The system was allowed to evolve until certain statistical measures of order, such as the density and orientation profiles, were invariant with respect to any further increases in simulation time, which was typically in the range of 100-200 ps. The attraction of the surface for the oxygen , methyl, and methylene groups was chosen as either weak or strong, where, in Table 6.3, where B(strong) is listed; note that B(strong) = 10 B(weak). Since the two sets of simulations yielded nearly identical results for the various averages studied, the figures refer, with one exception, to the weak field case.

VI.3 SIMULATION RESULTS

Three types of order are considered. The first is a collective atomic-level density profile of thechains relative to the tethering surface. The second measure of order is the distribution of $S-CH_3$ tilt angles relative to the surface normal. The third measure of order consists of the distribution of various O-O *intramolecular* separation distances. This function provides a succinct statistical descriptionof helix morphology at several length scales which is compared with ideal helical order. These quantitative measures of order are then supplemented by instantaneous projected images of the collection of chains that provide a qualitative but informative picture of the behavior of the entire surface array.

The number density profiles consist of plots of the number of sites located at a distance $z + dz$ above the surface vs. z with a dz resolution of .00316 nm. The orientation distributions are plots of the cosines of the tilt angle of the $S - CH_3$ with the unit vector relative to the surface normal. The cosines of these tilt angles are binned with a resolution of 0.01. The orientation distribution can be interpreted as the fractional density of chains having a prescribed projection onto the z-axis. The third measure of order, the *intramolecular* separation, is intended to quantify the notion of helicity. This consists of calculating the average nearest neighbor (NN), 2^{nd} NN, etc., set of O-O Euclidean distances (not z-projected distances) for each chain, with a dz resolution of .00316 nm, and then averaging over all molecules in the system. This has the effect of measuring average helix order relative to each individual molecular frame as opposed to a surface or lab-fixed frame.

At full coverage the chain orientation, shown in Figure 6.3, is decidedly normal to the surface with a modest though non-negligible dispersion of roughly 7°. At $\frac{3}{4}$ full coverage a secondary component is evident, located at about 75° from upright, while the maximum has shifted away from upright by about 20°. Note the factor of ≈ 3 reduction in the maximum orientation amplitude relative to the full coverage case. At $\frac{2}{3}$ full coverage the orientation distribution has become bimodal, with the maximum now shifted by $\approx$30° from the normal. Also, at $\frac{2}{3}$ full coverage the maximum amplitude has shrunk considerably relative to the previous case, the overall distribution has broadened, and the secondary component has become more prominent.

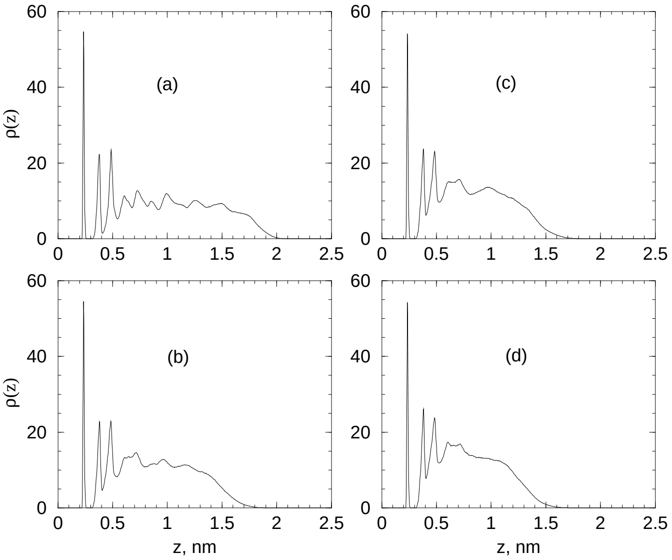

Figure 6.2: Density profiles for four degrees of surface coverage:(a) full coverage at $0.214nm^2$ projected surface area per molecule, (b)$\frac{3}{4}$ full coverage, (c)$\frac{2}{3}$ full coverage, and (d)$\frac{1}{2}$ full coverage. The chain-surface interaction is weak and since the strong surface interaction causes similar behavior, it is not displayed.

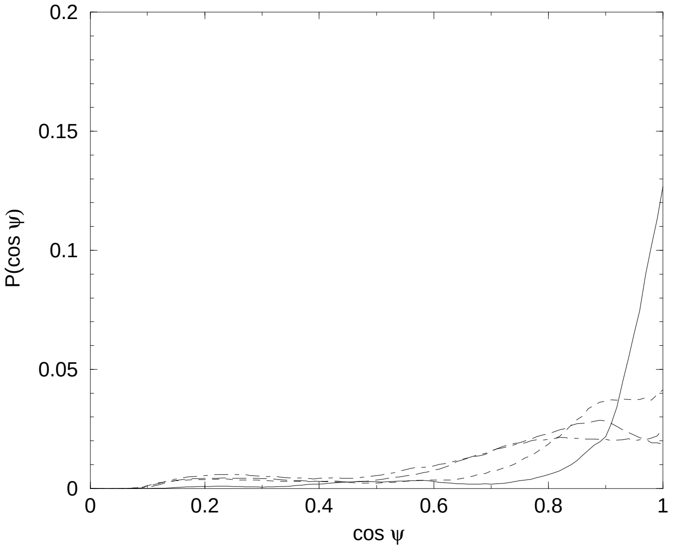

Figure 6.3: The weak surface-interaction $S-CH_3$ tilt angle distributions. They are presented as the cosine of the angle that this vector makes with the surface normal vector and are shown for full surface coverage(solid line), $\frac{3}{4}$ full coverage (dashed line), $\frac{2}{3}$ full coverage (long dashed line), and $\frac{1}{2}$ full coverage (long-short dashed line). Results for the strong surface interaction are very similar and are not displayed.

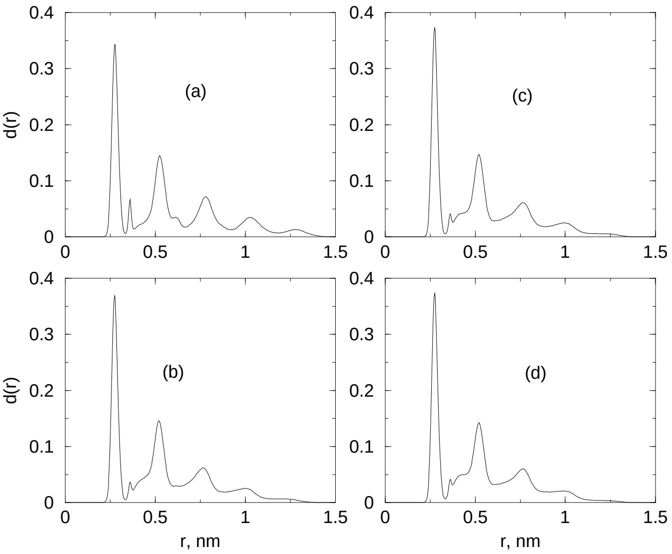

Figure 6.4: Distributions of *intramolecular* O-O separation distances for weak chain-surface interaction are shown for four degrees of surface coverage: (a)full coverage, (b)$\frac{3}{4}$ full coverage, (c)$\frac{2}{3}$ full coverage , and (d)$\frac{1}{2}$ full coverage. Similar results for the strong surface interaction are not displayed.

The distributions of NN, 2^{nd} NN, etc., intramolecular O-O separation distances are shown in Figure (6.4). At full coverage the NN O-O maximum is located at 0.277 nm. We also find a small though distinct trans-like satellite peak at 0.365 nm, a second NN O-O maximum at 0.528 nm, and a third located at around 0.79nm. An ideal $\frac{7}{2}$ helix morphology gives 0.297 nm and 0.577 nm for the NN and 2^{nd} NN O-O separations,(89; 90) which implies that the simulation result is consistent with this structure at short distances, but that discrepancies arise for larger O-O separations. Incidentally, the ratio of NN to 2^{nd} NN peak locations differs by only 2% for simulation vs.$\frac{7}{2}$ helix. At lower surface coverage, the satellite peak is less distinct whereas the NN O-O peak becomes slightly sharper. Both the z-projected density profiles and the O-O separation distance distributions vary slightly from full to $\frac{1}{2}$ full coverage, whereas the tilt angle distributions are much more sensitive to the degree of surface packing. This seems to be consistent with a picture of somewhat flexible but intact helical structures that tend to topple over at reduced coverage.

A series of snapshot views looking down on the surface-tethered array along the z-axis is presented in Figure 6.6 through Figure 6.10. The size of the connected balls forming the chains has been scaled down from what would be inferred from more realistic molecular models so as to provide contrast for the projected structure. The small dark blue spheres that represent the terminal methyl groups do not form a well-ordered hexagonal pattern; this is clearly inconsistent with the notion of a perfect lamellar crystal. Also, the prominence of some of the large yellow spheres representing oxygen indicates that these groups may be exposed to the external environment. A key feature revealed by this series of snapshots is the appearance, at close to $\frac{1}{2}$ full surface coverage, of well-defined cavities that expose the bare surface, an effect that persists even in the presence of strong chain-surface interactions. Insofar as the three measures of ordering considered here show no dramatic changes as the surface interaction is switched from weak to strong, we arrive at the picture of relatively robust domains of predominately upright helical molecules(at high surface coverage) with a considerable amount of thermal disorder.

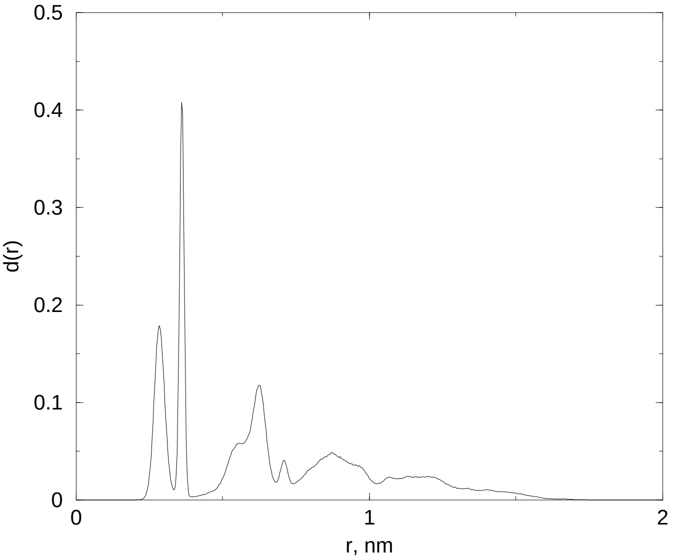

Figure 6.5: The distribution of intramolecular O-O separation distances in the absence of any electrostatic interactions is shown for the full surface coverage case

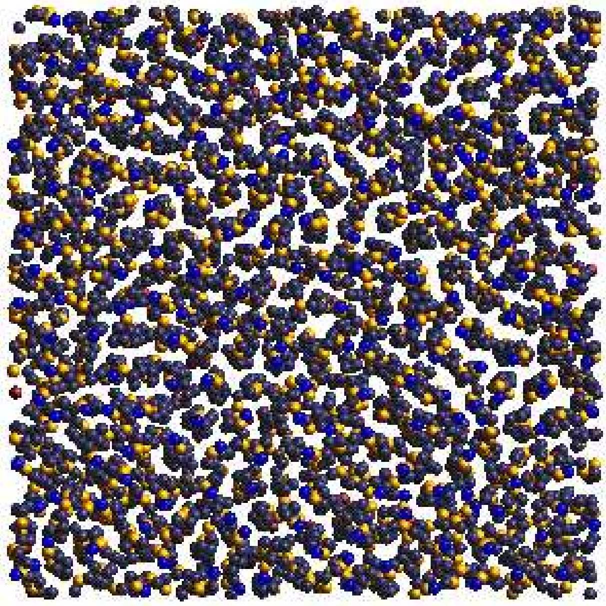

Figure 6.6: The projected snapshot view of all 225 chains as viewed from a vertical position located above the terminal methyl groups; this picture was taken at full surface coverage. The small dark blue spheres represent the terminal methyl groups, large yellow spheres are oxygen, small grey spheres are methylenes, and the small red spheres are sulfur. Even though the chains are predominately in an upright position and the lateral pattern is roughly hexagonal, there exists a considerable departure from the notion of perfect crystalline ordering which is due to thermal fluctuations.

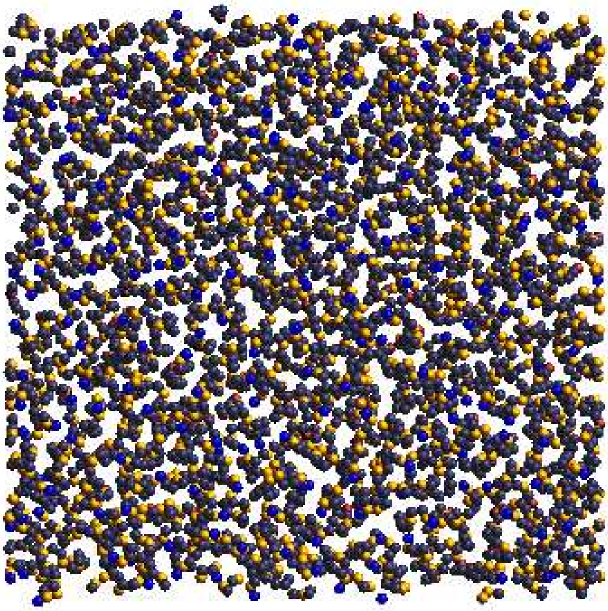

Figure 6.7: Snapshot view of the chains at $\frac{3}{4}$ full surface coverage. There is a superficial resemblance to the full coverage picture; however, a closer inspection reveals that a substantial fraction of the chains are tilted away from an upright position. This effect is clearly seen in the associated orientation distribution.

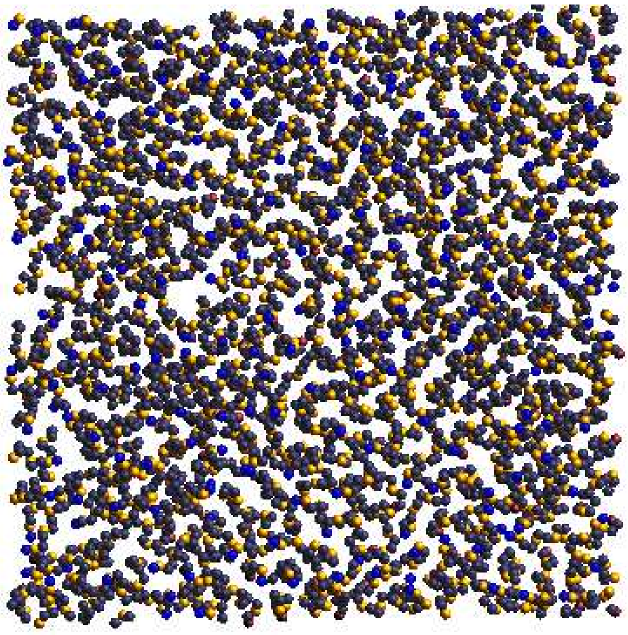

Figure 6.8: Snapshot view of the chains at $\frac{2}{3}$ full surface coverage. There is a close resemblance to both the full coverage and the $\frac{3}{4}$ full coverage cases; however, the associated orientation distribution now has a distinctly bimodal character.

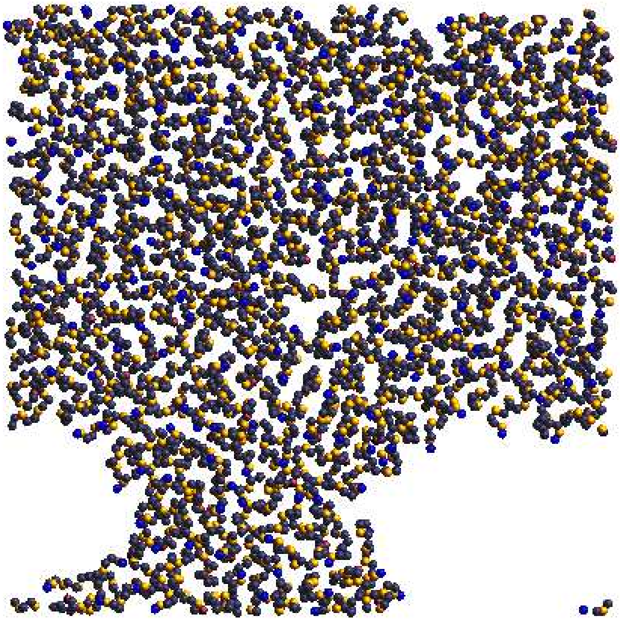

Figure 6.9: Snapshot view of the chains at $\frac{1}{2}$ full surface coverage with a weak chain-surface interaction. There is a qualitative difference between this picture and those associated with higher coverage, insofar as well-defined cavities or regions completely devoid of chains are now apparent. The associated orientation distribution still resembles that for the $\frac{2}{3}$ full coverage case. Cavities are not observed at $\frac{3}{5}$ full surface coverage, even after equilibration times of 200 ps, which suggests that they may begin to appear over a rather narrow range of surface densities.

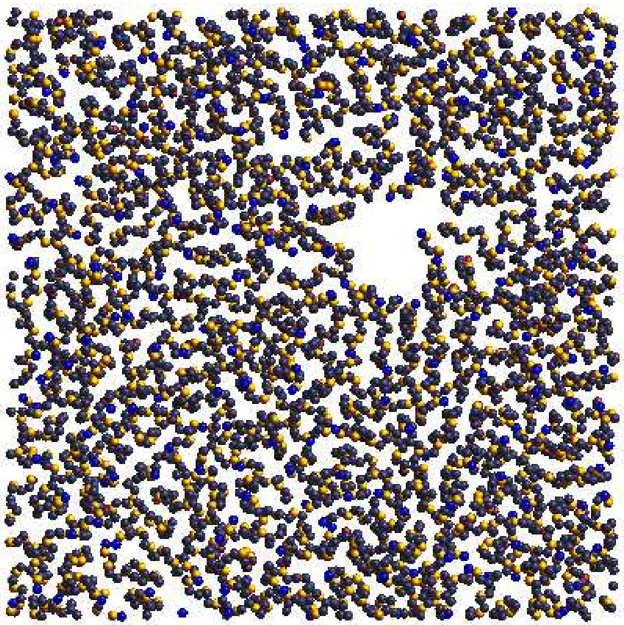

Figure 6.10: Snapshot view of the chains at 0.54 full coverage with a strong chain-surface interaction; note the appearance of a small though well-defined cavity. As in the weak surface interaction case, for the strong surface interaction case, cavities are not observed at $\frac{3}{5}$ full coverage, although large cavities are apparent at $\frac{1}{2}$ full coverage.

We have investigated the types of order that spontaneously develop in surface-tethered PEO chain molecules as the coverage is varied from close-packed to $\frac{1}{2}$ of the close-packed density, and the strength of the interaction between the tethering surface and the methylene, oxygen, and terminal methyl groups of the chains is switched from strong to weak. In contrast to a previous MD study of surface-tethered octadecanethiol molecules we find no tendency for $S(EO)_6CH_3$ to collapse onto the surface as a disordered film at reduced surface coverage and strong chain-surface attraction. (91; 92) Instead, the PEO chains remain oriented predominately normal to the surface with a structure that resembles a $\frac{7}{2}$ helix, thereby producing well-defined cavity regions which expose the bare surface along with oxygen atoms associated with domain wall chains.In addition, this study indicates that high resolution density profiles are poor indicators of average chain morphology, insofar as profile thermal broadening, associated mostly with backbone vibrational motion and bending, tends to obliterate structural features that are not located close to the tethering surface. Direct evidence for this backbone rocking is provided by the orientation distribution profiles of the $S - CH_3$ vector. In order to help clarify the situation a *helix order parameter distribution* is introduced which focusses on the density of various intramolecular O-O separations. This function provides a compact measure of helix morphology and order which varies from local separations, corresponding to nearest neighbor (NN) O-O distances, to long-range separations, which corresponds to first-last O-O distances. Whereas the nearest neighbor peak at 0.277 nm accords reasonably well with the ideal $\frac{7}{2}$ helix value of 0.297 nm, we observe significant discrepancies at larger O-O separations. In particular, we find a satellite peak at a separation of 0.365 nm which is attributed to a distinct locally extended trans-like chain morphology and which accounts for 7% of the total (NN) population. We conclude that surface-tethered $S(EO)_6CH_3$, as modeled in our simulation, does resemble a $\frac{7}{2}$ helix for short-range correlations, but that thermal fluctuations significantly disrupt long-range helical order.Another principal finding of this study is the importance of intermolecular interactions, and in particular, partial charge-based electrostatic interactions, in spontaneous helix formation and morphology. In fact, we have performed Brownian dynamics simulations on a single tethered $S(EO)_6CH_3$

chain which, under room temperature conditions, produces a disordered structure with an O-O distribution which is not in accord with what we observe in our MD simulation of 225 interacting molecules. The significance of partial charge assignments is suggested by the fact that, in the complete absence of charge separation, the O-O distance distribution shows a very prominent (NN) trans-like peak located at 0.352 nm. While an explicit representation of the methylene hydrogen atoms might be expected to have consequences for detailed helix morphology, we do not believe that this can serve as a major factor in helix formation in PEO chains. Furthermore, we found that helix morphology depends to some degree on the details of charge partitioning; in fact, excessive charge separation between oxygen and the methylenes resulted in collapse of the helix morphology into a set of compact though disordered spiral-like structures.The presence of considerable disorder in the central and terminal portions of the chains, as measured in a laboratory-fixed reference frame, is apparent from both the density profiles and $S-CH_3$ orientation distributions. Even at close packed density the combination of backbone reorientation and bond bending leads to considerable exposure to the external environment of O in the terminal methoxy group. At first this pronounced disorder might seem incompatible with the infrared transition dipole-dipole coupling theory of Kobayashi and Sakashita(93) (K-S), as these authors base their analysis on a perfect lamellar crystal structure. However, a single unit transition dipole is assumed by K-S to consist of 7 (PEO) chemical units (a unit cell), which is larger than an entire chain in our simulation. In addition, the lateral disorder associated with an imperfect hexagonal lattice, even when combined with orientation disorder in the transition dipoles, may have only a minor influence on the value of the so-called geometric factor, which consists of an orientationally weighted lattice sum and which plays a central role in the IR frequency shift predicted by K-S.

VII.0 CONCLUSION

In this dissertation, I have shown that Molecular Dynamics (MD) can provide very important insights into statistical and thermophysical properties of systems that may not be readily observable by experimental means. Since the presence of interfaces plays a fundamental role in fields ranging from biology to metallurgy, understanding these interfacial properties at the microscopic level will assist in fields as diverse as drug design and the control of surface defects in semiconductors. I have shown how MD can assist in providing a detailed understanding of interfaces at the molecular level. Chapter I provided an introduction to surfaces and surface properties. Chapter II gave a brief introduction to molecular dynamics simulations. I also discussed some of the limitations of this method and how their impact may be reduced.

In chapter III, I reported MD simulation results of two simple liquids having little affinity to mix. Since the interface breaks the symmetry of a bulk system, I had to introduce the notions of an anisotropic stress tensor and non-uniform density profiles. The simulations were used to calculate thermodynamic and interfacial properties and to infer a description of the behavior of these system quantities. Using the normal and transverse components of the pressure tensor we evaluated the surface tension and noticed an unusual increase with increasing temperature. Using basic thermodynamic arguments, I introduced a pressure induced void transfer mechanism to explain this behavior. I also provided a brief physical interpretation of the surface tension maximum. I hope to conduct further simulation studies with more complex fluids to see if they behave in a similar manner.

The next chapter provided a study to determine if a series of non-equilibrium simulations would allow one to predict the surface tension behavior of two immiscible liquids. I used the development introduced by C. Jarzynski which states that one can determine equilibrium quantities from an ensemble of non-equilibrium thermodynamic "measurements" if done under the appropriate conditions of statistical averaging. Since this is a more general method than the stress tensor approach, I simulated its compliance with the interface of two simple immiscible fluids. I found that both the Jarzynski and IK1 approaches can be useful tools in simulating immiscible liquid systems. The Jarzynski relation is quite effective at extracting free energy differences associated with interfacial area changes in systems comprised of closely spaced, interacting interfaces such as a lipid bilayer. Due to the computational cost, the Jarzynski relation is not a practical method to obtain the interfacial tension of isolated interfaces, at least for immiscible binary fluids where the IK1 method is still the best option. Secondly, we find that the homogeneous dilation, fast-switch protocol produces free energy differences that are nearly identical to those obtained by slower switching. This implies that computation costs can be greatly reduced by using a fast-switching Jarzynski method to study a strongly interacting lamellar type system. We concluded that the discrepancy between ΔF_{IK1} and ΔF_J can be attributed to the interactions between the interfaces which results in the compression of the more volatile of the two bulk phases. This effect is taken into account by ΔF_J, whereas it is implicitly excluded in the computation of ΔF_{IK1}. In other words, the change in free energy calculated by the IK1 method accounts only for the interfacial region, whereas the Jarzynski method free energy difference incorporates the bulk in addition to the interfacial properties. Presently it is not possible to separate these contributions in the Jarzynski relationship, so due to the interfacial interaction and the corresponding discrepancy between ΔF_{IK1} and ΔF_J, the free energies calculated by the two methods can not be compared directly for this type of system.

An MD study of long tethered alkane chains was presented in chapter V. We found a distinct difference in the types of order that developed when the coverage was on the order of $\frac{1}{2}$ of the close packed coverage, depending on the strength of the interaction between the surface and the methyl and methylene groups of the chain. In the weak coupling case, $\alpha = \frac{1}{10}$, the chains formed ordered islands where the chains were nearly upright and that coexisted with regions of the surface that contained no chains. This area could be viewed as a cavity. The distribution of tilt angles was narrowly peaked about 20° from vertical and the density profile was highly structured. We found that the strong coupling case was quite different. For the strong coupling case, $\alpha = 1$, the chains formed small islands or ordered regions that coexisted with disordered chains that completely covered the tethering surface. The distribution of tilt angles was broad and there seemed to be a significant fraction of *gauche* defects over all sites in the chains. The density profile was also correspondingly less structured and decreased in magnitude as the height above the surface exceeded 1.2 nm.

For the intermediate coupling case, $\frac{1}{2} \leq \alpha \leq \frac{3}{4}$, the island of chains remained in coexistence with the cavity. In the narrow range of coupling, $\frac{3}{4} < \alpha \leq \frac{7}{8}$, the chain arrangement changed, and the ordering was not as extensive. In this case, the cavity began to fill with those chains which were strongly tilted. Our simulations of sub-monolayer alkanethiol films are consistentwith experimental findings and should help understand why weak coupling results in well-ordered patterns similar to those found in the laboratory. Since the simulations we conducted employed generic interaction potentials, we believe that our findings have general implications for the establishment of experimental protocols for self assembled surface films of organic molecules with varying degrees of prescribeddisorder.In chapter VI, we used MD to investigate the types of order that spontaneously develop in surface-tethered PEO chain molecules as the coverage is varied from close-packed to $\frac{1}{2}$ of the close-packed density, and the strength of the interaction between the tethering surface and the methylene, oxygen, and terminal methyl groups of the chains is switched from strong to weak. At the lowest surface coverage we found that the PEO chains remain oriented predominately normal to the surface with a structure that resembles a $\frac{7}{2}$ helix, thereby producing well-defined cavity regions which expose the bare surface along with oxygen atoms associated with domain wall chains. In addition, our MD study indicated that high resolution density profiles are poor indicators of average chain morphology, insofar as profile thermal broadening, associated mostly with backbone librational motion and bending, tends to obliterate structural features that are not located close to the tethering surface. Another principal finding of this study was the importance of intermolecular interactions, and in particular, partial charge-based electrostatic interactions, in spontaneous helix formation and morphology. We also found that the significance of partial charge assignments is suggested by the fact that the O-O distance distribution shows a very prominent (NN) trans-like peak located at 0.352 nm when charge separation is not present. Using the density profiles and $S - CH_3$ orientation distributions, we were able to discern considerable disorder in the center and ends of the surface-tethered molecules. One conclusion of the polyethylene oxide study was that the lateral disorder associated with an imperfect hexagonal lattice, even when combined with orientation disorder in the transition dipoles, may have only a minor influence on the experimentally observed IR frequency shift associated with the $\frac{7}{2}$ helix morphology.

The overall results clearly show the importance of MD simulations in helping to refine some of the models of partial monolayers and interfaces. I have also shown how simulation combined with traditional methods may be used to develop new models, and in effect, developed novel means of describing interfaces and interfacial properties. My purpose for engaging in these studies was to show the importance of MD simulation studies and how they can be used to augment and refine the theoretical predictions of models of liquid-liquid interfaces and surface-tethered arrays of molecules.

APPENDIX A

SIMULATION CODE FOR CHAPTER III

```
      program md3a0
c     Revised 11-15-00 for surface tension, liquid-liquid interface
c     u(z), pchk added 10-23-00.  alpha part added, along with correction
c     to the integration algorithm 7nov02. incremental output has been
c     added ~oct02.  this program was parallelized to which reduced the
c     computational time by a factor of 4 on jan03.
      parameter (np=2000)
      dimension x(np),y(np),z(np),u(np),v(np),w(np),p(np)
      dimension ax(np),ay(np),az(np),axm(np),aym(np),azm(np),ap(np)
      dimension lr(400000)
      dimension ve(500,3),vf(500,3),die(500,3),dif(500,3)
      dimension g(500),icount(500),nxstart(np)
      double precision rhoz(0:400),sxx(0:400),syy(0:400),szz(0:400),
     x  pn(0:400),pt(0:400),ue(0:400)
c
c     common blocks
c
      common /cord/ x,y,z,u,v,w
      common /cacc/ ax,ay,az,axm,aym,azm
      common /ctab/ lr,icount,nxstart
      common /cvef/ ve,vf,die,dif
      common /cpar/ xmax,xmax2,ymax,ymax2,zmax,zmax2,rm1,rp1
      common /cprf/ rhoz,sxx,syy,szz,pn,pt,ue
      include 'mpif.h'
      include 'parallel.h'
      real*4 ts,te,tsset,teset,termt
      real*8 ws,we,wsset,weset,wallt

      call par_begin
      cpu_accelt = 0.
      wall_accelt = 0.
      commt = 0.
      cpuct = 0.
```

```
       cputable = 0.
       walltable = 0.
       ictable = 0
       call seconds(ts,ws)
c
c      open files
c
       open(2,file='md32')
       if (master) open(3,file='md3out')
       open(8,file='md38')
c
c      read in startup information
c
       read(2,1) j0,jmax,npart,jrest
1      format(4i10)
2      format(6f10.5)
       read(2,2) dt,ene,xmax,ymax,zmax,rm1
c
       close(2)
c      rm1 is the range of the interaction
c      rp1 is the square of the corresponding distance
c        for use in construction of the neiqhbor table.
c
c      list what has been provided
       if (master) write(3,1) j0,jmax,npart,jrest
       if (master) write(3,2) dt,ene,xmax,ymax,zmax,rm1
c
c      rework the range parameters
       rp1=(rm1+0.3)**2
           rm1=rm1**2
c
c      specify half-box size
       xmax2=0.5*xmax
       ymax2=0.5*ymax
       zmax2=0.5*zmax
c
c      generate  pi
         pi=4.*atan(1.)
         dt6=dt*dt/6.
         dtv=dt/6.
c      read in restart information
       call restart(etot,ek,jt,npart,1)
c
c      set up potential and force
         epsi=1.
         sig =1.
 palpha =0.
       call pot(epsi,sig,palpha)
c
c      scale to desired energy
       scale=1.+(ene-etot)/ek
        if(scale.lt.0.001) scale = 0.001
        scale=sqrt(scale)
        if (master) write(6,19) ene,etot,ek,scale
19      format(1x,4e13.4)
        do 22 j=1,np
          u(j)=u(j)*scale
          v(j)=v(j)*scale
```

```
          w(j)=w(j)*scale
22      continue
c
c      set initial values
          ek1=0.
          ek2=0.
          et1=0.
          et2=0.
        do 9 j=1,500
         icount(j)=0
         g(j)=0.
9       continue
        do 10 k=0,400
         rhoz(k)=0.d0
         sxx(k)=0.d0
         syy(k)=0.d0
         szz(k)=0.d0
          pn(k)=0.d0
          pt(k)=0.d0
          ue(k)=0.d0
 10    continue
c      set up neighbor table
       isum = 0
       call table(isum)
100    continue
       call driver(ek,etot,dtv,dt6,dt)
         jt=jt+1
           ek1=ek1+ek
           ek2=ek2+ek*ek
           et1=et1+etot
           et2=et2+etot*etot
101     format(i8,2e15.5)
         if(mod(jt,6).eq.0) call table(isum)
         if(mod(jt,jrest).eq.0) call restart(etot,ek,jt,npart,2)
         if(mod(jt,10).eq.0) call pchk
         if(jt.lt.jmax) go to 100
c
c     prepare output
         qq=1./(1.*jt)
          ek1=ek1*qq
          ek2=ek2*qq-ek1*ek1
          et1=et1*qq
          et2=et2*qq-et1*et1
         if (master) write(3,31) ek1,et1
         if (master) write(3,31) ek2,et2
31       format(2e15.6)
c
c      process pair function results
       do 300 j=1,500
         r=0.01*j
         vol=4.*pi*(r*r+.01*r+.01*.01/3.)*.01
         vol=vol/2.
            g(j)=icount(j)/(1.*isum*npart*vol)
300    continue
       if (master) write(3,33)(j,g(j),j=75,500)
33     format(i5,e15.4)
       do 350 j=0,400
         pn(j)=pn(j)/(xmax*ymax*jt)
```

```
          pt(j)=pt(j)/(2.*xmax*ymax*jt)
          rhoz(j)=rhoz(j)/(xmax*ymax*0.1*jt)
          sxx(j)=sxx(j)/(xmax*ymax*0.1*jt)
          syy(j)=syy(j)/(xmax*ymax*0.1*jt)
          szz(j)=szz(j)/(xmax*ymax*0.1*jt)
          ue(j)=ue(j)/(xmax*ymax*0.1*jt)
350     continue
        if (master) then
 write(12,37)(0.1*j,rhoz(j),sxx(j),syy(j),szz(j),j=0,400)
37        format(5e15.5)
          write(13,38)(0.1*j,rhoz(j),pn(j),pt(j),j=0,400)
38        format(4e15.5)
          write(14,39)(0.1*j,rhoz(j),ue(j),j=0,400)
39        format(3e15.5)
        endif
c
c       save final configuration
        call restart(etot,ek,jt,npart,2)
        close(2)
        if (master) close(3)
        close(8)
        call par_end
        call seconds(te,we)
        te = te - ts
        we = we - ws
        if (master) then
  print *,
     . '                    cpu time           wall time'
          print *,'time in accel    ',cpu_accelt,wall_accelt
          print *,'communicate time ',cpuct,commt
          print *,'total time       ',te,we
        endif

        if (master) stop 'md3 finished'
        end
        subroutine driver(ek,etot,dtv,dt6,dt)
        parameter (np=2000)
        dimension x(np),y(np),z(np),u(np),v(np),w(np),p(np)
        dimension ax(np),ay(np),az(np),axm(np),aym(np),azm(np),ap(np)
        dimension axp(np),ayp(np),azp(np),nq(np),ymx(4)
        double precision rhoz(0:400),sxx(0:400),syy(0:400),szz(0:400),
     x pn(0:400),pt(0:400),ue(0:400)
c       common blocks
c
        common /cord/ x,y,z,u,v,w
        common /cacc/ ax,ay,az,axm,aym,azm
        common /cpar/ xmax,xmax2,ymax,ymax2,zmax,zmax2,rm3,rp1
        common /cprf/ rhoz,sxx,syy,szz,pn,pt,ue
c
c       Use the Beeman algorithm
        include 'mpif.h'
        include 'parallel.h'

        do 100 j=1,np
           zmx=1.
           x(j)=x(j)+(dt*u(j)+dt6*(4.*ax(j)-axm(j)))*zmx
           y(j)=y(j)+(dt*v(j)+dt6*(4.*ay(j)-aym(j)))*zmx
```

```
          z(j)=z(j)+(dt*w(j)+dt6*(4.*az(j)-azm(j)))*zmx
c
c        invoke periodic boundary conditions
          if(x(j).gt.xmax) x(j)=x(j)-xmax
          if(x(j).lt.0.0)  x(j)=x(j)+xmax
          if(y(j).gt.ymax) y(j)=y(j)-ymax
          if(y(j).lt.0.0)  y(j)=y(j)+ymax
          if(z(j).gt.zmax) z(j)=z(j)-zmax
          if(z(j).lt.0.0)  z(j)=z(j)+zmax
100     continue
        call accel(axp,ayp,azp,etot)
        ek=0.
        do 200 j=1,np
          u(j)=u(j)+dtv*(2.*axp(j)+5.*ax(j)-axm(j))
          v(j)=v(j)+dtv*(2.*ayp(j)+5.*ay(j)-aym(j))
          w(j)=w(j)+dtv*(2.*azp(j)+5.*az(j)-azm(j))
          ek=ek+u(j)*u(j)+v(j)*v(j)+w(j)*w(j)
c
c       shift forces
          axm(j)=ax(j)
          aym(j)=ay(j)
          azm(j)=az(j)
          ax(j)=axp(j)
          ay(j)=ayp(j)
          az(j)=azp(j)
c       density and stress profiles
         ij=10*z(j)
         rhoz(ij)=rhoz(ij)+1.d0
         sxx(ij)=sxx(ij)+u(j)*u(j)
         syy(ij)=syy(ij)+v(j)*v(j)
         szz(ij)=szz(ij)+w(j)*w(j)
200     continue
        ek=ek/(2.*np)
        etot=etot+ek
        return
        end

        subroutine accel(ax,ay,az,etot)
        parameter (np=2000)
        dimension lr(400000),icount(500),nxstart(np)
        dimension x(np),y(np),z(np),u(np),v(np),w(np),p(np)
        dimension ax(np),ay(np),az(np),ap(np),work(np)
        dimension ve(500,3),vf(500,3),die(500,3),dif(500,3)
        double precision rhoz(0:400),sxx(0:400),syy(0:400),szz(0:400),
      x  pn(0:400),pt(0:400),ue(0:400)
        double precision rhozc(0:400),sxxc(0:400),syyc(0:400),
      x  szzc(0:400),pnc(0:400),ptc(0:400),uec(0:400)
c
c       common blocks
c
        common /cord/ x,y,z,u,v,w
        common /cvef/ ve,vf,die,dif
        common /ctab/ lr,icount,nxstart
        common /cpar/ xmax,xmax2,ymax,ymax2,zmax,zmax2,rm1,rp1
        common /cprf/ rhozc,sxxc,syyc,szzc,pnc,ptc,uec
        include 'mpif.h'
```

```
       include 'parallel.h'
       real*4 accels,accele,dstime,detime
       real*8 ws,we,wstime,wetime

       if (master.and.test) print *,this_process,' Entering accel'
       call seconds(accels,ws)
       ep=0.
       etot=0.
       do 20 j=1,np
         ax(j)=0.
         ay(j)=0.
         az(j)=0.
20     continue
       do j=0,400
 rhoz(j)=0.
 sxx(j)=0.
 syy(j)=0.
 szz(j)=0.
 pn(j)=0.
 pt(j)=0.
 ue(j)=0.
       enddo
       nx=1
       do 50 j=this_process+1,np-1,numprocs
           ij=10*z(j)
   nx=nxstart(j)
30         k=lr(nx)
          nx=nx+1
          if(k.eq.0) go to 50
           ik=10*z(k)
          xx=x(j)-x(k)
          yy=y(j)-y(k)
          zz=z(j)-z(k)
          if(xx.gt.xmax2)  xx=xx-xmax
          if(xx.lt.-xmax2) xx=xx+xmax
          if(yy.gt.ymax2)  yy=yy-ymax
          if(yy.lt.-ymax2) yy=yy+ymax
          if(zz.gt.zmax2)  zz=zz-zmax
          if(zz.lt.-zmax2) zz=zz+zmax
          rr=xx*xx+yy*yy+zz*zz
          if(rr.gt.rm1) go to 45
            if(j.le.1000) then
               if(k.le.1000) then
                  npot=2
               else
                  npot=3
               end if
             else
               if(k.gt.1000) then
                  npot=1
               else
                  npot=3
               end if
             end if
           rr=sqrt(rr)
             r=100.*rr
             if(r.lt.30) go to 60
```

```
             l=int(r)
             alpha=r-l
             phi=ve(l,npot)+alpha*die(l,npot)
             f=vf(l,npot)+alpha*dif(l,npot)
           qk=f/rr
              qj=qk*xx
              ax(j)=ax(j)+qj
              ax(k)=ax(k)-qj
                sxx(ij)=sxx(ij)+0.5*qj*xx
                sxx(ik)=sxx(ik)+0.5*qj*xx
              qj=qk*yy
              ay(j)=ay(j)+qj
              ay(k)=ay(k)-qj
                syy(ij)=syy(ij)+0.5*qj*yy
                syy(ik)=syy(ik)+0.5*qj*yy
              qj=qk*zz
              az(j)=az(j)+qj
              az(k)=az(k)-qj
                szz(ij)=szz(ij)+0.5*qj*zz
                szz(ik)=szz(ik)+0.5*qj*zz
           ep=ep+phi
             ue(ij)=ue(ij)+0.5*phi
             ue(ik)=ue(ik)+0.5*phi
c        Pressure tensor components:
           if(z(j).gt.z(k)) then
             qmax=z(j)
             qmin=z(k)
           else
             qmax=z(k)
             qmin=z(j)
           end if
           il=10*qmin
           ih=10*qmax
           za=abs(zz)
             qn=qk*za
             qt=qk*(xx*xx+yy*yy)
           do 100 kk=il,ih
             zq=0.1*(kk+1)
               if(zq.lt.qmin .or. zq.gt.qmax) go to 45
              pn(kk)=pn(kk)+qn
              pt(kk)=pt(kk)+qt/za
100        continue
45       go to 30
50       continue

 call seconds(dstime,wstime)
 call gsum(ep,1,work)
 call gsum(ax,np,work)
 call gsum(ay,np,work)
 call gsum(az,np,work)
 call gdsum(sxx(0),401,work)
 call gdsum(syy(0),401,work)
 call gdsum(szz(0),401,work)
 call gdsum(pn(0),401,work)
 call gdsum(pt(0),401,work)
 call gdsum(ue(0),401,work)
```

```
 call seconds(detime,wetime)
 cpuct = cpuct + detime - dstime
 commt = commt + wetime - wstime

         do j=0,400
      sxxc(j)=sxxc(j)+sxx(j)
      syyc(j)=syyc(j)+syy(j)
      szzc(j)=szzc(j)+szz(j)
      pnc(j)=pnc(j)+pn(j)
      ptc(j)=ptc(j)+pt(j)
      uec(j)=uec(j)+ue(j)
         enddo
         etot=ep/(1.*np)
         call seconds(accele,we)
 cpu_accelt = cpu_accelt + accele - accels
 wall_accelt = wall_accelt + we - ws
 if (master.and.test) print *,this_process,’ Leaving accel’
         return
60       if (master) write(3,1) r,j,k
1        format(’ r =’,e10.4,2i5)
         stop ’Range trouble’
         end
       subroutine restart(etot,ek,jt,npart,ix)
       parameter (np=2000)
       dimension x(np),y(np),z(np),u(np),v(np),w(np),p(np)
       dimension ax(np),ay(np),az(np),axm(np),aym(np),azm(np),ap(np)
c      common blocks
c
       common /cord/ x,y,z,u,v,w
       common /cacc/ ax,ay,az,axm,aym,azm
       include ’mpif.h’
       include ’parallel.h’
5      format(2i10,2e14.6)
6      format(6f13.6,I6)
7      format(6f13.6,I6)
       jn=8
        if(ix.eq.2) go to 100
         read(jn,5) jt,npart,etot,ek
         read(jn,6)(x(j),y(j),z(j),u(j),v(j),w(j),p(j),j=1,np)
         read(jn,7)(ax(j),ay(j),az(j),axm(j),aym(j),azm(j),ap(j),j=1,np)
         return
100     rewind(jn)
        if (master) then
          write(jn,5) jt,npart,etot,ek
          write(jn,6)(x(j),y(j),z(j),u(j),v(j),w(j),j,j=1,np)
          write(jn,7)(ax(j),ay(j),az(j),axm(j),aym(j),azm(j),j,j=1,np)
endif
        return
        end
       subroutine pot(epsi,ri,palpha)
       dimension ve(500,3),vf(500,3),die(500,3),dif(500,3)
       common /cvef/ ve,vf,die,dif
        do 45 j=1,500
          r=0.01*j
          ve(j,1)= 4.*epsi*(   (ri/r)**12 - (ri/r)**6 )
          vf(j,1)=24.*epsi*(2.*(ri/r)**12 - (ri/r)**6 )/r
          ve(j,2)=2.0*ve(j,1)
```

```
          vf(j,2)=2.0*vf(j,1)
          ve(j,3)= 4.*epsi*(  (1.2*ri/r)**12 - palpha*(ri/r)**6  )
          vf(j,3)=24.*epsi*(2.*(1.2*ri/r)**12 - palpha*(ri/r)**6  )/r
45      continue
        do 92 k=1,3
         do 90 j=1,499
            die(j,k)=ve(j+1,k)-ve(j,k)
            dif(j,k)=vf(j+1,k)-vf(j,k)
90       continue
92      continue
       return
       end
       subroutine table(isum)
       parameter (np=2000)
       dimension x(np),y(np),z(np),u(np),v(np),w(np),p(np)
       dimension lr(400000),icount(500),nxstart(np)
c      common blocks
c
       common /cord/ x,y,z,u,v,w
       common /ctab/ lr,icount,nxstart
       common /cpar/ xmax,xmax2,ymax,ymax2,zmax,zmax2,rm1,rp1
         xmax3=xmax2*ymax2
         nflag=0
         isum=isum+1
         nx=1
       do 50 j=1,np-1
  nxstart(j)=nx
          do 48 k=j+1,np
            xx=abs(x(j)-x(k))
            yy=abs(y(j)-y(k))
            zz=abs(z(j)-z(k))
            if(xx.gt.xmax2) xx=xx-xmax
            if(yy.gt.ymax2) yy=yy-ymax
            if(zz.gt.zmax2) zz=zz-zmax
            rr=xx*xx+yy*yy+zz*zz
            if(rr.gt.rp1) go to 45
             lr(nx)=k
             nx=nx+1
          if(nx.gt.400000) then
1           format('Trouble, nx =',i6,2i5)
          end if
45           if(rr.gt.xmax3) go to 48
                 r=sqrt(rr)
                 ix=100*r+.5
                 if(ix.gt.500) go to 48
                 icount(ix)=icount(ix)+1
48           continue
               lr(nx)=nflag
               nx=nx+1
50     continue
       return
       end
       subroutine pchk
       parameter (np=2000)
       dimension x(np),y(np),z(np),u(np),v(np),w(np),p(np)
       common /cord/ x,y,z,u,v,w
         px=0.
```

```
           py=0.
           pz=0.
         do 10 j=1,np
           px=px+u(j)
           py=py+v(j)
           pz=pz+w(j)
10       continue
           px=px/(1.*np)
           py=py/(1.*np)
           pz=pz/(1.*np)
         do 20 j=1,np
           u(j)=u(j)-px
           v(j)=v(j)-py
           w(j)=w(j)-pz
20       continue
        return
        end
```

APPENDIX B

SIMULATION CODE FOR CHAPTER IV

```
      program newvt1
c     Revised 11-15-00 for surface tension, liquid liquid interface
c     u(z), pchk added 10-23-00. thermostat added on 10sep02.  last
c     updated in sep03.  interfacial area change added on 29oct03.
c     system separation added 21NOV03.  this program works well,
c     and should be suitable for L-J canonical  studies! 25NOV03
c
      parameter (np=1024,nts=3)
      dimension x(np),y(np),z(np),u(np),v(np),w(np),nn(np)
      dimension ax(np),ay(np),az(np),xm(np),ym(np),zm(np),mm(np)
      dimension n(np),m(np)
      dimension lr(400000),ut(np),vt(np),wt(np)
      dimension ve(500,3),vf(500,3),die(500,3),dif(500,3)
      dimension g(500),icount(500)
      dimension tr(nts),trv(nts),trf(nts),qmr(nts)
      double precision rhoz(0:320),sxx(0:320),syy(0:320),szz(0:320),
     x  pn(0:320),pt(0:320),ue(0:320),rhoz1(0:320),rhoz2(0:320)
      double precision ek1,ek2,et1,et2

c
c     common blocks
c
      common /cord/ x,y,z,u,v,w,ut,vt,wt,nn,mm
      common /cacc/ ax,ay,az,xm,ym,zm,n,m
      common /ctab/ lr,icount,isum
      common /cvef/ ve,vf,die,dif
      common /cpar/ xmax,xmax2,ymax,ymax2,zmax,zmax2,rm1,rp1
      common /cprf/ rhoz,sxx,syy,szz,pn,pt,ue,rhoz1,rhoz2
      common /ctcf/ dt,dt2,d2t,zmx
c
c     Common block for thermostat variables
c
      common /ctos/ tr,trv,trf,qmr,ttr
c
c     open files
c
      open(2,file='md32')
      open(3,file='md3out')
```

```
       open(8,file='md38')
c
c     read in startup information
c
       read(2,1) j0,jmax,npart,jrest
 1     format(4i10)
 2     format(6f10.5)
 3     format(2f10.2)
       read(2,2) dt,ene,xmax,ymax,zmax,rm1
c
c     Thermostat variables
c
       read(2,3) qmr(1),ttr
       do 10 j=2,nts
          qmr(j)=qmr(1)/(1.*np)
 10    continue

c
       close(2)
c
c     rm1 is the range of the interaction
c     rp1 is the square of the corresponding distance
c       for use in construction of the neiqhbor table.
c
c     list what has been provided
c
       write(3,1) j0,jmax,npart,jrest
       write(3,2) dt,ene,xmax,ymax,zmax,rm1
c
c     rework the range parameters
       rp1=(rm1+0.3)**2
           rm1=rm1**2
c
c     specify half-box size
       xmax2=0.5*xmax
       ymax2=0.5*ymax
       zmax2=0.5*zmax
c
c     generate  pi
         pi=4.*atan(1.)
         dt2=dt*dt
         d2t=dt/2.
c
c     read in restart information
c

       call restart(etot,ek,jt,npart,1,mm,m)
c
c     set up potential and force
c
         epsi=1.
         sig =1.
 palpha =0.
       call pot(epsi,sig,palpha)
c
       zmx = 1.
c
c     set initial values
c
```

```
          ek1=0.
          ek2=0.
          et1=0.
          et2=0.
c
c     Set thermostat variables
c
       do 12 j=1,nts
          tr(j)=0.
          trv(j)=0.
          trf(j)=0.
 12    continue
       do 8 j=1,np
          ut(j)=0.
          vt(j)=0.
          wt(j)=0.
 8     continue
       do 9 j=1,500
         icount(j)=0
         g(j)=0.
 9     continue
       do 1000 k=0,320
          rhoz(k)=0.d0
  rhoz1(k)=0.d0
  rhoz2(k)=0.d0
          sxx(k)=0.d0
          syy(k)=0.d0
          szz(k)=0.d0
          pn(k)=0.d0
          pt(k)=0.d0
          ue(k)=0.d0
 1000  continue
c     set up neighbor table
       isum = 0
       call table(isum)
c
c     Determine the Kinetic energy
c
       do 11 i=1,np
          ek=ek+u(i)*u(i)+v(i)*v(i)+w(i)*w(i)
 11    continue
       ek=ek/(1.*np)
       trf(1)=(ek-3.*ttr)*np
 100   continue
       call driver(isum,icount,jt,ek,etot,mm,m)
         jt=jt+1
           ek1=ek1+ek
           ek2=ek2+ek*ek
           et1=et1+etot
           et2=et2+etot*etot
        write(6,101) jt,ek,etot
 101       format(i8,2e17.8)
           if(mod(jt,6).eq.0) call table(isum)
           if(mod(jt,jrest).eq.0) call restart(etot,ek,jt,npart,2,mm,m)
           if(mod(jt,25).eq.0) call pchk
           if(jt.lt.jmax) go to 100
c
```

```
c    prepare output
c
            qq=1./(1.*jt)
            ek1=ek1*qq
            ek2=ek2*qq-ek1*ek1
            et1=et1*qq
            et2=et2*qq-et1*et1
            write(3,31) ek1,et1
            write(3,31) ek2,et2
c           write(6,19) jt,ene,etot,ek
c           write(6,*) ek
 19        format(4e15.6)
 31         format(2e15.6)
c
c     process pair function results
c
            do 300 j=1,500
               r=0.01*j
               vol=4.*pi*(r*r+.01*r+.01*.01/3.)*.01
               vol=vol/2.
               g(j)=icount(j)/(1.*isum*npart*vol)
 300        continue
       write(3,33)(j,g(j),j=75,500)
 33    format(i5,e15.4)
c
       do 350 j=0,320
          pn(j)=pn(j)/(xmax*ymax*jt)
          pt(j)=pt(j)/(2.*xmax*ymax*jt)
          rhoz(j)=rhoz(j)/(xmax*ymax*0.1*jt)
  rhoz1(j)=rhoz1(j)/(xmax*ymax*0.1*jt)
  rhoz2(j)=rhoz2(j)/(xmax*ymax*0.1*jt)
          sxx(j)=sxx(j)/(xmax*ymax*0.1*jt)
          syy(j)=syy(j)/(xmax*ymax*0.1*jt)
          szz(j)=szz(j)/(xmax*ymax*0.1*jt)
          ue(j)=ue(j)/(xmax*ymax*0.1*jt)
 350   continue
       write(12,37)(0.1*j,rhoz(j),sxx(j),syy(j),szz(j),j=0,320)
 37    format(5e15.5)
       write(13,38)(0.1*j,rhoz(j),pn(j),pt(j),j=0,320)
 38    format(4e15.5)
       write(14,39)(0.1*j,ue(j),j=0,320)
 39    format(2e15.5)
       write(15,40)(0.1*j,rhoz(j),rhoz1(j),rhoz2(j),j=0,320)
 40    format(4e15.5)
c
c      save final configuration
c
       call restart(etot,ek,jt,npart,2,mm,m)
       close(2)
       close(3)
       close(8)
       end

       subroutine driver(isum,icount,jt,ek,etot,mm,m)
       parameter (np=1024,nts=3)
       dimension x(np),y(np),z(np),u(np),v(np),w(np),nn(np)
       dimension ax(np),ay(np),az(np),xm(np),ym(np),zm(np),mm(np)
```

```
      dimension axp(np),ayp(np),azp(np),nq(np),ymx(4)
      dimension n(np),m(np)
      dimension ut(np),vt(np),wt(np)
      dimension trt(nts),tr(nts),trv(nts),trf(nts),qmr(nts)
      double precision rhoz(0:320),sxx(0:320),syy(0:320),szz(0:320),
     x pn(0:320),pt(0:320),ue(0:320),rhoz1(0:320),rhoz2(0:320)
      double precision ek1,ek2,et1,et2

c     common blocks
c
      common /cord/ x,y,z,u,v,w,ut,vt,wt,nn
      common /cacc/ ax,ay,az,xm,ym,zm,n
      common /cpar/ xmax,xmax2,ymax,ymax2,zmax,zmax2,rm3,rp1
      common /cprf/ rhoz,sxx,syy,szz,pn,pt,ue,rhoz1,rhoz2
      common /ctos/ tr,trv,trf,qmr,ttr
      common /ctcf/ dt,dt2,d2t,zmx
c
c     Use the Velocity Verlet Algorithm
c
      ek=0.

      do 99 j=1,np
c
c    UPDATE THE POSITIONS & DETERMINE VELOCITIES
c
      x(j)=x(j)+dt*u(j)+0.5*dt2*(ax(j)*zmx)
      y(j)=y(j)+dt*v(j)+0.5*dt2*(ay(j)*zmx)
      z(j)=z(j)+dt*w(j)+0.5*dt2*(az(j)*zmx)
c
c      invoke periodic boundary conditions
c
         if(x(j).gt.xmax) x(j)=x(j)-xmax
         if(x(j).lt.0.0)  x(j)=x(j)+xmax
         if(y(j).gt.ymax) y(j)=y(j)-ymax
         if(y(j).lt.0.0)  y(j)=y(j)+ymax
         if(z(j).gt.zmax) z(j)=z(j)-zmax
         if(z(j).lt.0.0)  z(j)=z(j)+zmax

      u(j)=u(j)+0.5*dt*(ax(j)*zmx)
      v(j)=v(j)+0.5*dt*(ay(j)*zmx)
      w(j)=w(j)+0.5*dt*(az(j)*zmx)
      ek=ek+u(j)*u(j)+v(j)*v(j)+w(j)*w(j)
 99   continue
c
c    DETERMINE THE THERMOSTAT QUANTITIES
c
      trf(1)=(ek-3.*ttr*np)-trv(1)*trv(2)/qmr(2)
      trf(2)=trv(1)**2/qmr(1)-ttr-trv(2)*trv(3)/qmr(3)
      trf(nts)=trv(2)**2/qmr(2)-ttr
      do 101 j=1,nts
         tr(j)=tr(j)+trv(j)*dt+0.5*dt2*trf(j)
         trv(j)=trv(j)+0.5*dt*trf(j)
 101  continue
c
c    DETERMINE NEW ACCELERATION
c
     call accel(axp,ayp,azp,etot)
```

```
      ek=0.
c
c     UPDATE THE VELOCITIES
c
      do 200 j=1,np
c
       u(j)=u(j)+0.5*dt*axp(j)*zmx
       v(j)=v(j)+0.5*dt*ayp(j)*zmx
       w(j)=w(j)+0.5*dt*azp(j)*zmx
       ek=ek+u(j)*u(j)+v(j)*v(j)+w(j)*w(j)
c
c     SET TEMPORARY VELOCITY
c
       ut(j) = u(j)
       vt(j) = v(j)
       wt(j) = w(j)

 200  continue
c
c    THERMOSTAT SECTION II
c
      trf(1)=(ek-3.*ttr*np)-trv(1)*trv(2)/qmr(2)
      trf(2)=trv(1)**2/qmr(1)-ttr-trv(2)*trv(3)/qmr(3)
      trf(nts)=trv(2)**2/qmr(2)-ttr

      do 1011 j=1,nts
         tr(j)=tr(j)+trv(j)*dt+0.5*dt2*trf(j)
         trv(j)=trv(j)+0.5*dt*trf(j)
         trt(j)=trv(j)
 1011 continue

c
c    ITERATIVE LOOP & NEW ALPHA
c
      do 220 L=1,6
            ek=0.
         do 230 j=1,np
             u(j)= ut(j) - 0.5*dt*trv(1)*u(j)/qmr(1)
             v(j)= vt(j) - 0.5*dt*trv(1)*v(j)/qmr(1)
             w(j)= wt(j) - 0.5*dt*trv(1)*w(j)/qmr(1)
             ek=ek+(u(j)*u(j)+v(j)*v(j)+w(j)*w(j))*zmx
 230     continue
          trf(1)=(ek-3.*ttr*np)-trv(1)*trv(2)/qmr(2)
          trf(2)=trv(1)**2/qmr(1)-ttr-trv(2)*trv(3)/qmr(3)
          trf(nts)=trv(2)**2/qmr(2)-ttr
             do 1012 j=1,nts
                trv(j)=trt(j)+0.5*dt*trf(j)
 1012        continue
 220  continue
ek=0.
c
c    SHIFT ACCELERATIONS, INCREMEMT KINETIC ENERGY
c
      do 204 j=1,np
         xm(j)=ax(j)-trv(1)*u(j)/qmr(1)
         ym(j)=ay(j)-trv(1)*v(j)/qmr(1)
         zm(j)=az(j)-trv(1)*w(j)/qmr(1)
```

```
         ax(j)=axp(j)-trv(1)*u(j)/qmr(1)
         ay(j)=ayp(j)-trv(1)*v(j)/qmr(1)
         az(j)=azp(j)-trv(1)*w(j)/qmr(1)
         ek=ek+u(j)*u(j)+v(j)*v(j)+w(j)*w(j)
c
c      density and stress profiles
c
          ij=10*z(j)
  if(mm(j).eq.1) then
rhoz1(ij)=rhoz1(ij)+1.d0
    rhoz2(ij)=0.
  else
rhoz1(ij)=0.
rhoz2(ij)=rhoz2(ij)+1.d0
  endif
          rhoz(ij)=rhoz1(ij)+rhoz2(ij)+1.d0
          sxx(ij)=sxx(ij)+u(j)*u(j)
          syy(ij)=syy(ij)+v(j)*v(j)
          szz(ij)=szz(ij)+w(j)*w(j)
 204   continue
       ek=ek/(2.*np)
       etot=etot+ek
       return
       end

       subroutine accel(ax,ay,az,etot)
       parameter (np=1024)
       dimension lr(400000),icount(500)
      dimension x(np),y(np),z(np),u(np),v(np),w(np),nn(np),mm(np)
       dimension ax(np),ay(np),az(np),ap(np)
       dimension n(np),m(np)
       dimension ve(500,3),vf(500,3),die(500,3),dif(500,3)
       double precision rhoz(0:320),sxx(0:320),syy(0:320),szz(0:320),
     x  pn(0:320),pt(0:320),ue(0:320),rhoz1(0:320),rhoz2(0:320)
       double precision ek1,ek2,et1,et2
c
c      common blocks
c
       common /cord/ x,y,z,u,v,w,nn,mm
       common /cvef/ ve,vf,die,dif,n,m
       common /ctab/ lr,icount
       common /cpar/ xmax,xmax2,ymax,ymax2,zmax,zmax2,rm1,rp1
       common /cprf/ rhoz,sxx,syy,szz,pn,pt,ue,rhoz1,rhoz2
       common /ctcf/ dt,dt2,d2t,zmx

       ep=0.
       etot=0.
       do 20 j=1,np
          ax(j)=0.
          ay(j)=0.
          az(j)=0.
 20    continue
       nx=1
       do 50 j=1,np-1
          ij=10*z(j)
 30       k=lr(nx)
          nx=nx+1
```

```
          if(k.eq.0) go to 50
           ik=10*z(k)
          xx=x(j)-x(k)
          yy=y(j)-y(k)
          zz=z(j)-z(k)
          if(xx.gt.xmax2)  xx=xx-xmax
          if(xx.lt.-xmax2) xx=xx+xmax
          if(yy.gt.ymax2)  yy=yy-ymax
          if(yy.lt.-ymax2) yy=yy+ymax
          if(zz.gt.zmax2)  zz=zz-zmax
          if(zz.lt.-zmax2) zz=zz+zmax
          rr=xx*xx+yy*yy+zz*zz
          if(rr.gt.rm1) go to 45
            if(j.le.512) then
               if(k.le.512) then
                  npot=2
               else
                  npot=3
               end if
             else
               if(k.gt.512) then
                  npot=1
               else
                  npot=3
               end if
             end if
           rr=sqrt(rr)
             r=100.*rr
             if(r.lt.30) go to 60
             l=int(r)
             alpha=r-l
             phi=ve(l,npot)+alpha*die(l,npot)
             f=vf(l,npot)+alpha*dif(l,npot)
           qk=f/rr
              qj=qk*xx
              ax(j)=ax(j)+qj
              ax(k)=ax(k)-qj
                sxx(ij)=sxx(ij)+0.5*qj*xx
                sxx(ik)=sxx(ik)+0.5*qj*xx
              qj=qk*yy
              ay(j)=ay(j)+qj
              ay(k)=ay(k)-qj
                syy(ij)=syy(ij)+0.5*qj*yy
                syy(ik)=syy(ik)+0.5*qj*yy
              qj=qk*zz
              az(j)=az(j)+qj
              az(k)=az(k)-qj
                szz(ij)=szz(ij)+0.5*qj*zz
                szz(ik)=szz(ik)+0.5*qj*zz
           ep=ep+phi
             ue(ij)=ue(ij)+0.5*phi
             ue(ik)=ue(ik)+0.5*phi
c        Pressure tensor components:
           if(z(j).gt.z(k)) then
             qmax=z(j)
             qmin=z(k)
```

```
           else
             qmax=z(k)
             qmin=z(j)
           end if
           il=10*qmin
           ih=10*qmax
           za=abs(zz)
             qn=qk*za
             qt=qk*(xx*xx+yy*yy)
           do 100 kk=il,ih
              zq=0.1*(kk+1)
               if(zq.lt.qmin .or. zq.gt.qmax) go to 45
              pn(kk)=pn(kk)+qn
              pt(kk)=pt(kk)+qt/za
 100       continue
 45        go to 30
 50     continue
         etot=ep/(1.*np)
         return
 60      write(3,1) r,j,k
 1       format(' r =',e10.4,2i5)
         stop 'Range trouble'
         end
       subroutine restart(etot,ek,jt,npart,ix,mm,m)
       parameter (np=1024)
       dimension x(np),y(np),z(np),u(np),v(np),w(np),nn(np)
       dimension ax(np),ay(np),az(np),xm(np),ym(np),zm(np),mm(np)
       dimension n(np),m(np)
c
c      common blocks
c
       common /cord/ x,y,z,u,v,w,nn
       common /cacc/ ax,ay,az,xm,ym,zm
 5     format(2i10,2e14.6)
 6     format(6f13.6,i6,i3)
 7     format(6f13.6,I6,I3)
       jn=8
        if(ix.eq.2) go to 100
      read(jn,5) jt,npart,etot,ek
      read(jn,6)(x(j),y(j),z(j),u(j),v(j),w(j),nn(j),mm(j),j=1,np)
      read(jn,7)(ax(j),ay(j),az(j),xm(j),ym(j),zm(j),n(j),m(j),j=1,np)
         return
 100     rewind(jn)
      write(jn,5) jt,npart,etot,ek
      write(jn,6)(x(j),y(j),z(j),u(j),v(j),w(j),j,mm(j),j=1,np)
      write(jn,7)(ax(j),ay(j),az(j),xm(j),ym(j),zm(j),j,m(j),j=1,np)
        return
        end
       subroutine pot(epsi,ri,palpha)
       dimension ve(500,3),vf(500,3),die(500,3),dif(500,3)
       common /cvef/ ve,vf,die,dif
       do 45 j=1,500
          r=0.01*j
          ve(j,1)= 4.*epsi*(   (ri/r)**12 - (ri/r)**6 )
          vf(j,1)=24.*epsi*(2.*(ri/r)**12 - (ri/r)**6 )/r
          ve(j,2)=2.0*ve(j,1)
          vf(j,2)=2.0*vf(j,1)
```

```
          ve(j,3)= 4.*epsi*(   (1.2*ri/r)**12 - palpha*(ri/r)**6  )
          vf(j,3)=24.*epsi*(2.*(1.2*ri/r)**12 - palpha*(ri/r)**6  )/r
 45    continue
       do 92 k=1,3
          do 90 j=1,499
            die(j,k)=ve(j+1,k)-ve(j,k)
            dif(j,k)=vf(j+1,k)-vf(j,k)
 90       continue
 92    continue
       return
       end
       subroutine table(isum)
       parameter (np=1024)
       dimension x(np),y(np),z(np),u(np),v(np),w(np),nn(np)
       dimension lr(400000),icount(500)
c
c      common blocks
c
       common /cord/ x,y,z,u,v,w
       common /ctab/ lr,icount
       common /cpar/ xmax,xmax2,ymax,ymax2,zmax,zmax2,rm1,rp1,dt
         xmax3=xmax2*ymax2
        nflag=0
         isum=isum+1
         nx=1
       do 50 j=1,np-1
          do 48 k=j+1,np
             xx=abs(x(j)-x(k))
             yy=abs(y(j)-y(k))
             zz=abs(z(j)-z(k))
             if(xx.gt.xmax2) xx=xx-xmax
             if(yy.gt.ymax2) yy=yy-ymax
             if(zz.gt.zmax2) zz=zz-zmax
             rr=xx*xx+yy*yy+zz*zz
             if(rr.gt.rp1) go to 45
             lr(nx)=k
             nx=nx+1
             if(nx.gt.400000) then
 1              format('Trouble, nx =',i6,2i5)
          end if
 45       if(rr.gt.xmax3) go to 48
                 r=sqrt(rr)
                 ix=100*r+.5
                 if(ix.gt.500) go to 48
                 icount(ix)=icount(ix)+1
 48           continue
               lr(nx)=nflag
               nx=nx+1
 50         continue
       return
       end
       subroutine pchk
       parameter (np=1024)
       dimension x(np),y(np),z(np),u(np),v(np),w(np)
       common /cord/ x,y,z,u,v,w
         px=0.
         py=0.
```

```
        pz=0.
      do 10 j=1,np
         px=px+u(j)
         py=py+v(j)
         pz=pz+w(j)
10    continue
        px=px/(1.*np)
        py=py/(1.*np)
        pz=pz/(1.*np)
        do 20 j=1,np
           u(j)=u(j)-px
           v(j)=v(j)-py
           w(j)=w(j)-pz
20      continue
     return
     end
```

APPENDIX C

BIBLIOGRAPHY

[1] N.K. Adam. *The Physics and Chemistry of Surfaces.* Oxford Univ. Press, New York.

[2] D. Nicholson and N.G. Parsonage. *Computer Simulation and the Statistical Mechanics of Adsorption.* Academic Press, New York.

[3] G. Navascues. Liquid surfaces: theory of surface tension. *Rep. Prog. Phys.*, 42:1131–1186, 1979.

[4] A.W. Adamson. *Physical chemistry of surfaces.* John Wiley Sons, New York.

[5] L.D. Landau, E.M. Lifshitz, and L.P. Pitaevskii. *Statistical Physics 3rd Edition.* Paragom Press, New York.

[6] J.M. Haile. *Molecular Dynamics Simulation: Elementary Methods.* John Wiley Sons, New York.

[7] M.P. Allen and D.J. Tildesley. *Computer Simulation of Liquids.* Oxford Univ. Press, New York.

[8] D.C. Rapaport. *The art of molecular dynamics simulation.* Cambridge Univ. Press, New York.

[9] C. Jarzynski. Nonequilibrium equality for free energy differences. *Phys. Rev. Let.*, 78:2690–2693, 1997.

[10] C. Rickwardt, P. Nielaba, M.H. Muser, and K. Binder. Path integral Monte Carlo simulations of silicates. *Phys. Rev. B*, 63:45204:1–8, 2001.

[11] M. Presber, D. Loding, and R. Martonák. Orientational phase transitions in molecular n_2 solids: A path-integral Monte Carlo study. *Phys. Rev. B*, 58:11937–11943, 1998.

[12] J.L. Garcıa-Palacios and F.J. L'azaro. Langevin-dynamics study of the dynamical properties of small magnetic particles. *Phys. Rev. B*, 58:14937–14958, 1998.

[13] G.J. Martyna, M.L. Klein, and M. Tuckerman. Nosé-Hoover chains: The canonical ensemble via continuous dynamics. *J. Chem. Phys.*, 97:2635–2643, 1992.

[14] E. Díaz-Herrera, J. Alejandre, F. Ramírez-Santiago, and F. Forstmann. Interfacial tension behavior of binary and ternary mixtures of partially miscible Lennard-Jones fluids: A molecular dynamics simulation. *J. Chem. Phys.*, 110:8084–8089, 1999.

[15] J.K. Johnson, J.A. Zollweg, and K.E. Gubbins. The Lennard-Jones equation of state revisited. *Mol. Phys*, 78:591–618, 1993.

[16] J.J. Nicolas, K.E. Gubbins, W.B. Street, and D.J. Tildesley. Equation of state for the Lennard-Jones fluid. *Mol. Phys.*, 37:1429–1454, 1979.

[17] I. Prigogine, R. Defay, and A. Bellemans. *Surface tension and adsorption.* John Wiley Sons, New York.

[18] L. Verlet. Computer Experiments on classical fluids. I. Thermodynamical properties of Lennard-Jones molecules. *Phys. Rev.*, 159:98–103, 1967.

[19] R.D. Mountain. Neighbor tables for molecular dynamics simulations. *NISTIR*, 5545:1–11, 1994.

[20] J.W. Gibbs. *Elementary Principles in Statistical Mechanics.* University Press, Cambridge.

[21] R.D. Mountain and D. Thirumalai. Activated dynamics, loss of ergodicity, and transport in supercooled liquids. *Phys. Rev. E*, 47:479–489, 1993.

[22] K.S.C. Freeman and I.R. McDonald. Molecular theory of surface tension. *Mol. Phys.*, 26:529–537, 1973.

[23] A.I. Borisenko and I.E. Tarapov. *Vector and Tensor Analysis.* Dover, New York.

[24] J.H. Irving and J.G. Kirkwood. The Statistical Mechanical theory of transport processes. iv. The equation of hydrodynamics. *J. Chem. Phys.*, 18:817–829, 1950.

[25] F. Varnik, J. Baschnagel, and K. Binder. Molecular dynamics results on the pressure tensor of polymer films. *J. Chem. Phys.*, 113:4444–4453, 2000.

[26] C.A. Croxton. *Statistical Mechanics of The Liquid Surface.* John Wiley Sons, New York.

[27] D.J. Evans and G.P. Morris. *Statistical Mechanics of Nonequilibrium Liquids.* Academic Press, London.

[28] B.D. Todd, D.J. Evans, and P.J. Daivis. Pressure tensor for inhomogeneous fluids. *Phys. Rev. E, Stat. Phys. Plasmas Fluids Relat. Interdiscip. Top. (USA)*, 52:1627–1638, 1995.

[29] M.J. Haye and C. Bruin. Molecular dynamics study of the curvature correction to the surface tension. *J. Chem. Phys*, 100:556–559, 1994.

[30] M. Rao and B.J. Berne. On the location of surface of tension in the planar interface between liquid and vapour. *Mol. Phys.*, 37:455–461, 1979.

[31] S.J. Hemingway, J.R. Henderson, and J.S. Rowlinson. The density profile and surface tension of a drop. *Far. Symp. of the Chem. Soc.*, 16:33–43, 1981.

[32] J.P.R.B. Walton, D.J. Tildesley, J.S. Rowlinson, and J.R. Henderson. The pressure tensor at the planar surface of a liquid. *Mol. Phys.*, 48:1357–1368, 1983.

[33] L.A. Turkevich and J.A. Mann. Pressure dependence of the interfacial tension between fluid phases. 1. Formalism and application to simple fluids. *Langmuir*, 6:445–456, 1990.

[34] L.A. Turkevich and J.A. Mann. Pressure dependence of the interfacial tension between fluid phases. 2. Application to liquid-vapor interfaces of amphiphilic solutions. *Langmuir*, 6:457–470, 1990.

[35] I. Napari and A. Laaksonen. The effect of potential truncation on the gas-liquid surface tension of planar interfaces and droplets. *J. Chem. Phys.*, 114:5796–5801, 2001.

[36] G.N. Lewis and M. Randall. *Thermodynamics, 2nd edition.* McGraw-Hill, New York.

[37] E.A. Guggenheim. *Thermodynamics.* North Holland, Amsterdam.

[38] E.A. Guggenheim. The Thermodynamics of Interfaces in Systems of Several Components. *Trans. Faraday Soc.*, 36:397, 1940.

[39] S.E. Feller, Y. Zhang, R.W. Pastor, and B.R. Brooks. Computer simulation of liquid/liquid interfaces. I. Theory and application to octane water. *J. Chem. Phys.*, 103:10252–10266, 1995.

[40] S.E. Feller, Y. Zhang, and R.W. Pastor. Computer simulation of liquid-liquid interfaces. II. Surface tension-area dependence of a bilayer and monolayer. *J. Chem. Phys.*, 103:10267–10276, 1995.

[41] S.E. Feller and R.W.Pastor. Constant surface tension simulations of lipid bilayers: The sensitivity of surface areas and compressibilities. *J. Chem. Phys.*, 111:1281–1287, 1999.

[42] T.E. Faber. *An Introduction to the Theory of Liquid Metals.* Cambridge University Press, London, New York.

[43] J. Stecki and S. Toxvaerd. Correlations in the liquid interfaces of simple liquids. *J. Chem. Phys.*, 103:9763–9771, 1995.

[44] J. Stecki and S. Toxvaerd. The liquid-liquid interface of simple liquids. *J. Chem. Phys.*, 103:4352–4359, 1995.

[45] S. Iatsevitch and F. Forstmann. Structure and surface tension of interfaces between demixing liquids: model calculations using integral equations. *J. Phys., Condens. Matter.*, 13:4769–4787, 2001.

[46] M. Lifschitz and K.F. Freed. Interfacial behavior of compressible polymer blends. *J. Chem. Phys.*, 98:8994–9013, 1993.

[47] M. Lifschitz and K. F. Freed. Interfacial behavior of phase separated asymmetric compressible binary polymer blends. *J. Chem. Phys.*, 105:1633–1645, 1996.

[48] C.D. Holcomb, P. Clancy, and J.A. Zollweg. A critical study of the simulation of the liquid-vapour interface of a lennard-jones fluid. *Mol. Phys.*, 78:437–459, 1993.

[49] G.A. Chapela, G. Saville, S.M. Thompson, and J.S. Rowlinson. Computer simulation of a gas-liquid surface. i. *J. Chem. Soc. Faraday Trans. II*, 73:1133–1144, 1977.

[50] M. Meyer, M. Mareschal, and M. Hayoun. Computer modeling of a liquid-liquid interface. *J. Chem. Phys.*, 89:1067–1073, 1988.

[51] M.P. Gelfand and M.E. Fisher. Finite-size effects in fluid interfaces. *Physica A*, 166:1–74, 1990.

[52] D. Levesque and L. Verlet. Molecular Dynamics and time reversibility. *J. Stat. Phys.*, 72:519–537, 1993.

[53] J.H. Irving and J.G. Kirkwood. The Statistical Mechanical theory of transport processes. IV. The equations of hydrodynamics. *J. Chem. Phys.*, 18:817–829, 1950.

[54] D.M. Zuckerman and T.B. Woolf. Overcoming finite-sampling errors in fast-switching free-energy estimates: Extrapolative analysis of a molecular system. *Chem. Phys. Let.*, 351:445–453, 2002.

[55] D. Frenkel and B. Smit. *Understanding Molecular Simulations.* Academic, New York, 1996.

[56] D. Chandler. *Introduction to Modern Statistical Mechanics.* Oxford University Press, New York, 1987.

[57] J. Liphardt, S. Dumont, S.B. Smith, I. Tinoco, and C. Bustemante. Equilibrium information from nonequilibrium measurements in an experimental test of Jarzynski's equality. *Science*, 296:1832–1835, 2002.

[58] G. Hummer. Fast-growth thermodynamic integration: Error and efficiency analysis. *J. Chem. Phys.*, 114:7330–7337, 2001.

[59] D.A. Hendrix and C. Jarzynski. A "fast growth" method of computing free energy differences. *J. Chem. Phys.*, 114:5974–5981, 2001.

[60] R.W. Zwanzig. High-Temperature equation of state by a perturbation method. I. Nonpolar gases. *J. Chem. Phys.*, 22:1420–1426, 1954.

[61] F. Reif. *Fundamentals of Statistical and Thermal Physics.* McGraw-Hill, New York, 1965.

[62] J. Hermans. Simple analysis of noise and hysteresis in (slow-growth) free energy simulations. *J. Phys. Chem.*, 95:9029–9032, 1991.

[63] J.G. Kirkwood. Statistical Mechanics of fluid mixtures. *J. Chem. Phys.*, 3:300–313, 1935.

[64] G.J. Martyna, D.L. Tobias, and M.L. Klein. Constant pressure molecular dynamics algorithms. *J. Chem. Phys.*, 101:4177– 4189, 1994.

[65] L.D. Landau and E.M. Lifshitz. *Theory of Elasticity.* Pergamon Press, New York.

[66] A.N. Parikh, D.L. Allara, I.B. Azouz, and R. Rondelez. An intrinsic relationship between molecular structure in self-assembled n-Alkylsiloxane monolayers and deposition temperature. *J. Phys. Chem.*, 98:7577–7590, 1994.

[67] J.B. Brzoska, I.B. Azouz, and F. Rondelez. Silanization of solid substrates: A step toward reproducibility. *Langmuir*, 10:4367–4373, 1994.

[68] M.M Sung, C. Carraro, O.W. Yauw, Y. Kim, and R. Maboudian. Reversible liquid-liquid transitions in the early stages of monolayer self-assembly. *J. Phys. Chem. B*, 104:1556–1559, 2000.

[69] A. Parikh and D.L. Allara. Quantitative determination of molecular structure in multilayered thin films of biaxial and lower symmetry from photon spectroscopies. I. Reflection infrared vibrational spectroscopy. *J. Chem. Phys.*, 96:927–945, 1992.

[70] R.H. Terrill, T.A. Tanzer, and P.W. Bohn. Structural evolution of Hexadecanethiol monolayers on Gold during assembly: Substrate and concentration dependence of monolayer structure and crystallinity. *Langmuir*, 14:845–854, 1998.

[71] J. Hautman and M.L. Klein. Simulation of a monolayer of alkyl thiol chains. *J. Chem. Phys.*, 91:4994–5001, 1989.

[72] J.H.R. Clarke and D. Brown. Molecular Dynamics computer simulation of chain molecule liquids. *Mol. Phys.*, 58:815–825, 1986.

[73] P. Schofield. Computer Simulation studies of the liquid state. *Comp. Phys. Comm.*, 5:17–23, 1973.

[74] D. Beeman. Some Multistep Methods for use in Molecular Dynamics simulation. *J. Comp. Phys.*, 20:130–139, 1976.

[75] D.L. Allara, A.N. Parikh, and F. Rondelez. Evidence for a unique chain organization in long chain Silane monolayers deposited on two widely different solid substrates. *Langmuir*, 11:2357–2360, 1994.

[76] P. Harder, M. Grunze, R. Dahint, G.M. Whitesides, and P.E. Laibinis. Molecular conformation in oligio(ethylene glycol)-terminated self-assembled monolayers on gold

and silver surfaces determines their ability to resist protein adsorption. *J. Phys. Chem. B*, 102:426–436, 1998.

[77] A.J. Pertsin and M. Grunze. Computer simulation of water near the surface of oligo(ethylene glycol)-terminated alkanethiol self-assembled monolayers. *Langmuir*, 16:8829–8841, 2000.

[78] H.J. Taunton, C. Toprakcioglu, L.J. Fetters, and J. Klein. Forces between surfaces bearing terminally anchored polymer chains in good solvents. *Nature*, 332:712–714, 1988.

[79] S.I. Jeon and J.D. Andrade. Protein-Surface interactions in the presence of polyethylene oxide. *J. Coll. Interface Sci.*, 142:159–165, 1991.

[80] S.I. Jeon, H. Lee, J.D. Andrade, and P.G. De Gennes. Protein-Surface interactions in the presence of polyethylene oxide. *J. Coll. Interface Sci.*, 142:149–158, 1991.

[81] R.L.C. Wang, H.J. Kreuzer, and M. Grunze. Molecular conformation and solvation of oligo(ethylene glycol)-terminated self-assembled monolayers and their resistance to protein adsorption. *J. Phys. Chem. B*, 101:9767–9773, 1997.

[82] D.J. Vanderah, C.W. Meuse, V. Silin, and A. Plant. Synthesis and characterization of self-assembled monolayers of alkylated 1-thiahexa(ethylene oxide) compounds on gold. *Langmuir*, 14:6916–6923, 1998.

[83] R. Valiokas, S. Svedhem, S.C.T. Svensson, and B. Liedberg. Self-assembled monolayers of oligo(ethylene glycol)-terminated and amide group containing alkanethiolates on gold. *Langmuir*, 15:3390–3394, 1999.

[84] D.J. Vanderah, C.P. Pham, S.K. Springer, V. Silin, and C.W. Meuse. Characterization of a series of self-assembled monolayers of alkylated 1-thiaoligo(ethylene oxides)$_{4-8}$ on gold. *Langmuir*, 16:6527–6532, 2000.

[85] A.J. Pertsin, M. Grunze, and I.A. Garbuzova. Low-Energy configurations of Methoxy

triethylene glycol terminated alkanethiol self-assembled monolayers and their relevance to protein adsorption. *J. Phys. Chem. B*, 102:4918–4926, 1998.

[86] D.J. Vanderah, G. Valincius, and C.W. Meuse. Self-assembled monolayers of methyl 1-thiahexa(ethylene oxide) for the inhibition of protein adsorption. *Langmuir*, 18:4674–4680, 2002.

[87] D.J. Vanderah, H. La, J. Arsenault, R.S. Gates, V. Silin, and C.W. Meuse. Structural variations and ordering conditions for the self-assembled monolayers of $HS(CH_2CH_2O)_{3-6}CH_3$. *Langmuir*, 19:3752–3756, 2003.

[88] B. Lin, P.T. Boinske, and J.W. Halley. A molecular dynamics model of the amorphous regions of polyethylene oxide. *J. Chem. Phys*, 105:1668–1681, 1996.

[89] T. Miyazawa, K. Fukishima, and Y. Ideguchi. Molecular vibrations and structure of high polymers. III. Polarized infrared spectra, normal vibrations, and helical conformation of polyethylene glycol. *J. Chem. Phys.*, 37:2764–2776, 1962.

[90] Y. Takahashi and H. Tadokoro. Structural studies of Polyethers $(-(CH_2)_m - O-)_n$. X. Crystal structure of poly(ethylene oxide). *Macromolecules*, 23:672–675, 1973.

[91] R.D. Mountain, J.B. Hubbard, C.W. Meuse, and V. Simmons. Molecular Dynamics study of partial monolayer ordering of chain molecules. *J. Phys. Chem. B*, 105:9503–9508, 2001.

[92] R.D. Mountain, J.B. Hubbard, C.W. Meuse, and V. Simmons. Molecular Dynamics study of tethered chains. *NISTIR*, 6481, 2000.

[93] M. Kobayashi and M. Sakashita. Morphology dependent anomalous frequency shifts of infrared adsorption bands of polymer crystals: Interpretation in terms of transition dipoli-dipole coupling theory. *J. Chem. Phys*, 96:748–760, 1992.